University of California
Los Angeles

Experimental and Analytical Study of a High Gain Self Amplified Spontaneous Emission Free Electron Laser Operating in a Large Spectral Bandwidth Regime

A dissertation submitted in partial satisfaction
of the requirements for the degree
Doctor of Philosophy in Physics

by

Gerard Cosmos Andonian

2006

The dissertation of Gerard Cosmos Andonian is approved.

Harold R. Fetterman

George Igo

Claudio Pellegrini

James B. Rosenzweig, Committee Chair

University of California, Los Angeles

2006

To my family . . .

Table of Contents

List of Figures

List of Tables

Acknowledgments

The journey through graduate school is long, arduous and impossible to complete alone. I wish to acknowledge all those who were integral to the completion of the experiment and the composition of this dissertation. First, I am grateful to my advisor James Rosenzweig, who recruited me into the Particle Beam Physics Laboratory and provided continuous guidance and counsel. He was willing to roll up his sleeves and participate hands-on in the experiment which took place in Brookhaven National Laboratory, New York. I would also like to express my sincere gratitude to the other senior members of the Particle Beam Physics Laboratory. Claudio Pellegrini's work in Free Electron Laser research is internationally recognized and he has been very enthusiastic in disseminating his knowledge to inspired students. Sven Reiche has taught me about the subtle intricacies of FELs on numerous occasions and has always left his door open for discussions about any topic. Sven also graciously offered to proofread this manuscript; he was especially fond of the use of semicolons in the theory chapter. Gil Travish's organizational efforts alleviated a large part of the experimental management duties. I would also like to show appreciation to my dissertation committee members, George Igo and Harold Fetterman.

The VISA II experiment took place at the Accelerator Test Facility in BNL. There are a number of people who supported the UCLA group and the VISA II experiment during the tenure of the project. Vitaly Yakimenko, the ATF Director, kept the wheels rolling and was crucial in coordinating our experiment by maintaining open communications with UCLA. Ilan Ben-Zvi, the former Director, graciously welcomed me to the ATF and was integral in getting the experiment up and running. The ATF staff members deserve the utmost commendation for the

system maintenance: Marcus Babzien, Todd Corwin, Don Davis, Karl Kusche, Bob Malone, Martin Woodle, and Feng Zhou. They were always willing to lend a helping hand.

Of the many collaborators on the VISA II project, the success of the experiment directly depended on the ground warriors who had the mission of setting up the measurements, collecting and analyzing the data. Many experimental runs ran into the late night shift when sleep came at a premium. The roster of this hard-working crew, called the "VISA IB team", included Alex Murokh, Carlo Vicario, Jung Yun Huang and myself. Alex Murokh, a former graduate student at the ATF, showed me the ropes around Long Island and his contributions to the VISA program are felt until today.

Although the experiment took place in New York, I spent most of my time researching and preparing for the runs at the PBPL in Los Angeles. The PBPL is a dynamic entity with a zany cast of characters, each of whom has affected me in a unique way. I would like to thank all the members (past and present) of the PBPL who played a role in my graduate career at UCLA. They include post-doctorate researchers, graduate students, undergraduates, and staff members: Ron Agustsson, Scott Anderson, Hristo Badakov, Salime Boucher, Alan Cook, Mike Dunning, Joel England, Michael Fairchild, Pedro Frigola, Travis Holden, Jeremy Jacob, Jae Lim, Pietro Musumeci, Brendan O'Shea, Soren Telfer, Matt Thompson, Aaron Tremaine, Oliver Williams, Rodney Yoder.

I would like to applaud the UCLA Physics Machine Shop, anchored by Harry Lockart, whose team of machinists was able to realize parts from drawings and ship them out to New York on very short notice. Also, Jim Kolonko and Christine Green made sure that all necessary orders were placed and that travel vouchers were reimbursed in a timely manner.

I am very grateful for my parents and grandparents who have always championed education and encouraged me to attend graduate school to get a PhD. Finally, I am indebted to my wife, Pauline, for her steadfast love and resolute perseverance which provided the backbone of our marriage while I worked long hours far away from home.

Vita

1977	Born, Los Angeles, California, USA.
1994-1999	B.S. Physics, University of California Los Angeles.
1999-2002	Teaching Assistant, Department of Physics, UCLA.
2001	Outstanding Teaching Assistant Award, University of California Los Angeles.
2001	M.S. Physics, University of California Los Angeles.
2002	High Energy Density Physics Summer School, UC Santa Cruz and Lawrence Livermore National Laboratory, CA.
2003	US Particle Accelerator School, Louisiana State University, Baton Rouge, LA
2000–2006	Graduate Research Assistant, Particle Beam Physics Lab, Physics Department, UCLA.
2002–2006	Graduate Research Assistant, Accelerator Test Facility, Brookhaven National Laboratory, Upton, NY.

Publications

R. Agustsson, G. Andonian, M. Babzien, I. Ben-Zvi, P. Frigola, J. Huang, A. Murokh, L. Palumbo, C. Pellegrini, S. Reiche, J. Rosenzweig, G. Travish, V. Yakimenko,

Chirped Pulse Amplification at VISA-FEL, Nuclear Instruments and Methods in Physics Research Section A: Accelerators, Spectrometers, Detectors and Associated Equipment, **528**, Issues 1-2, 463 (2004)

G. Andonian, S. Telfer, S. Reiche, J. Rosenzweig, P. Frigola, *Status of the UCLA PEGASUS Injector Laboratory*, Proceedings of the 2002 Free Electron Laser Conference (2002)

G. Andonian, R. Agustsson, M. Babzien, I. Ben-Zvi, A. Murokh, L. Palumbo, C. Pellegrini, S. Reiche, J. Rosenzweig, G. Travish, C. Vicario, V. Yakimenko, *Design and Status of the VISA II Experiment*, Proceedings of the 2003 Particle Accelerator Conference, 944 (2003)

G. Andonian, S. Telfer, S. Reiche, J. Rosenzweig, P. Frigola, *Status of the UCLA PEGASUS Laboratory*, Proceedings of the 2003 Particle Accelerator Conference, 2110 (2003)

G. Andonian, R. Agustsson, M. Babzien, I. Ben-Zvi, I. Boscolo, S. Cialdi, M. Ferrario, A. Flacco, J. Huang, V. Litvinenko, A. Murokh, L. Palumbo, C. Pellegrini, S. Reiche, J. Rosenzweig, G. Travish, C. Vicario, V. Yakimenko, *VISA IB: Ultra-High Bandwidth, High Gain SASE FEL*, Proceedings of the 2004 Free Electron Laser Conference, 325 (2004)

G. Andonian, R. Agustsson, P. Frigola, M. Babzien, I. Ben-Zvi, I. Boscolo, S. Cialdi, M. Ferrario, A. Flacco, J. Huang, V. Litvinenko, A. Murokh, L. Palumbo, C. Pellegrini, S. Reiche, J. Rosenzweig, G. Travish, C. Vicario, V. Yakimenko,

Recent Results from and Future Plans for the VISA II SASE FEL, Proceedings of the 2005 Particle Accelerator Conference, 2167 (2005)

G. Andonian, A Murokh, C. Pellegrini, S. Reiche, J. Rosenzweig, G. Travish, M. Babzien, I. Ben-Zvi, V. Litvinenko, V. Yakimenko, I. Boscolo, S. Cialdi, A. Flacco, M. Ferrario, L. Palumbo, C. Vicario, J. Huang, *Simulations, Diagnostics and Recent Results of the VISA II Experiment*, Proceedings of the 27th International Free Electron Laser Conference, 83 (2005)

G. Andonian, A. Murokh, J. Rosenzweig, R. Agustsson, M. Babzien, I. Ben-Zvi, P. Frigola, J. Huang, L. Palumbo, C. Pellegrini, S. Reiche, G. Travish, C. Vicario, V. Yakimenko, *Observation of Anomalously Large Spectral Bandwidth in a High Gain Self-amplified Spontaneous Emission Free-Electron Laser*, Physical Review Letters, **95**, 054801 (2005)

G. Andonian, A. Murokh, J. Rosenzweig, R. Agustsson, M. Babzien, I. Ben-Zvi, P. Frigola, J. Huang, L. Palumbo, C. Pellegrini, S. Reiche, G. Travish, C. Vicario, V. Yakimenko, *Observation of Anomalously Large Spectral Bandwidth in a High Gain Self-amplified Spontaneous Emission Free-Electron Laser*, Virtual Journal of Ultrafast Science - August 2005, **4**, Iss. 8 (2005)

R. England, J. Rosenzweig, G. Andonian, P. Musumeci, G. Travish, R. Yoder, *Sextupole Correction of the Longitudinal Transport of Relativistic Beams in Dispersionless Translating Sections*, Physical Review Special Topics - Accelerators and Beams, **8**, 012801 (2005)

P. Frigola, G. Andonian, S. Reiche, J. Rosenzweig, S. Telfer, *Design and Operation of Pegasus Thermionic Cathode*, Proceedings of the 2003 Particle Accelerator Conference, 3321 (2003)

S. Reiche, G. Andonian, P. Frigola, J. Rosenzweig, S. Telfer, G. Travish, *The FEL Program at the PEGASUS Injector*, Proceedings of the 2003 Particle Accelerator Conference, 947 (2003)

S. Telfer, S. Reiche, J. Rosenzweig, P. Frigola, G. Andonian, *Commissioning of the UCLA PEGASUS Photoinjector Laboratory*, Proceedings of the 2001 Particle Accelerator Conference, 2263 (2001)

G. Travish, G. Andonian, P. Frigola, S. Reiche, J. Rosenzweig, S. Telfer, *The UCLA Pegasus Plane-Wave Transformer Photoinjector*, Proceedings of the 2003 Particle Accelerator Conference, 2112 (2003)

F. Zhou, R. Agustsson, G. Andonian, D. Cline, A. Murokh, J. Rosenzweig, I. Ben-Zvi, V. Yakimenko, *Experimental Characterizations of 4-D Transverse Phase Space of a Compressed Beam*, Proceedings of the 2005 Particle Accelerator Conference, 2263 (2005)

Abstract of the Dissertation

Experimental and Analytical Study of a High Gain Self Amplified Spontaneous Emission Free Electron Laser Operating in a Large Spectral Bandwidth Regime

by

Gerard Cosmos Andonian

Doctor of Philosophy in Physics

University of California, Los Angeles, 2006

Professor James B. Rosenzweig, Chair

The drive to create and measure ultra-short pulses in the x-ray regime advances the ongoing development of free electron lasers (FEL). Several proposed schemes, to shorten the pulse length of the radiation, involve driving the FEL with a chirped (linear longitudinal phase space correlation) electron beam in the self amplified spontaneous emission (SASE) mode. This dissertation examines the experiments conducted under such conditions, canvassing analytical and numerical studies of beam dynamics and radiation properties, experimental observations, and descriptions of the development of novel diagnostics.

The VISA (Visible-Infrared SASE Amplifier) program has achieved saturation at 840 nm within a 4 m long undulator. A novel bunch compression mechanism during transport was discovered and ultimately responsible for the high peak current required to drive the FEL. Start-to-end simulations, detailing the dynamics from electron beam inception at the photocathode to the FEL radiation properties at the undulator, were successfully benchmarked to observable data.

The VISA II experiment is an extension of this SASE FEL operating under different experimental conditions. Driving the SASE FEL with a chirped electron beam requires maintaining the chirp throughout transport by the use of sextupole magnets to correct for second-order compression effects. The emitted radiation is frequency chirped, diagnosed via a modified frequency resolved optical gating (FROG) technique. Specific numerical simulations and diagnostic developments are presented.

A set of measurements, without sextupole corrections, displays anomalous features, namely large spectral bandwidth of the radiation at stable and sustained high gain lasing. The bandwidth has an rms value of 21 nm (12% full width), previously unobserved in a FEL. In addition, the far-field angular distribution yields a hollow mode structure, similar to earlier results yet more pronounced in angle. Start-to-end simulations reproduced the most striking features of this radiation and yielded insight into the mechanisms of the unexpected behavior. It was deduced that the dominant source of the pulse broadening is the off-axis emission which emits coherently into angles as large as 2.5 mrad. A diagnostic to measure the spectral angular distribution of the FEL intensity was developed. These findings and experimental schemes are detailed in this dissertation.

CHAPTER 1

Introduction

In the scientific community, there is a clear demand for the production of high brightness light sources in the UV and x-ray regions of the electromagnetic spectrum. The use of man-made electromagnetic waves to study physical phenomena and structure dates back to the beginning of the 20th century. There have been many advancements along the way, from atomic spectroscopy to x-ray crystallography. Scientists, from a myriad of disciplines, require ever more brilliant sources to investigate the framework and underpinnings of complex processes at atomic levels and ultra short time scales. Currently, there is an intense drive to realize a radiation source capable of producing high peak power x-ray photons with Ångstrom wavelengths and pulses as short as tens of femtoseconds.

Such radiation sources have a near infinite number of possible applications. For example, these sources will enable biological sampling via single molecule diffraction. The dynamics of single protein folding can be unraveled by composing an atomic scale motion picture [1]. Investigations to study the interactions of viral entities with other microscopic organisms and matter are also proposed. Structural dynamics studies on the atomic scale require light with comparable wavelengths and ultra short pulses, so as not to destroy the sample under study by bombarding it with destructive levels of integrated power, which is one of the drawbacks of already existing x-ray technologies.

1.1 Light Sources: A Source for Brilliance

Brilliance is defined as the number of photons emitted by a source per unit time, per unit solid angle, per unit source area, per unit bandwidth. Brilliance, B_r, also called spectral brightness, is given by

$$B_r = \frac{d^2F}{d\omega d\Omega}, \tag{1.1}$$

and is typically represented in the units of [photons/s/mm^2/mrad/0.1%BW] [2]. It represents the brightness of a source centered around a given frequency, ω. Brightness,

$$B = \frac{dF}{d\Omega}, \tag{1.2}$$

is a less stringent concept with near identical units, [photons/s/mm^2/mrad], excluding the term 0.1%BW, which corresponds to the bandwidth centered around a given frequency. The flux,

$$F = \int \frac{1}{\omega}\frac{dI}{d\omega}d\omega, \tag{1.3}$$

is defined as the number of photons per unit time, per unit surface area of the source, and $d\Omega = d\theta_x d\theta_y$ is the subtended solid angle. The intensity,

$$I = \frac{dE}{dtdxdy} \tag{1.4}$$

is proportional to the energy per unit time, per unit source area. Brilliance and brightness are the most common and useful merits of the photon beam quality for light sources.

First generation light sources had a very low brightness or brilliance. First generation sources are actually electron storage rings built for high energy physics whose photon emission was parasitic with respect to the design of the machine. Eventually, the photon emission was harnessed for other experimental uses and

led to the development of dedicated radiation sources. The dedicated electron storage rings were classified as second generation light sources and were designated exclusively for improved photon beam production. These sources were able to reach brilliances near 10^{15} [photons/s/mm^2/mrad/0.1%BW] [2]. The third generation light sources, which encompasses accelerators with insertion devices (undulators), generate higher brightness coherent radiation with pulse lengths on the order of picoseconds. The fourth generation light sources, which include high gain free electron laser (FEL) amplifiers and Energy Recovery Linacs (ERL) [3], will reach a peak brilliance of 10^{35}, many orders of magnitude higher than the present day light sources. One candidate for such a radiation source is the x-ray free electron laser, which is an extension of already existing technologies in free electron lasers into the Ångstrom wavelength regime. There are currently numerous proposals to build such facilities, namely the Linac Coherent Light Source [4], the European X-ray Free Electron Laser [5], the Pohang X-ray Free Electron Laser [6], and the Spring8 Compact SASE Source in Japan [7].

1.2 Free Electron Lasers: A Brief History

The free electron laser (FEL) was first proposed by Madey in 1971 [8]. In the most basic terms, a free electron laser converts the kinetic energy of a relativistic electron beam into electromagnetic radiation [9]. This is accomplished by coupling the electron beam motion with an electromagnetic wave by use of a magnetic device called an undulator. The undulator, so named due to the motion exhibited by the electrons as they traverse the device, is a series of magnets (usually permanent magnets) arranged to yield an alternating magnetic field. The electrons' trajectories are oscillatory in the undulator field, and photons are emitted every period. The wavelength is defined by the energy of the electron beam and the

physical parameters of the undulator:

$$\lambda = \frac{\lambda_u}{2\gamma^2}\left(1 + \frac{K^2}{2} + \gamma^2\theta^2\right). \tag{1.5}$$

Here, λ is the radiated wavelength, λ_u is the period of the undulator magnetic field, γ is the normalized energy of the electron beam, K is the normalized magnetic deflection strength, and θ is the observation angle.

Details of the physical processes behind the FEL are reserved for Chapter 2; however, a simple outline of the gain process can be stated here. As photons are emitted, the electromagnetic wave is amplified, which in turn modulates the electron beam in a mechanism called *bunching*. This self-sustaining process continues until the FEL reaches a state of saturation, where additional photons do not amplify the radiated electromagnetic wave any further. The FEL process is initiated by an external electromagnetic field, the *seed*, co-propagating with the longitudinal direction of motion of the electron beam. The self amplified spontaneous emission (SASE) case, uses the spontaneous undulator radiation, emitted by the electron beam as it undergoes oscillation in the undulator, as the seeding field. The FEL may alternatively be seeded by a conventional source, such as a molecular laser with a well-defined wavelength and energy.

There are a number of advantages that the FEL possesses compared to that of traditional lasers and other radiation sources. The radiated wavelength (Eq. 1.5) is a function of the electron beam energy. Hence, the FEL is a tunable source of radiation whereas molecular lasers can only emit coherently at specific wavelengths which depend on excitation levels. Indeed, the FEL is able to operate in the x-ray region of the electromagnetic spectrum. Also, since the source of the FEL is an electron beam in vacuum, the FEL can operate at high power with no damage to the lasing medium, unlike traditional molecular lasers where the maximum power is limited to the damage threshold of the medium [10].

1.2.1 Experiments in FEL Physics

The first successful demonstration of a free electron laser was performed in Stanford in 1976 and 1977 [11, 12]. As of 2005, there have been dozens of free electron laser experiments realized, and many more have been proposed [13]. The operating principles of the self amplified spontaneous emission free electron laser have successfully been demonstrated in recent times. Proof-of-principle experiments have demonstrated exponential gain in SASE FEL operation since 1998 [14, 15]. In 2000 and 2001, there were three SASE FELs that reached saturation at high gain. Each of these experiments obtained data which is in close agreement to theory and simulations and will be summarized below.

The Low Energy Undulator Test Line (LEUTL) FEL [16] was the first SASE FEL to reach saturation. The LEUTL FEL was designed as a test-bed to study fourth generation light sources in the ultra-violet. It is located at the Advanced Photon Source (APS) at Argonne National Laboratory (ANL), Illinois. The LEUTL undulator consists of nine segments; each module has a length of 2.5 m. Diagnostic stations are placed between each undulator segment, and used to measure electron beam parameters such as position and bunching, as well as radiation properties such as spectra and energy. The LEUTL FEL operated in a wavelength range from 385 nm to 530 nm. Pioneering measurements at LEUTL included the analysis of FEL amplification as a function of undulator position and studies of harmonics during saturation.

The Visible-Infrared SASE Amplifier (VISA) FEL was a collaborative venture between UCLA, Brookhaven National Laboratory (BNL), and Stanford Linear Accelerator Center (SLAC), built at the Accelerator Test Facility (ATF) in New York [17]. The VISA FEL was the second project to achieve saturation operating in the SASE mode. It was designed to study aspects of SASE FEL physics

relevant to the Linac Coherent Light Source (LCLS). The undulator is comprised of four 1 m segments in vacuum. Novel intra-undulator diagnostics give the ability to measure both FEL and electron beam parameters. The operating wavelength was measured to be 840 nm, with an electron beam energy of 70 MeV [18]. Ultimately, a novel bunch compression mechanism was found responsible for the high current (250 A) required to achieve saturation within 4 m, corresponding to a gain length of 18 cm, the shortest ever recorded for a SASE FEL in the near infrared. The bunch compression mechanism was atypical as it did not employ a dedicated compressor. Rather, it was a side effect of second-order dispersion related to the intricacies of the bends in the transport line. The output radiation had a measured energy of 20 μJ, and a bandwidth of 2%. In addition, the angular distribution of the radiation yielded a unique hollow mode structure. All these findings were thoroughly analyzed with the aid of a robust start-to-end simulation suite of codes, which modeled beam creation, transport and the FEL process in an integrated manner. Subsequent sets of measurements, conducted at the VISA experiment, are the main subjects of Chapters 4 and 5.

The TESLA Test Facility (TTF), located at the Deutsche Elektronens Synchrotron (DESY) in Germany, also demonstrated high gain operation of a SASE FEL that reached saturation [19]. TESLA was designed to study the feasibility of linear colliders based on superconducting technology, and to provide a high brightness electron beam to drive a SASE FEL in the UV regime. The undulator is comprised of three 5 m long segments. Diagnostic stations are located between each module and allow measurements such as beam profile and position. The delivered beam energy was 250 MeV, and ultimately compressed with a bunch compressor yielding current spikes as high as 2.5 kA. The FEL wavelength at the TTF was measured to be 92 nm. Start-to-end simulations were able to reproduce the experimental findings. A second stage of experiments at TTF is operational

	LEUTL	VISA	TTF
Undulator length	20 m	4 m	15 m
Beam Energy	255 MeV	70 MeV	250 MeV
Beam Current	630 A	250 A	1.3 kA
Radiation Wavelength	530 nm	840 nm	92 nm

Table 1.1: A comparison of three successful single-pass high gain SASE FEL experiments that have achieved saturation.

at 30 nm, and serves as a forerunner to the European X-ray FEL that will be built in the future.

Although many other SASE FEL experiments were successful and relevant to the development of x-ray FELs, they have been omitted from this discussion for the purposes of brevity. More information regarding these experiments may be found in the References.

1.2.2 Realized Applications of FELs

Free electron lasers have been used for scientific research in user applications as well. Electrostatic FELs in the terrahertz region (far-infrared) of the electromagnetic spectrum have been used to conduct materials studies on semiconductor nanostructures, such as quantum wells and resonant tunneling diodes [20], as they were able to provide kilowatts of coherent radiation. Tunable infrared FELs have been used to study non-linear optical spectroscopies as they provide high average power with short pulses which are essential to resolve vibrational surface properties; the FEL also provides a gain in sensitivity, compared to molecular lasers, required for sum-frequency generation studies [21]. At the Thomas Jefferson National Accelerator Facility (TJNAF), an FEL with a pulse energy of 0.5 μJ

and pulse duration of 1 ps was used to study the lifetime of the vibrational mode of Hydrogen atoms in crystal silicon due to its increased stability and higher repetition rate [22].

With the incessant need of short duration radiation, current FEL research is primarily directed toward x-ray research applications. International SASE FEL projects have been proposed (notably LCLS and TESLA, but also in South Korea and Italy) to push the operating wavelengths into the x-ray regime, and to shorten the pulse duration to the femtosecond scale. The x-ray FEL will open new doors for scientists with its properties of spectral coherence and short duration, tunable frequency radiation [23].

1.3 Survey of the Dissertation

As the promise of x-ray free electron lasers comes close to realization, a number of experiments must be carried out to justify the feasibility of such a large scale investment. The subject matter of this dissertation deals with one such SASE FEL experiment, which was designed to investigate fundamental aspects of a proposed project at an x-ray FEL facility. Namely, the VISA (Visible to Infrared SASE Amplifier) experimental program, which encompasses the distinctive VISA IB and VISA II experiments, will be presented. The theory of the FEL will be disseminated in Chapter 2, where there is a focus on practical results that are relevant to our experiment and detailed mathematical derivations are reserved for the Appendix. The description of the experiment, including layout, design, and operating parameters, is recounted in Chapter 3. The VISA IB experiment, the unique observation of an ultra-wide bandwidth SASE FEL, is discussed and analyzed with the aid of a robust simulation suite in Chapter 4. The design and preliminary measurements for the VISA II experiment, a chirped beam SASE

FEL, are presented in Chapter 5. This dissertation will conclude with a brief summary of obtained results, as well as an outlook to future experiments and measurements that will expand upon the growing knowledge base gained from the VISA program.

CHAPTER 2

Basic Principles of Free Electron Lasers

This chapter will review the basic theory behind the free electron laser (FEL) with an emphasis on the results that are relevant to the experiment at hand. Extensive calculations are reserved for the appendices specified in the appropriate sections, or left as references. The chapter begins with a general description of free electron lasers. The equations of motion for a single electron in a periodic magnetic field are derived using a Hamiltonian approach in Section 2.2. Section 2.3 explores the phenomenon of *spontaneous emission*, or undulator radiation, and the derivation of the resonance condition. This is followed by the derivation of the equations of motion for an electron in the combined fields of the undulator and the external electromagnetic wave co-propagating with the electrons. The derivation of the self-consistent FEL equations, which take into account both the undulator and the varying radiation fields (time-dependent) begins with Maxwell's equations; the effect of the electron trajectory on the electromagnetic wave is studied and the subsequent resonance condition is obtained. Normalized, scaled variables are introduced to simplify the self-consistent FEL equations. Formal solutions to these equations are quoted in Section 2.5; approximations to limiting scenarios (1-D model) are considered to present a qualitative understanding of the dependence of the FEL performance on certain parameters, such as the Pierce and detuning parameters. 3-D effects and extensions to the newly introduced parameters are examined in Section 2.6. The concept of *self*

amplified spontaneous emission (SASE) is familiarized and contrasted with the *seeded amplifier* notion. Finally, electron beam considerations (such as chirp, energy spread, and current) are analyzed with respect to FEL performance. Although a basic knowledge of accelerator physics fundamentals is a prerequisite for this chapter, the most important concepts are defined in the context of the FEL theory.

2.1 General Overview of Free Electron Lasers

In the most basic terms, a free electron laser (FEL) transforms the kinetic energy of a relativistic electron beam into coherent electromagnetic radiation [9]. The relativistic electron beam propagates through an undulator magnet, which causes the electrons to oscillate in the direction transverse to the nominal beam motion (Figure 2.1). The electrons emit radiation every oscillation through the undulator. The emission per period is broadband, however, since the electrons emit periodically over a long time interval, certain frequencies are enhanced through period-to-period interference effects. The wavelength of the enhanced radiation is dependent on the energy of the electrons and the parameters of the employed magnetic structure. As the electrons travel colinearly with the electromagnetic wave, a component of the electron velocity lies in a direction along the transverse electric field of the wave; this allows for an energy exchange. As the energy is transferred from the electrons to the wave, the radiation field is amplified and the electrons are slowed down. The electron energy distribution as a function of longitudinal position in the bunch is also modulated by the electron's interaction with the radiation. As a result, the electrons tend to physically group in bunches separated by the radiation wavelength. The radiation is greatly enhanced further by this process, which is called *microbunching*. Once all the electrons are coherently

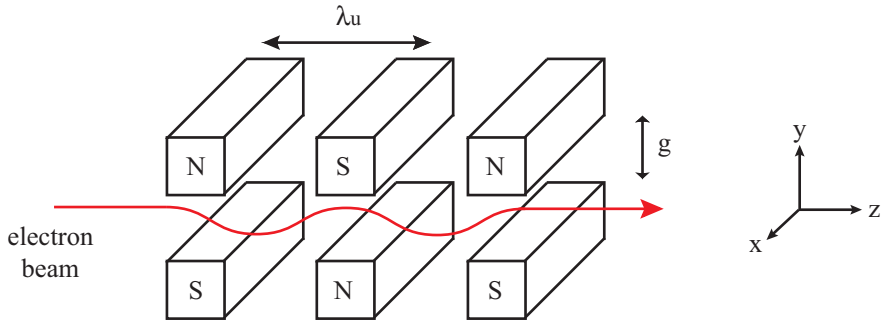

Figure 2.1: A sketch of a simple planar undulator; λ_u is the period of the undulator, and g is the gap.

emitting in phase, maximal bunching is achieved and the FEL reaches saturation. At this point the energy gain of the field is not significantly enhanced by additional modulation. The closed loop process (oscillation, field enhancement, modulation) is referred to as the *collective instability* and is the basic operating mechanism of the free electron laser. The converse scenario is also a field under active study; if the energy is transferred from the electromagnetic wave to the electrons, the electrons are accelerated in a device referred to as the inverse free electron laser [24].

The free electron laser is a tunable, coherent source for electromagnetic radiation which can operate at wavelengths ranging from 1 centimeter to 1 Ångstrom (x-ray) in the electromagnetic spectrum. In the following sections, the physics underlying the FEL is presented in an analytic format. The methods employed in References [9, 25, 26, 27] are closely followed. The intent of this chapter is to present the theory of the FEL and introduce the most important terms relevant to the experiment at hand. In some instances, the reader is directed to the Appendix or the References for detailed calculations and derivations of some formulae.

2.2 Equations of Motion in a Planar Undulator

An undulator is a periodic structure composed of magnets of alternating polarity. The motion an electron undergoes while traversing through the undulator is sinusoidal, to first-order. The helical undulator has alternating field components in both transverse dimensions creating a helical trajectory for an electron entering it. The planar undulator has an alternating field in only one dimension causing transverse electron oscillations in one dimension. The planar undulator will be discussed almost exclusively throughout this manuscript as a planar undulator is employed for the SASE FEL experiment described.

The typical field in a planar undulator, near the axis, is approximated by

$$\vec{B} = B_0 \cos\left(\frac{2\pi z}{\lambda_u}\right)\hat{y}, \tag{2.1}$$

where B_0 is the peak magnetic field of the undulator, and λ_u is the length of the undulator period (Figure 2.1). In Eq. 2.1, z is the longitudinal coordinate and the magnetic field oscillates along the vertical dimension, $\hat{y}$.

The electron velocity normalized to the speed of light, c, is

$$\vec{\beta} = \frac{\vec{v}}{c} = \beta_x\hat{x} + \beta_y\hat{y} + \beta_z\hat{z}. \tag{2.2}$$

The relativistic Lorentz factor, denoted by γ, is defined as

$$\gamma = \frac{1}{\sqrt{1-\beta^2}}. \tag{2.3}$$

The equations of motion for the electrons are readily obtained using the principles of Hamiltonian dynamics [28]. A brief review of Hamiltonian dynamics is presented in Appendix B. The Hamiltonian for an electron, of mass m and charge e, in an electromagnetic field is

$$H = \sqrt{\left(\vec{p} - e\vec{A}\right)^2 c^2 + m^2c^4}; \tag{2.4}$$

in the case of a magnetostatic undulator the Hamiltonian is not an explicit function of time, and is thus a constant of the motion. Therefore the Hamiltonian can be equated to the total energy of the system, $H = \gamma mc^2$. The vector potential, $\vec{A}$, for the planar undulator on-axis can be approximated by,

$$\vec{A} = \frac{B_0}{k_u} \sin(k_u z)\, \hat{x}, \tag{2.5}$$

which is derived (to first-order) in the usual manner from $\vec{B} = \vec{\nabla} \times \vec{A}$. Here, $k_u = 2\pi/\lambda_u$ is the wavenumber associated with the period of the undulator.

It has been shown that a quantum treatment is not necessary to construct an appropriate physical model of the free electron laser, therefore the *quasi-classical* approach is adequate [29, 30] and will be applied here. Following the classical Hamiltonian formalism, the canonical momentum is derived. The transverse canonical momenta of the system are conserved:

$$\dot{p}_x = -\frac{\partial H}{\partial x} = 0, \tag{2.6}$$

$$\dot{p}_y = -\frac{\partial H}{\partial y} = 0, \tag{2.7}$$

or explicitly,

$$p_x = m\gamma c\beta_x + eA_x = \text{constant}, \tag{2.8}$$

$$p_y = m\gamma c\beta_y + eA_y = \text{constant}. \tag{2.9}$$

The transverse trajectories are given by

$$\dot{x} = \frac{\partial H}{\partial p_x} = \frac{p_x - eA_x}{\gamma m}, \tag{2.10}$$

$$\dot{y} = \frac{\partial H}{\partial p_y} = \frac{p_y - eA_y}{\gamma m}. \tag{2.11}$$

With the assumption that the initial velocity is completely axial, the electrons initially do not have any components of velocity in the transverse dimensions.

Then the constant values of p_x and p_y are set to zero to simplify the upcoming mathematical expressions. Dividing by c, and using the definition of the undulator parameter,

$$K = \frac{eB_0}{k_u mc}, \tag{2.12}$$

the transverse velocities are expressed as

$$\beta_x = -\frac{K}{\gamma}\sin\left(k_u z\right), \tag{2.13}$$

$$\beta_y = 0. \tag{2.14}$$

The longitudinal component of the trajectory is solved for by revisiting Eq. 2.3. Since magnetic fields perform no work on charged particles (they merely alter the trajectory), the total energy of the system is conserved. Using the fact of energy conservation and the expression for the transverse velocity, the longitudinal velocity of the electrons is

$$\begin{aligned}\beta_z^2 &= 1 - \frac{1}{\gamma^2} - \beta_x^2 - \beta_y^2, \\ \beta_z &= \frac{K^2}{4\gamma^2\beta_0}\cos(2k_u\beta_0 ct) + \beta_0.\end{aligned} \tag{2.15}$$

Here, β_0 is the average longitudinal velocity, given by

$$\beta_0 = \left\langle\sqrt{1 - \frac{1}{\gamma^2} - \beta_x^2}\right\rangle \approx 1 - \frac{1 + \frac{K^2}{2}}{2\gamma^2}. \tag{2.16}$$

The longitudinal velocity of the electron beam is "slowed" down once it enters the undulator as some of the energy is transferred into horizontal oscillations.

Since the average longitudinal velocity is much greater than the amplitude of the horizontal velocity ($\beta_0 \gg K/\gamma$), the longitudinal trajectory (to first-order) is approximated as $c\beta_0 t + z_0$. Integration of Eq. 2.15, to first-order, gives the longitudinal component of the trajectory,

$$z(t) = \frac{K^2}{8\gamma^2\beta_0^2 k_u}\sin\left(2k_u\beta_0 ct\right) + \beta_0 ct + z_0. \tag{2.17}$$

The transverse trajectory component is obtained by integrating Eq. 2.13;

$$x(t) = \frac{K}{k_u \beta_0 \gamma} \cos\left(k_u \beta_0 c t\right) + x_0. \tag{2.18}$$

Moreover, as the electrons oscillate transversely at a frequency of $k_u \beta_0 c$, an additional "fast" oscillation in the longitudinal direction at twice the frequency is imposed. It will be shown in the following sections that when the other terms in the expression for β_z are considered, the electron beam is modulated in the longitudinal dimension.

2.3 Undulator Radiation

The phenomenon of spontaneous emission in an undulator, also referred to as undulator radiation, occurs as a consequence of the motion of the electrons in the undulator (Figure 2.2). Radiation is emitted at each period of oscillation. Constructive interference of this radiation will occur under specific conditions; radiation pulses add up coherently to amplify the emitted electromagnetic wave. The time between pulses of the emitted radiation multiplied by c yields the wavelength of the emitted radiation,

$$\lambda = c\Delta T = \frac{\lambda_u}{\beta_z} - \lambda_u \cos\theta. \tag{2.19}$$

The radiation interferes constructively if the wavelength is an integer multiple of the above expression.

Since the electrons are relativistic, the radiation is emitted within a cone (with $\theta \propto 1/\gamma$) confined axially along the undulator. The expansion for β_z with small angles becomes

$$1 - \beta_z \approx \frac{1}{2\gamma^2}\left(1 + \frac{K^2}{2}\right). \tag{2.20}$$

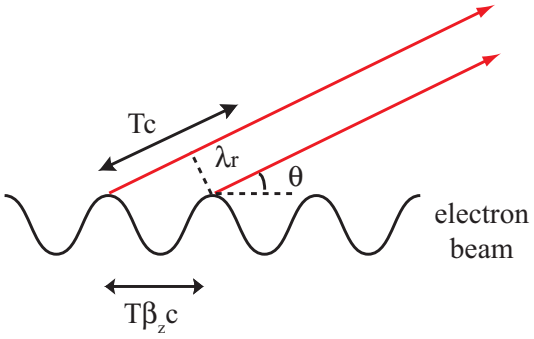

Figure 2.2: A schematic of the requirements for coherent radiation emission from an oscillating electron beam.

The wavelength of the coherent undulator radiation from Eq. 2.19 is

$$\lambda = \frac{\lambda_u}{2\gamma^2}\left(1 + \frac{K^2}{2} + \gamma^2\theta^2\right). \tag{2.21}$$

Eq. 2.21 is called the *resonance condition*. It is apparent that for a full undulator of length $N_u\lambda_u$ (where N_u is the number of undulator periods), and $\theta = 0$, the total time of travel through the undulator will be $\Delta t = N_u \Delta T$. This yields a linewidth of the radiation (full width at half maximum) of

$$\frac{\Delta\omega}{\omega} = \frac{1}{N_u}, \tag{2.22}$$

where $\omega = 2\pi/\lambda$ is the frequency of the radiation.

The spectral angular distribution for the planar undulator radiation is derived in detail in Appendix C; the results are stated here. The intensity distribution for the fundamental harmonic of a single electron, in the on-axis emission direction is given by

$$\frac{d^2I}{d\omega d\Omega} = \frac{e^2 N_u^2 \gamma^2 K^2}{c(1+\frac{K^2}{2})^2} F_1(K) \left(\frac{\sin x_1}{x_1}\right)^2, \tag{2.23}$$

with

$$F_1 = F_1(K) = \left[J_0\left(\frac{K^2}{4(1+\frac{K^2}{2})}\right) - J_1\left(\frac{K^2}{4(1+\frac{K^2}{2})}\right)\right]^2, \tag{2.24}$$

and

$$x_1 = \pi N_u \left(\frac{\omega - \omega_r}{\omega_r} \right), \tag{2.25}$$

where

$$\omega_r = \frac{2ck_u\gamma^2}{1 + \frac{K^2}{2}} \tag{2.26}$$

is the resonant frequency derived from Eq. 2.21 for the on-axis case ($\theta = 0$). The J_n's of Eq. 2.24 are the Bessel functions. A formal derivation of these results, including higher harmonics, is presented in Appendix C.

This study can be expanded from a single electron to a distribution of electrons. Although the issue is formally addressed later, a brief qualitative argument is initiated here. By taking the derivative of Eq. 2.21, the collective effects of an electron beam on the undulator radiation spectrum are briefly analyzed:

$$\frac{\Delta\lambda}{\lambda} = \frac{-2\Delta\gamma}{\gamma} + \frac{2K\Delta K}{1 + K^2} + \frac{\gamma^2(\Delta\theta)^2}{1 + K^2}. \tag{2.27}$$

The linewidth broadening is dominated by the first term, $\Delta\gamma/\gamma$, which is proportional to the energy spread in the electron beam. The last two terms, which define the magnetic errors and the angular spread of the electrons in the beam, respectively, are combined to put a constraint on the quality of the electron beam in the undulator. The effects of electron beam parameters on field enhancement will be studied in more detail in Section 2.6.

2.4 Equations of Motion in the Combined Fields

To continue the study of the electron motion in an undulator, the effect of the radiation on the electrons must be considered. The radiation field, $\vec{E}_r = -\partial\vec{A}_r/\partial t$, has a vector potential given by

$$\vec{A}_r = \frac{E_0}{k_r c} \sin\left(k_r(z - ct) + \Psi_r\right) \hat{x}; \tag{2.28}$$

here, $k_r = 2\pi/\lambda$ is the wavenumber of the radiated wave, Ψ_r is the initial phase of the field, and E_0 is the maximum amplitude of the electromagnetic wave. The plane wave is horizontally polarized for a planar undulator, while a helical undulator yields circularly polarized radiation.

The vector potential for the undulator field is given by Eq. 2.5. The combined vector potential is simply

$$\vec{A} = \vec{A}_u + \vec{A}_r. \tag{2.29}$$

Using the Hamiltonian formalism (Eq. 2.4), as in the previous section, the transverse velocity is given by

$$\beta_x = -\frac{e}{\gamma m}\left(A_{u,x} + A_{r,x}\right), \tag{2.30}$$

where $A_{u,x}$ and $A_{r,x}$ are the horizontal components of the undulator and radiation vector potential, respectively. Inserting the known values for the horizontal components of the vector potential yields

$$\beta_x = -\frac{K}{\gamma}\sin\left(k_u z\right) - \frac{K_r}{\gamma}\sin\left(k_r(z-ct) + \Psi_r\right), \tag{2.31}$$

where the dimensionless radiation coefficient, K_r, is defined analogously to the undulator parameter;

$$K_r = \frac{eE_0}{k_r mc^2}. \tag{2.32}$$

The longitudinal velocity is obtained from the definition of the Lorentz factor (Eq. 2.3) and the transverse velocity (Eq. 2.31). Realizing that the vector potential A_r, although time-dependent, has a negligible effect, energy conservation is used to approximate β_z as

$$\begin{aligned}\beta_z \approx \quad & 1 - \frac{1 + \frac{K^2}{2} + \frac{K_r^2}{2}}{2\gamma^2} + \frac{K^2}{4\gamma^2}\cos(2k_u z) \\ & + \frac{K_r^2}{4\gamma^2}\cos(2k_r(z-ct) + 2\Psi_r) \\ & - \frac{KK_r}{\gamma^2}\sin(k_u z)\sin(k_r(z-ct) + \Psi_r).\end{aligned} \tag{2.33}$$

As an initial step, Eq. 2.33 is integrated to first-order, neglecting the terms with amplitudes that are proportional to K_r and K_r^2, since $K \gg K_r$, to yield

$$z(t) = c\beta_0 t + \frac{K^2}{8\gamma^2 k_u} \sin(2ck_u\beta_0 ct) + z_0, \tag{2.34}$$

where β_0 is the average longitudinal velocity, similar to that of the previous section,

$$\beta_0 = 1 - \frac{1 + \frac{K^2}{2} + \frac{K_r^2}{2}}{2\gamma^2}. \tag{2.35}$$

2.4.1 Energy Transfer

The energy exchange between a charged particle in an electric field is given by [31]

$$\dot{U} = e\vec{v} \cdot \vec{E}, \tag{2.36}$$

where $U = \gamma mc^2$ is the particle energy, $\vec{v}$ is the particle velocity and $\vec{E}$ is the electric field of the copropagating wave. This expression is rewritten in a readily useable form:

$$\dot{\gamma} = \frac{e\vec{\beta} \cdot \vec{E}}{mc}. \tag{2.37}$$

Recalling $\vec{E} = -\partial\vec{A}/\partial t$, the expression for the energy transfer relation (Eq. 2.37), neglecting higher-order terms, is explicitly

$$\dot{\gamma} = -\frac{k_r cKK_r}{\gamma} \sin(k_u z) \cos\left(k(z - ct) + \Psi_r\right). \tag{2.38}$$

From Eq. 2.38 it is apparent to achieve maximal energy transfer, the total phase must be kept constant. Rewriting the sine and cosine terms as exponential functions, the expression for the total resonant phase, θ, and its derivative, are

$$\theta = (k_u + k_r)z - k_r ct, \tag{2.39}$$

$$\dot{\theta} = c(k_r + k_u)\beta_z - ck_r. \tag{2.40}$$

The phase θ is often called the *ponderomotive force phase* [9] (the phase of the ponderomotive or beat wave created by the radiation field's and electron's spatio-temporal oscillations), which is the phase difference between the electrons longitudinal motion and the phase of the radiated wave. The other term from Eq. 2.38, $(k_u - k_r)z - k_r ct$ is not resonant (it averages to near zero over a period) and therefore it is not considered in this calculation.

The resonance condition is derived from the requirement that the total phase remain constant ($\dot{\theta} = 0$),

$$\beta_z = \frac{k_r}{k_u + k_r}. \tag{2.41}$$

Using the expansion for β_z, this condition yields the same wavelength of radiation as for spontaneous emission, therefore, the electromagnetic wave from undulator radiation is further amplified under these conditions.

The argument for the longitudinal velocity, β_z, must be correctly expressed to obtain an accurate model of the physical processes: The oscillatory term from Eq. 2.34 must also be considered as the first-order approximation is no longer valid. Again, exponential forms are used to represent the trigonometric functions. The mathematical expression from Appendix C (Eq. C.10) [32] relates the exponential of a sine function to a power series,

$$e^{-ia\sin b} = \sum_{m=-\infty}^{\infty} e^{-imb} J_m(a), \tag{2.42}$$

where $J_m(a)$ are the Bessel functions. Using this relation, while keeping only the terms resonant at the fundamental wavelength, the expression for the longitudinal velocity is

$$\beta_z = \beta_0 + \frac{F_1 K K_r}{2\gamma^2} \cos(\theta + \Psi_r), \tag{2.43}$$

with $F_1 = J_0(\xi_1) - J_1(\xi_1)$, which is defined explicitly in Appendix C, and ξ_1 is

given by the expression (also defined in the Appendix C),

$$\xi_1 = \frac{K^2}{4(1+\frac{K^2}{2})}. \tag{2.44}$$

Appendix C includes an in-depth derivation of the form factor ($F_n(K)$) which is prevalent in most results involving the planar undulator. With this expression for the longitudinal velocity, Eqs. 2.40 and 2.38 are written as

$$\dot{\theta} = c\left(k_u - k_r \frac{1+\frac{K^2}{2}+\frac{K_R^2}{2} - F_1 K K_r \cos(\theta+\Psi_r)}{2\gamma^2}\right), \tag{2.45}$$

$$\dot{\gamma} = -ck_r F_1 \frac{K K_r}{2\gamma}\sin(\theta+\Psi_r). \tag{2.46}$$

Eqs. 2.45 and 2.46 are called the 1-D FEL pendulum equations. It is possible to derive these equations from a new Hamiltonian with the conjugate variables (θ, γ):

$$H(\theta,\gamma) = ck_u\gamma + ck_r\left(\frac{1+\frac{K^2}{2}+\frac{K_R^2}{2} - F_1 K K_r \cos(\theta+\Psi_r)}{2\gamma}\right). \tag{2.47}$$

The motivation for the new Hamiltonian, $H(\theta,\gamma)$ will be clear in the following section. The physical interpretation of these variables is clear in the context of the FEL. The energy modulation of the system is described by Eq. 2.46, whereas Eq. 2.45 describes the evolution of the relative phase of the longitudinal motion with respect to the radiated wave.

2.4.2 Pendulum Equations

A change of variables will simplify the expression in the FEL equations. The resonant energy, for this specific scenario, is defined as

$$\gamma_R^2 = \frac{k_r}{2k_u}\left(1+\frac{K^2}{2}\right), \tag{2.48}$$

and the new variable representing the energy deviation, η, is defined as

$$\eta = \frac{\gamma - \gamma_R}{\gamma_R}. \tag{2.49}$$

Now, incorporating the initial phase Ψ_r into the ponderomotive phase ($\theta \rightarrow \theta + \Psi_r$), and neglecting the terms proportional to $KK_r \cos\theta$ and K_r^2 because they are small, Eqs. 2.45 and 2.46 become

$$\dot{\theta} = 2ck_u\eta, \tag{2.50}$$

$$\dot{\eta} = -\Omega^2 \sin\theta, \tag{2.51}$$

with

$$\Omega^2 = \frac{ck_r F_1 K K_r}{2\gamma_R^2}. \tag{2.52}$$

The respective Hamiltonian that describes the motion in this equations is

$$H(\theta, \eta) = ck_u\eta^2 - \Omega^2 \cos\theta, \tag{2.53}$$

with the new canonical variables (θ, η). With these redefined conjugate variables, a familiar second-order differential equation is derived,

$$\ddot{\theta} + 2ck_u\Omega^2 \sin\theta = 0. \tag{2.54}$$

Eq. 2.54 is well-known in classical mechanics. It is often informally referred to as the *pendulum equation*, a second-order differential equation which describes the trajectory of a pendulum. The solutions to this equation have been mathematically studied and are readily available. Only its relevant interpretations will be discussed in this section.

The FEL operating under these principles is historically referred to as being in the *small signal gain* (SSG) regime [9]. The curves of constant energy are plotted in Figure 2.3. Any particles that are injected at an energy below the

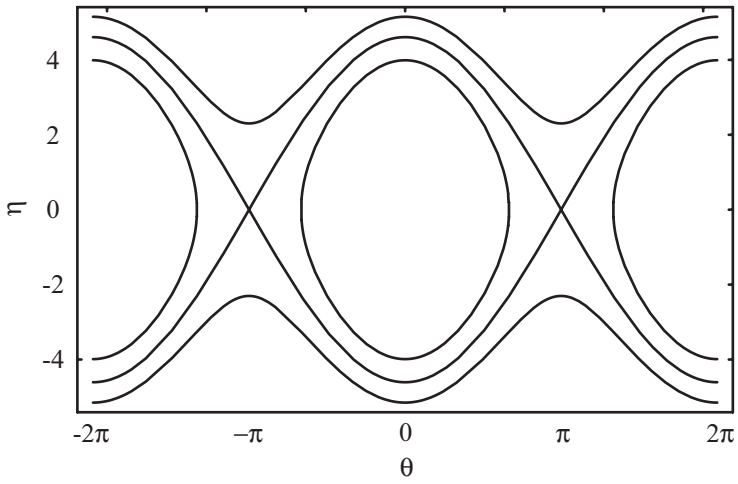

Figure 2.3: The constant H-curves (constant energy) of the Hamiltonian plotted in the longitudinal phase space (θ, η). The separatrix defines the crossing between stable and unstable motion.

energy defining the separatrix in Eq. 2.54, are caught in the bucket, and their motion is stable. Those particles that lie outside the separatrix exhibit unstable motion. Figure 2.3 is illustrative because it shows that an ensemble of electrons either gains or loses energy. Particles with energy greater than the separatrix energy move forward with respect to the initial phase, and lower energy particles fall back. Thus the electrons tend to group together in the longitudinal phase space buckets at phases that are multiples of 2π ($\theta = 0, 2\pi, 4\pi$, etc.). This phenomenon, known as bunching, also called *microbunching* to differentiate from the electron macro-pulses emitted by pulsed accelerating source (e.g. rf injectors), is an integral component for an operating FEL. As the electromagnetic wave is amplified, the longitudinal modulation is increased; electrons become bunched together to emit collectively at the same phase. The coherent emission is enhanced which leads to additional bunching. This collective instability is a closed loop process which drives FEL operation. The *high gain* regime will be analyzed in the following section.

2.5 High Gain Free Electron Laser

Although the small signal gain (SSG) regime if beneficial for an intuitive understanding of the FEL process, it is only an approximation and some assumptions must be lifted for a thorough comprehension of the collective instability. The SSG model neglects the *space charge* effect. For high current density beams, the space charge forces (electrostatic electron beam self-forces) are repulsive, and act in direct opposition to the bunching mechanism discussed previously. Thus, space charge forces inhibit the FEL gain process as they work against the radiation field's attempt to modulate the electron beam. Also, the SSG model does not include the effect of the updated electron trajectories on the radiated field itself, i.e. the radiated fields are considered constant in time. For a complete appreciation of the physical process, the radiation field must be allowed to be a function of time, depending on the changes of trajectories of the electron beam.

To begin this study, Maxwell's equations are revisited with the applicable source terms for charge and current density. Since all physical processes are contained in this description, the subsequent equations of motion are referred to as the *self-consistent* set of FEL equations. This set of equations, which are difficult to solve without the aid of numerical methods, will be scaled to new variables. With some appropriate approximations and the aid of the new variables, physical insight is obtained for the high gain FEL.

Several wave equations can be obtained from Maxwell's relations [31];

$$\left[\vec{\nabla}^2 - \frac{d^2}{c^2 dt^2}\right] \vec{A} = -\mu_0 \vec{J}_e, \tag{2.55}$$

$$\left[\vec{\nabla}^2 - \frac{d^2}{c^2 dt^2}\right] \varphi = -\frac{\rho_e}{\epsilon_0}. \tag{2.56}$$

Here the constants ϵ_0 and μ_0 are the dielectric permittivity and magnetic permeability of vacuum, respectively. The current density, $\vec{J}_e$, and the charge distribu-

tion, ρ_e, are given by the familiar relations

$$\vec{J}_e = ec\sum_{l=1}^{N_e}\vec{\beta}_l(t)\delta(\vec{r}-\vec{r}_l(t)), \qquad \rho_e = e\sum_{l=1}^{N_e}\delta(\vec{r}-\vec{r}_l(t)). \tag{2.57}$$

The Dirac-delta function is represented by $\delta(\vec{r})$, and $\vec{r}_l$ is the trajectory of the lth electron. The velocity, $\vec{\beta}$, was derived in the previous section for different scenarios. The charge and current density are related by the continuity equation,

$$\frac{d\rho_e}{dt} + \vec{\nabla}\cdot\vec{J}_e = 0. \tag{2.58}$$

Eq. 2.58 allows us to express the current density in terms of the charge density in Maxwell's equations. Following the methods described in Refs. [9, 25], the complex quantities, $\tilde{J} = J_x - iJ_y$ and $\tilde{A} = A_x - iA_y$, are introduced. The complex vector potential is

$$\tilde{A} = i\frac{E_r}{k_r}e^{i\Psi_r}e^{ik_r(z-ct)} = i\frac{mc}{e}ue^{ik(z-ct)}, \tag{2.59}$$

where the complex amplitude, $u = -iK_re^{i\Psi_r}$, has been incorporated. The complex vector potential for the undulator field is defined analogously as

$$A_u = \frac{imcK}{e}e^{-ik_uz}. \tag{2.60}$$

Since the wave is periodic, the longitudinal electrostatic field may be represented as a Fourier series, $E_z = \sum_n \hat{E}_n\exp(in\theta)$. Then, we combine the wave equations of Eqs. 2.55 and 2.56 and the continuity equation to obtain

$$\left[\vec{\nabla}^2_{x,y} - \frac{n^2k_r^2\left(1+\frac{K^2}{2}\right)}{\gamma_R^2}\right]\hat{E}_n = \frac{inek_r\left(1+\frac{K^2}{2}\right)}{\epsilon_0\gamma_R^2}\sum_{n=1}^{\infty}\delta(\vec{r}-\vec{r}_l)e^{-in\theta_l}. \tag{2.61}$$

It is assumed that the radiation field and electron beam have no transverse coordinate dependence, so the differential operator on the left-hand side of Eq. 2.61 is dropped.

The transverse velocity, β_x, is used to obtain the current density of the beam. To linearize the system and obtain the 1-D FEL equations, we first write the explicit wave equation with appropriate approximations. Using the paraxial approximation for the radiation field [33] (the wave is propagating in the $\hat{z}$-direction), assuming no transverse dependence of the radiation field and electron beam, and neglecting terms that are second-order derivatives of the complex field amplitude u, the wave equation is

$$\left[\frac{\partial}{\partial z}+\frac{1}{c}\frac{\partial}{\partial t}\right]u=-\frac{\alpha}{k_r}\sum_{l=1}^{N_e}\left(\frac{F_1K}{\gamma_l}e^{-i\theta_l}-i\frac{u}{\gamma_l}\right)\delta(\vec{r}-\vec{r_l}), \tag{2.62}$$

with $\alpha = e^2\mu_0/2m$. The time-derivative on the left-hand side of Eq. 2.62 describes the *slippage*, as it defines the difference between the electron beam velocity compared to the speed of light. Now the self-consistent FEL equations (Eqs. 2.45 and 2.46) are written in the complex form,

$$\dot{\theta}_l = ck_u - ck_r\left(\frac{1+\frac{K^2}{2}}{2\gamma_l^2}\right)+\frac{k_rF_1K\left(ue^{i\theta_l}-\text{c.c.}\right)}{2\gamma_l^2}, \tag{2.63}$$

$$\dot{\gamma}_l = -\frac{ck_rF_1K}{2\gamma_l}\left(ue^{i\theta_l}+\text{c.c.}\right)+\frac{e}{mc}\sum_{n=1}^{\infty}\left(\hat{E}_ne^{i\theta_l}+\text{c.c.}\right). \tag{2.64}$$

In Eq. 2.64, the second term on the right-hand side is called the space charge and will be expounded on in the upcoming sections. A number of simplifications were made in the 1-D model to obtain the self-consistent set of equations defined in Eqs. 2.63 and 2.64: the transverse differential operator was neglected, for the steady state solution, the time derivative in Eq. 2.62 was taken as constant, the complex field was assumed small, and the series was summed only up to the first term ($n = 1$) to describe the system in the linear regime. This set of equations describe the motion of the individual electrons and the radiation field, and are often referred to as the *1-D FEL equations*.

The solutions to these equations have been obtained using numerical methods

[34], however only limiting cases of interest will be considered in this manuscript. Also, for a full description of a realistic beam including important effects such as diffraction, the *3-D FEL equations* must be addressed. Although the solutions will be motivated and quoted, only the repercussions of real electron beam effects (such as energy spread and current distribution), rather than detailed derivations, will be mentioned in Section 2.6.

2.5.1 FEL Equations with Scaled Variables

In this section, the mathematical methods of Reference [35] are followed; the scaled FEL variables are introduced. As will be shown, the most important of the new parameters is the FEL parameter (also called the Pierce parameter [35]), which defines the scaling of the FEL equations with dimensionless variables. For the planar undulator, the Pierce parameter is defined as

$$\rho = \left(\frac{F_1 K \gamma_0 \Omega_p}{4 c \gamma_R^2 k_u} \right)^{2/3}. \tag{2.65}$$

The second parameter which is necessary for rescaling the FEL equations is the so-called *detuning* parameter δ,

$$\delta = \frac{\gamma_0^2 - \gamma_R^2}{2\gamma_R^2 \rho}, \tag{2.66}$$

where γ_0 is the mean energy of the electron ensemble. For a small deviation from the resonant energy, Eq. 2.66 can be approximated as

$$\delta = \frac{\Delta\gamma}{\gamma\rho}. \tag{2.67}$$

As is obvious from this equation, the detuning parameter measures the difference in energy of the electron beam from the resonance energy obtained from the wavelength of the radiation field. The resonant energy was defined in the previous

section,

$$\gamma_R = \frac{k_r}{2k_u}\frac{1+\frac{K^2}{2}}{2}. \tag{2.68}$$

The detuning parameter is extremely important for the seeded amplifier experiments at VISA, as will be addressed in Section 6.1. A third parameter, space charge, describes the repulsion forces that the electrons encounter due to the close proximity achieved through bunching. The space charge coefficient is a measure of the inhibition of the bunching, which is required for field enhancement. It is defined as

$$\sigma_\gamma = \frac{\Omega_p \gamma_0}{c k_r \rho}\left(\frac{1}{1+\frac{K^2}{2}}\right)^{1/2}, \tag{2.69}$$

where Ω_p is the plasma frequency given by

$$\Omega_p = \sqrt{\frac{\mu_0 n_e e^2 c^2}{\gamma_0 m}}. \tag{2.70}$$

The new variables are now defined:

$$\eta_l = \frac{\gamma_l - \gamma_0}{\gamma_0 \rho}, \tag{2.71}$$

$$A = \frac{F_1 K k_r u}{4\gamma_R^2 k_u \rho^2}, \tag{2.72}$$

$$\tilde{z} = \frac{2ck_u\gamma_R^2}{\gamma_0^2}\rho t. \tag{2.73}$$

The expressions from Eqs. 2.62, 2.63, and 2.64 are normalized resulting in

$$\dot{\theta}_l = \delta + \eta_l, \tag{2.74}$$

$$\dot{\eta}_l = -\left(A + i\sigma_\gamma^2 \left\langle e^{-i\theta_l}\right\rangle\right) e^{i\theta_l} - \text{c.c.}, \tag{2.75}$$

$$\dot{A} = \left\langle e^{-i\theta_l}\right\rangle. \tag{2.76}$$

The equations are only solved numerically, except for a few idealized cases [36]. This guides us to the simplest case which will lead to a better physical understanding of the process. For a monoenergetic beam (i.e. no energy spread),

the FEL equations are linearized and a trial solution for the field amplitude, $A \propto \exp(i\Lambda\tilde{z})$, is applied to derive the cubic dispersion relation:

$$\left((\Lambda+\delta)^2 - \sigma_\gamma^2\right)\Lambda = -1. \tag{2.77}$$

For illustrative purposes, a first-order solution to Eq. 2.77 can be found by taking the limits of $\delta = 0$ and $\sigma_\gamma = 0$ to give the cubic equation $\Lambda^3 = -1$. The three solutions for Λ describe the physical phenomenon of the FEL collective instability. The real solution is oscillatory, the complex solutions represent the decaying and growing modes. At the beginning of the FEL process, the *start-up regime*, all the modes are of comparable magnitude and begin interfering with each other. After some time, the growing mode dominates, and the electric field grows exponentially. This is referred to as the regime of *exponential growth*. This period of growth ends in the *saturation* regime. In the saturation regime, the linear equations are no longer valid (the description of saturation is non-linear) and numerical methods must be approached.

With this basic understanding, we revisit Eq. 2.73. Assuming the electron energy is centered around the resonant energy ($\gamma_0 \approx \gamma_R$), and $z = ct$, the expression in Eq. 2.73 becomes $\tilde{z} = 2k_u\rho z$. Inserting this form into our test solution gives a mathematically scaled solution for the amplitude: $A \propto \exp(i\Lambda z/L_g)$. The *gain length* of the FEL is defined as

$$L_g = \frac{\lambda_u}{4\pi\rho}, \tag{2.78}$$

which is simply the length required for the field amplitude to increase by a factor of e. It is of practical importance to keep the gain length small. This minimizes the overall length of the undulator, as saturation can be reached earlier. In practice, the gain length of the FEL is derived empirically by measuring the energy as a function of distance along the undulator.

These results are only valid for a monoenergetic beam, whereas when energy spread is introduced the gain of the FEL is negatively affected. The energy spread prevents the electron bunching at the appropriate phase as the electrons have different longitudinal velocities. There have been recent experimental proposals to "pre-bunch" the electron beam (inject a current modulated beam into an undulator) to aid in the efficiency of the amplification process [37].

Saturation is achieved when the electrons stop transferring energy to the radiated field; once the electrons lose enough energy to the field, they no longer satisfy the synchronism condition. There are methods, known generally as tapering, that will extract more energy out of the beam near saturation [25] by varying the undulator parameters (e.g. $K(z)$ or $\lambda_u(z)$) to move the bucket, with the captured beam in it, to a lower energy, hence maximizing the interaction between the electrons and the radiation. The power at saturation is proportional to the FEL parameter and the peak current [38], I_p, of the beam,

$$P_{sat} = \rho \frac{\gamma_0 I_p m c^2}{e} = \rho P_{beam}. \tag{2.79}$$

It is obvious that the FEL parameter plays an important role in the design of FELs, as increasing the FEL parameter reduces the gain length of the system, as well as increases the power at saturation.

2.6 3-D Effects in Free Electron Lasers

The basics of the FEL process remain the same when 3-D effects are taken into account. However, a new *3-D FEL parameter* must be defined that will satisfy the relations from the previous section,

$$\tilde{\rho} = \left(\frac{I}{2\gamma_0 I_A} \frac{F_1^2 K^2}{\left(1 + \frac{K^2}{2}\right)} \right)^{1/2}, \tag{2.80}$$

where I is the current of the electron beam, and I_A is the Alfven current, familiar from plasma physics. Similarly, the space charge coefficient has a 3-D analog given by

$$\tilde{\sigma}_\gamma^2 = \frac{8\tilde{\rho}}{D}\frac{1+\frac{K^2}{2}}{K^2}, \tag{2.81}$$

where $D = 2r_0^2 k_r k_u \tilde{\rho}$ is the *diffraction parameter*, a measure of the diffraction of the propagating radiation beam.

2.6.1 Transverse Modes

In order to achieve transverse coherence, phase information must propagate in the transverse direction. The velocity spread in the transverse dimension of an electron beam is parameterized by the beam *emittance* [39]. The emittance of the electron beam is a measure of its transverse size and divergence. The normalized emittance, $\epsilon_n = \epsilon\gamma$, is proportional to the square of the amplitude of the average betatron oscillations that the electrons exhibit when injected slightly off-axis or off-angle. These additional oscillations reduce the longitudinal velocity. The requirement on the beam emittance is that it must be smaller than the beta function of the electron beam divided by the gain length, $\epsilon_n \ll \beta\lambda/\gamma L_g$. Here, β is a measure of the electron beam envelope (transverse) and is usually on the order of a gain length. In fact, one of the optimum conditions for coherent emission is that the geometric emittance of the electron beam, $\epsilon_n/\beta\gamma$, must be less than the radiation wavelength. This is not a problem for FELs in the visible and infrared regions, such as the VISA experiment, as photoinjectors readily achieve normalized emittances on the order of 1 mm-mrad.

The FEL amplification process is inhibited if the radiation leaks in the transverse dimensions. A characteristic parameter of this type of diffraction phenomena is the Rayleigh length [33], $z_R = k_r w_0/2$, where w_0 is the size of the waist of

the beam. If the gain length is longer than the Rayleigh length, the FEL is said to be *diffraction limited*.

2.6.2 Self Amplified Spontaneous Emission

The initial radiation field taken into account thus far can be of two sources. If the seeding field comes from a laser, commonly called a *seeding laser*, the transverse and longitudinal coherence is preserved throughout the gain process [40]. The other scenario, which is of more interest to the VISA experiments as well as to future x-ray sources, is the *self amplified spontaneous emission* (SASE) free electron laser. The SASE FEL is based on the random phase factors, θ_l, of the electrons in the ensemble at the beginning of the undulator, resulting in a broadband spectrum for the spontaneous emission (undulator radiation) as the seeding signal. The SASE FEL not only drives the radiation at the resonance frequency, but it also amplifies all frequencies within the acceptance bandwidth of the FEL [41]. The relative bandwidth of the SASE FEL under standard conditions of single transverse mode excitation is given by the FEL parameter ($\tilde{\rho} \approx \Delta\omega/\omega$), typically on the order of $10^{-2}-10^{-3}$. We examine in the experiments presented below a scenario in which the bandwidth is strongly enhanced by 3D effects.

The initial ponderomotive phase of the electrons in the ensemble is random, therefore, the electrons will group together randomly. The emitted radiation from these random groups will be dominated by the groups with the most electrons. These fluctuations lead to variations in beam current and are also present in the output radiation energy. It has been shown that since the SASE FEL starts from the shot noise in the electron beam, the output energy distribution also displays fluctuations that follow the gamma distribution [42]. In this statistical treatment

of the SASE FEL, the gamma probability distribution of the radiation energy has a dependence on the number of modes in a radiation pulse (denoted by M).

The explicit value of M is determined by the slippage in the SASE FEL. If the electron bunch length is longer than the slippage, $N_u\lambda$, the radiation's temporal distribution is comprised of numerous modes. The modes, or spikes, originate from the random noise variations in the beam current and the intensity fluctuations follow a gamma distribution. In Chapter 5, an experiment is described where a fully coherent seed signal is provided for the FEL using the output from a preliminary undulator operating in the SASE mode [43]. It is obvious that the only method to generate an x-ray FEL would be to use the SASE approach, as there are no seeds for the amplification process other than spontaneous emission.

2.6.3 Other Electron Beam Effects

From Eq. 2.27, it is obvious that an electron beam with energy spread will affect the linewidth of the emitted radiation. The energy spread of the beam is correlated to the linewidth of the radiation from the FEL. In fact, the energy spread should be less than the FEL parameter ($\Delta\gamma/\gamma < \tilde{\rho}$) otherwise the collective instability is prevented from developing thus the exponential gain is inhibited; this effect is known as Landau damping [44]. The wiggle motion in the undulator is well understood; however, that analysis applies to particles injected exactly on-axis. For particle with a slight injection error, or deviation from the central axis, the electron will additionally oscillate through the undulator with a slower period, often called the *betatron oscillation*. Since some of the longitudinal energy is also transferred to this extra slow oscillation, the on-axis velocity is further slowed down.

In Eq. 2.79, the power at saturation of the FEL radiation is proportional to

the peak current of the electron beam. There are a number of ways to increase the current of the beam, thus yielding higher power. One method is to use a dedicated compressor [16]; another, which was used in the VISA experiment, is to exploit second-order effects in a dispersive section of a beam line transport. Increasing the current of the beam also decreases the gain length, requiring a shorter undulator to achieve saturation and maximize efficiency. Thus it is crucial, for operating a high gain SASE FEL, to achieve the highest possible beam current with a reasonable emittance. One must be careful to compress the beam with care, as excessive compression of the beam leads to an emittance degradation.

Revisiting the ponderomotive phase term from Eq. 2.39, we can write an expression for the slippage,

$$\frac{d\theta}{dt} = k_r c \left(\frac{\beta_z}{\bar{\beta}_z} - 1 \right), \tag{2.82}$$

where, $\bar{\beta}_z$ is the resonant longitudinal velocity. When the electrons travel at the resonant velocity, $\bar{\beta}_z$, the ponderomotive phase from Eq. 2.82 is constant and the synchronism condition is upheld. However, in a realistic scenario, the electrons will have a distribution of velocities. Those with higher energy will move forward with respect to the initial phase; conversely, those with lower energy will move backward. Conceptually, the radiated wave is traveling at the speed of light, while the particles are traveling slower than c. For optimal interaction, the interaction phase between the wave and the undulating particle should be kept constant. Therefore, an ensemble with a larger electron velocity spread, i.e. particle with differing energies, will have a negative effect on the bunching of the electrons in the undulator thus inhibiting the FEL amplification process. However, if the ensemble has a narrow energy distribution, all the particles lie near the resonant energy. Particles with $\dot{\theta} < 0$ slow down while particles with $\dot{\theta} > 0$ speed up and bunching occurs at the period of the radiated field.

The electron beam *chirp* refers to the, usually linear, correlation between the electron beam energy and the longitudinal position within that bunch,

$$\frac{\Delta\gamma}{\gamma} = \alpha\frac{l}{l_b}, \tag{2.83}$$

where l represents the position along the longitudinal bunch, and l_b is the bunch length. The chirp parameter is characterized by α. A chirped electron beam, amplified through the FEL process, will produce frequency-chirped radiation [45], $\omega_j = \omega_0 + 2\alpha t_j$, where the jth electron emits at a frequency ω_j. For the chirp correlation to hold consistent with the FEL instability, the slippage occurring during passage through a gain length of the undulator (the cooperation length) must be short compared to the distance over which the resonant frequency changes by a gain bandwidth. In a proposed experiment, a monochromator will sample a slice of a chirped radiated SASE pulse to use as a seed for a second undulator which acts as an FEL amplifier [43]. This topic is explained in detail in Chapter 5.

CHAPTER 3

Description of the Experiment

3.1 Accelerator Test Facility

The VISA experiment is a multi-institutional collaboration and its success has depended on the efforts of many parties. The VISA experiment is hosted by the Accelerator Test Facility (ATF) at Brookhaven National Laboratory (BNL) in New York. The ATF is a state-of-the-art complex, which has garnered international accolade for its pioneering work in advanced accelerators, plasma and laser physics, and FEL studies. Since 2001, the ATF has accommodated more than a dozen different experiments along five separate beamlines [46]. Among these experiments is the VISA project, for which the ATF staff provides maintenance of the beamline (eg. vacuum pumps, magnet power supplies, etc.) and assistance to the experimenters by addressing safety and logistical concerns as well as computer and data acquisition support.

3.1.1 The ATF Laser

The core capabilities of the ATF provide a stable 70 MeV, high-brightness electron beam based on a state-of-the-art photoinjector and laser system. The Nd:YAG (often futher abbreviated to YAG) laser drives the rf photocathode. It is housed in a class 100 clean room environment. The YAG laser is capable of

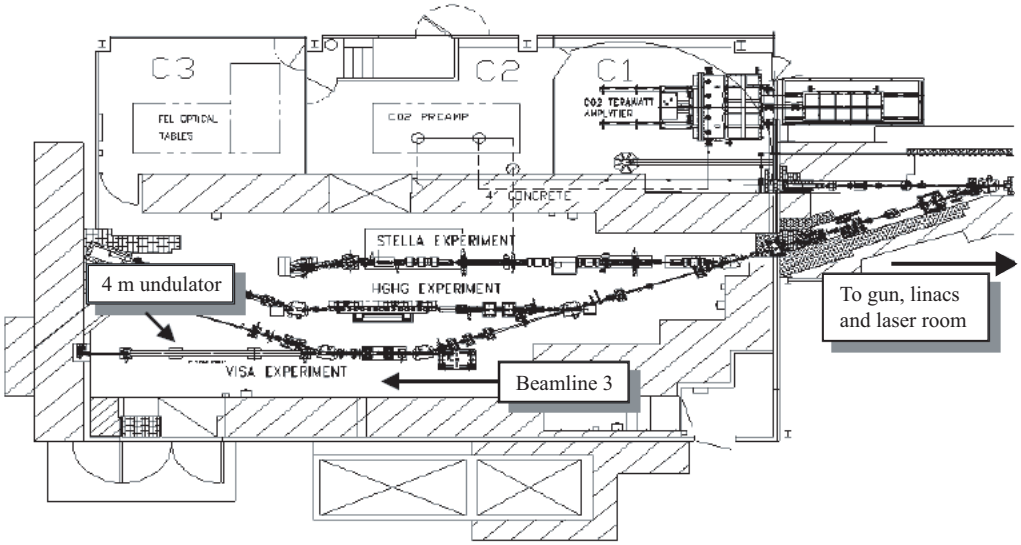

Figure 3.1: A blueprint drawing of the Accelerator Test Facility layout. The VISA Experiment is located in the Experimental Hall along Beamline 3 (courtesy M. Woodle).

producing up to 50 μJ of UV on the photocathode, with a pulse length of 8 ps. The typical values for the VISA experiment ranged from 8 - 20 μJ. The YAG laser emits near the 1 micron wavelength (1064 nm), then is quadruply frequency multiplied, or reduced down, to 266 nm and shined on the photocathode. A diagnostic pick-off, placed just upstream of the insertion port before the cavity, is used to image the spot on the cathode, and conduct other measurements on the laser beam [47].

The uniformity of the electron emission from the cathode affects the overall emittance of the electron beam, which is commonly used as a figure of merit of its quality. The laser uniformity is limited by the minimization of timing and phase errors. These errors, during propagation to the photoinjector, lead to fluctuations in the laser intensity shined on the photocathode [48]. Such changes in laser intensity negatively affect various beam parameters, including emittance, energy and charge and also affect the overall stability of the generated beam. Daily

Parameter	Symbol	Value
Charge	Q	500 pC
Energy	γ	70 MeV
Emittance	ϵ	2 mm mrad
Pulse length	l_p	10 ps
Laser energy on cathode	E_{laser}	8-18 μJ
Repetition Rate	f	1.5 Hz

Table 3.1: Typical ATF operating parameters for the VISA experiments.

maintenance of the laser helps reduce the controllable sources of non-uniformity to improve the emittance of the beam.

3.1.2 The ATF Photoinjector

The photoinjector has been conceptually designed to produce high-brightness electron beams. The laser pulses incident on a photocathode (Magnesium or Copper) generate short bunches of electron beams. The cathode is housed in a rf structure operated at high accelerating fields, which accelerate the electrons to relativistic energies.

The ATF photoinjector (or gun) has gone through many changes since the birth of the facility. During the VISA tenure, the ATF successfully used two different guns. For the measurements taken during VISA I and the initial part of VISA II, the ATF employed Gun III, which was developed as a joint UCLA-BNL-SLAC collaboration. This gun regularly produced a photoelectron beam with an emittance between 1-2 mm-mrad at a charge of 0.5 nC [49]. At a charge of 1 nC and 10 ps pulse length, the measured emittance was 2.6 mm-mrad for this photoinjector [50]. The gun is able to generate a photoelectron beam with an energy

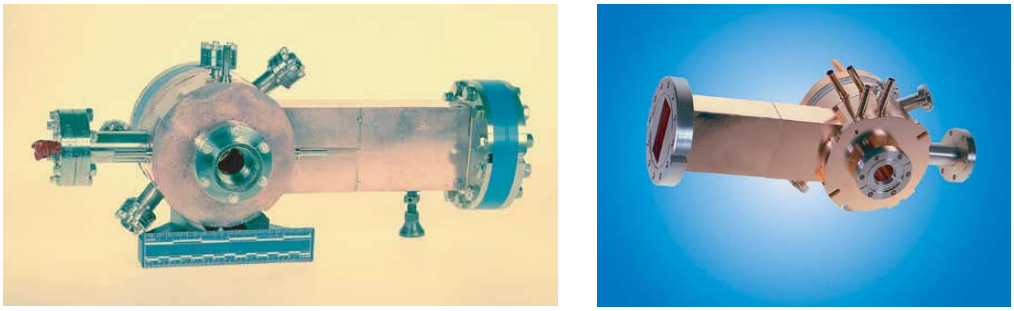

Figure 3.2: Photographs of the previous photoinjector, Gun III (left), and the currently installed Gun IV (right), at the ATF (courtesy V. Yakimenko).

of 4 MeV; the remaining acceleration is handled by two accelerating structures, discussed in Section 3.1.3. Charge is monitored via a retractable Faraday cup located directly after the gun exit, before the linac section. A solenoid provides external focusing for the beam to control its transverse size and achieve *emittance compensation* [51], a process where emittance growth due to linear components of space-charge forces are compensated. Emittance compensation has successfully been demonstrated at the ATF photoinjector [52].

The rf power scheme at the ATF utilizes a number of components and requires constant attention for reliable operations. The 2856 MHz low-level signal, multiplied from the master oscillator, is attenuated and phase shifted before heading to the kilowatt amplifier. The linac operator has the ability to control the rf power and phase via the computer control system. An XK5 type Klystron tube, which generates up to 25 MW of power, is used to power the gun as the 266 μm UV light, frequency multiplied from the YAG laser, is shined on the photocathode. A separate trigger ensures the synchronism between shots from the laser and the Klystron tubes. Figure 3.3 summarizes the rf power structure that is used at the ATF.

Due to multipactoring in the gun, a new photoinjector (Gun IV, Figure 3.2)

was installed in March of 2004. Multipactoring is a phenomenon whereby electrons emitted from the cathode, are deflected and impacted on the inner surface of the rf cavity generating secondary sources of electron emission [53]; this process may self-amplify and produce cavity breakdown. This is responsible for field restrictions, thus limiting acceleration, and has been observed to develop with the age of the cavity at the ATF. Gun IV is a 1.6 cell, pi-mode copper photoinjector which sustains field gradients of 110 MV/m in the full cell and 160 MV/m in the half cell. It has a larger aperture than the previous gun allowing a larger laser spot size on the cathode (as wide as 4 mm). Under ideal conditions, it is capable of generating a stable beam with energy as high as 5.5 MeV [54].

A variety of techniques is implemented at the ATF for improving any deteriorating aspects of the accelerator. The ATF uses a process called *laser cleaning*, where the YAG laser is focused on the surface of the cathode with high energy, as part of its maintenance. Laser cleaning is based on vacuum observation while adjusting the laser energy. It is used to occasionally remove surface contaminants from the copper or magnesium cathode that may have developed over the course of months of operation. Laser cleaning improves the quantum efficiency of the gun, the ratio of emitted electrons to incident UV photons, to 0.5% immediately after the process and to about 0.1% for up to a month afterwards [55].

3.1.3 The ATF Linac Section

The ATF uses two SLAC type linac structures (S-band, 2856 MHz) to accelerate the beam to energies up to 71 MeV. An additional XK5 type Klystron tube, which generates up to 25 MW of power, drives the linac sections. A modulator provides the tube with the necessary high voltage. There is a mechanical, high power phase shifter that controls the relative phase between the two linac sections.

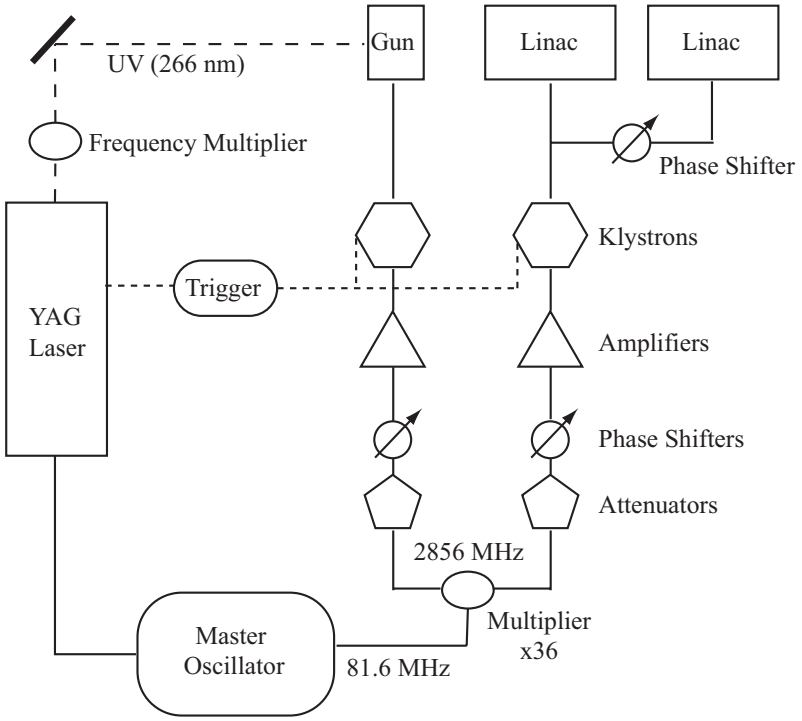

Figure 3.3: A schematic diagram of the rf power and YAG laser setup at the ATF.

The phase shifter is under control of the ATF operator. The gain in energy, in practical laboratory units, is [49]

$$\Delta E[\mathrm{MeV}] = 10^8 \cdot \sqrt{P[\mathrm{MeV}]} \cdot 395 \cdot I[\mathrm{A}]. \tag{3.1}$$

3.1.4 Control System

The ATF computer control system was designed for maintenance and diagnostic operations of the accelerator as well as to service the experimenters. Hence, the computer control system is connected to the most widely used equipment in the ATF, including magnet power supplies, rf systems, laser diagnostics, electron beam profile monitors, digital frame grabbers and vacuum gauges [56]. The ATF control system was built around a VAX 4200 computer, and data acquisition was

handled via CAMAC hardware [57]. The control system displays were built using Vsystem (a commercially available package) and features a graphical user interface that is navigable by any of the trained linac operators. There are two video frame grabbers which are used to collect shot-to-shot statistics about the electron beam profile. Online applications developed at the ATF, using MathCad software, can monitor and control accelerator operations directly from a MathCad worksheet [58]. For example, using a MathCad worksheet, emittance measurements and automatic generation of photoinjector performance statistics are made daily to provide a quantifiable merit of the beam quality. The knowledge greatly helps with the maintenance of the day-to-day consistency of beam parameters and is essential for users' analyses of acquired data.

The near decade old ATF computer control system was upgraded during the tenure of the VISA II experiment. The renovation included a move toward a more reliable 8-way Intel Pentium computer and 100 MHz Ethernet communications replacing the existing 5 MHz CAMAC highway [59]. This resulted in a marked improvement in terms of control and speed, as well as a more intuitive feel to tracking saved data. Most of the original interfaces, including MathCad worksheets, were preserved, which minimized retraining for users and operators.

Most of the VISA controls are integrated into the ATF control system. Retractable profile monitors and imaging systems, remote controlled flip mounts for the optical transport line, the alignment laser shutter, and the undulator steering magnet power supply excitation levels are all incorporated into the ATF computer control system. Discussions regarding the technical aspects of the undulator diagnostics are reserved for Section 3.3.2.

Radiation measurements from a Molectron brand energy-meter (Model No. J3s-10) give a signal that is displayed on an oscilloscope in the control room. Via

GPIB communications, the information from the scope is incorporated into a pre-written MathCad worksheet that collects and re-displays the data in a more manageable spreadsheet format.

The Ocean Optics spectrometer (Model number USB2000), used for measuring the IR spectrum emitted from the FEL, is *not* integrated into the ATF control system. Rather, the spectrometer has a dedicated laptop PC (Dell C60, Pentium III, running the MicroSoft Windows 2000 operating system) which operates proprietary software (Ocean Optics) for spectrum acquisition and display. The spectrometer uses USB communications, converted via an Ethernet bus to overcome the logistical concern of data loss over a USB cable of length 100 m (the approximate distance from the undulator in the Experimental Hall of the ATF to the Control Room). Two filter wheels, used for modifying the input spectrum, are also controlled by the same computer via an ethernet-serial cable bus (Figure 3.4). The laptop computer is located in the Control Room where the operator has complete access to all of the ATF controls and diagnostics.

3.2 Beamline Transport

In the context of charged particle beams and FEL physics, the beamline transport is the array of magnetic elements (also referred to as beam optics) arranged in between the accelerating section and the undulator. The purpose of the transport is to deliver an electron beam with appropriate parameters to the undulator. The beam requirements for a SASE FEL are very stringent, necessitating that the transport optics and diagnostics are well calibrated and understood. Manipulation of the collective beam parameters is accomplished by the calculated placement of directed magnetic fields along the beamline. Dipole magnets are used to change the trajectory of the beam; quadrupoles are used as linear focus-

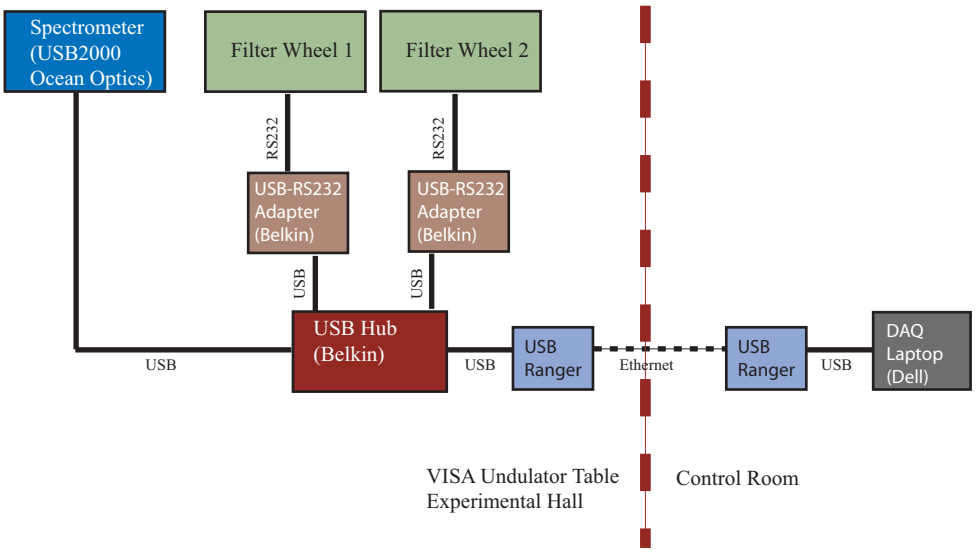

Figure 3.4: A block diagram of the control setup for the VISA components not integrated into the ATF computer control system. The spectrometer and two filter wheels are controlled via serial ports which are converted through an ethernet bus, then amplified and sent to the control room.

ing elements to control beam size and shape. Additional trim coils (also called steering magnets) are used for local corrections to the beam trajectory.

The transport to the VISA undulator can be divided into three distinct sections (Figure 3.5); the moniker of each of these sections has been adopted from the vernacular of the ATF. The H-line is the linear transport directly after the accelerating sections and has 3 sets of quadrupole triplets for focusing, as well as numerous trim coils for steering. The F-line is the dispersive line of the transport that is accessed through a 20° bend dipole magnet. The F-line contains focusing quadrupoles, steerers, as well as sextupole magnets for second-order corrections that were installed specifically for the VISA II experiment. The F-line also contains a high energy slit (HES) which is an adjustable slit that ranges from completely closed up to a 10 mm wide aperture. The HES is located in the beam path at a high dispersion, yet small betatron beam size, point and is

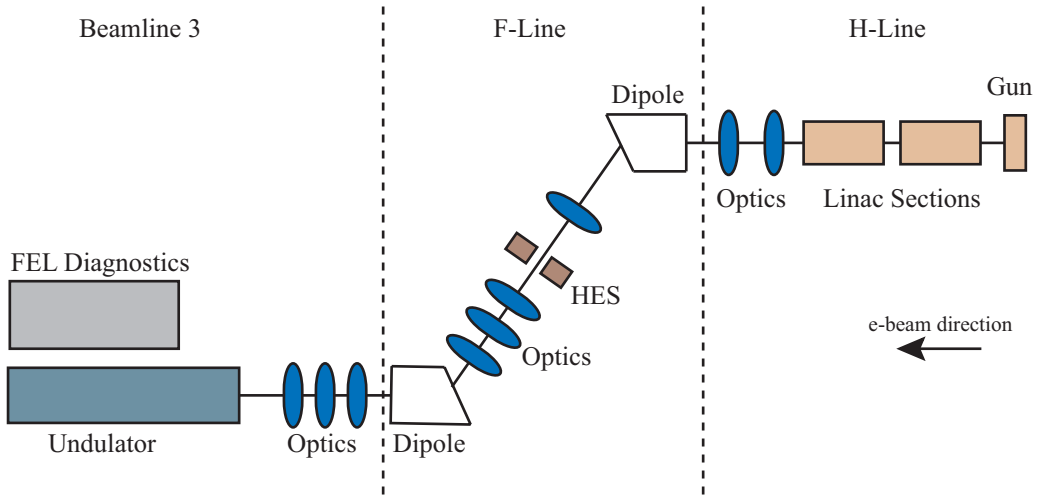

Figure 3.5: A block diagram of the ATF beamline transport with various landmarks labeled (not to scale).

used to monitor the energy and energy spread of the electron beam. The F-line terminates with a second dipole (20°) into Beamline 3 (BL3). BL3 contains the final focusing quadrupole triplet used for matching the electron beam Twiss parameters into the VISA undulator. The undulator is located at the downstream end of BL3). The alignment laser (reference laser) used in the VISA experiment is located at the head of BL3.

In most cases, the topic of transport is platitudinous, however the ATF beamline transport, in particular the F-line, has brought some interesting points to attention. In the VISA runs, an electron beam pulse compression mechanism, based solely on the magnet elements of the transport (i.e. no external compressor), was discovered. Ultimately, this compression was responsible for the observed sustained high-gain lasing. In the VISA II runs, there is an attempt to control the pulse compression mechanism by the addition of second-order magnetic correctors (sextupoles). Although the elimination of compression would be ideal, simulations have shown that even minimal lasing requires an increase in

Parameter	Symbol	Value
Undulator period	λ_u	1.8 cm
Number of periods	N	220
Gap	g	6 mm
Maximum B field	B_{max}	0.75 T
Undulator parameter	K	1.26
Length of FODO cell	L_{FODO}	24.75 cm
Quadrupole focusing gradient	g_f	33.3 T/m
Trim coil field	B_{trim}	50 G
Trim coil length	l_{trim}	20 cm

Table 3.2: A list of the VISA undulator parameters.

peak current achieved by compression.

3.3 Undulator

The centerpiece of any FEL experiment is the undulator employed. The VISA undulator was designed for the purposes of understanding some properties of the far more grand Linac Coherent Light Source (LCLS) project at SLAC. The design and subsequent construction of the VISA undulator involved a collaboration of many scientists and engineers. In this section, details of the design, construction, and assembly of the undulator are discussed. The intra-undulator diagnostics for both electron beam and FEL radiation, and alignment issues are also addressed.

The VISA undulator (Figure 3.6) is a 4 meter undulator, comprised of four 1-meter segments. There are a total of 220 periods, or 55 periods per undulator segment. Each period has a length of 1.8 cm. The undulator is comprised of per-

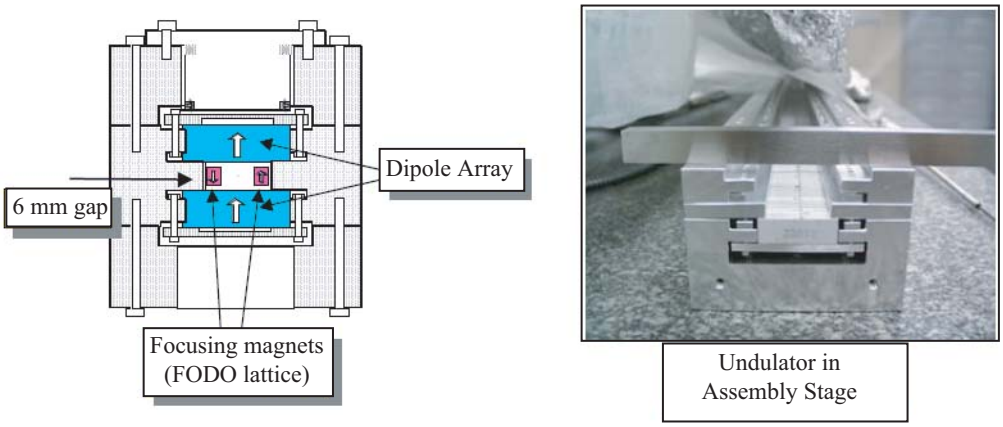

Figure 3.6: A schematic of the VISA undulator design (left) and a photograph of the undulator (right) from the initial building phase of the program (courtesy A. Tremaine).

manent magnets arranged in a pure Halbach geometry [60]. The magnet blocks are NdFeB and have a height of 10 mm and a thickness of 4.5 mm. To maintain an average beta function near 30 cm (per the original design) [61], a focusing FODO (a periodic arrangement of focusing quadrupole - drift - defocusing quadrupole - drift) lattice is superimposed on the undulator and provides extra focusing. The addition of the extra focusing was necessary to reduce the saturation length by 18.5% compared to the same undulator without the focusing array [62]. The FODO lattice magnets have dimensions of 30 mm x 4 mm x 4.5 mm. The magnet positions and locations are not adjustable. There are 4 (four) FODO cells per undulator segment (16 total); each FODO cell is 25 cm in length. The magnetic field gradient in the quadrupoles is 33 T/m [63]. After careful detailed magnetic measurements, shim magnets are used to correct excessive field gradient errors and minimize trajectory errors [64].

3.3.1 Alignment and Support Structure

The undulator is housed in an external aluminum chamber under vacuum. The vacuum chamber is supported on a five-legged table and is constructed out of 2 sections (one section is 2.5 m long and the other is 1.5 m). The two segments are bolted together with an O-ring seal. The vessel is maintained at a pressure of 10^{-8} Torr during operation, close to two orders of magnitude better than initially established requirements. Trim magnets (or steering magnets) are installed external to the vacuum vessel. The trim magnets are capable of carrying a current of 5 Amps, creating 50 Gauss fields on-axis for aid in corrections to the electron beam trajectory [63].

During its initial installation, rough alignment, accomplished by standard surveying techniques, brought the undulator axis to within 200 μm straightness; this was sufficient for initial gain measurements of the undulator [65]. The beamline reference laser, which has a secondary purpose for testing diagnostics, was used to achieve alignment errors of less than 20 μm [66]. The undulator alignment was maintained as such for the entire run of the VISA I experiment.

The undulator was kept under very restrictive laboratory conditions during the time between the initial VISA runs and the later runs for VISA II. The undulator alignment was confirmed for the VISA II segment of the experiment using an optical CCD technique. The joints connecting adjacent undulator segments are fiducialized. Using the optical technique with CCD cameras, the misalignment between segments was measured with near micron level accuracy and compared to that of the VISA I runs. Figure 3.7 shows a sample of the fiducialized undulator segments that were measured. There were no notable differences in the observed values and it was determined that undulator straightness was adequate for the experiment continuation. The beam reference laser studies also confirmed that

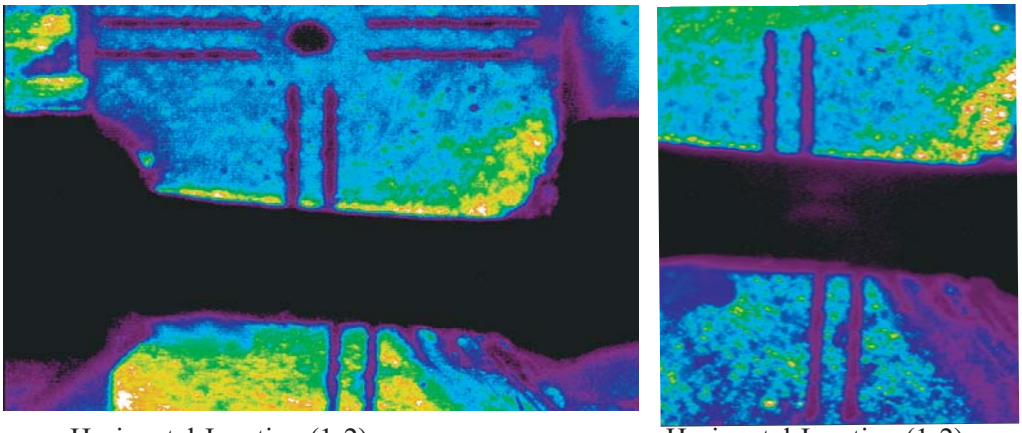

Horizontal Junction (1-2)
Measured October 2002 - 45 microns
VISA II

Horizontal Junction (1-2)
Measured 2000 - 45 microns
VISA I

Figure 3.7: An image of the fiducialized undulator segments used for alignment. The measured offset of fiducials is 45 microns for the original VISA runs (right) and the current VISA II runs (left) confirming the lack of motion of the undulator during down time.

the undulator diagnostics had not undergone any noticeable movements during the down time between the VISA runs. Hence, it was not required to re-pump and re-align the undulator for the measurements made during the VISA II runs, saving the experiment a considerable amount of time and finances. Intra-undulator diagnostics required some minor realignment.

Finally, electron beam trajectory measurements were made as a definitive verification. After high energy running conditions in the accelerating sections were re-established, and appropriate electron beam tunes were implemented, the electron beam was transmitted through the undulator. Once the alignment laser was centered through the profile monitors along the undulator and the reference line was determined, the electron beam centroid versus the alignment laser position was plotted along the undulator (Figure 3.8). This final step verified the alignment.

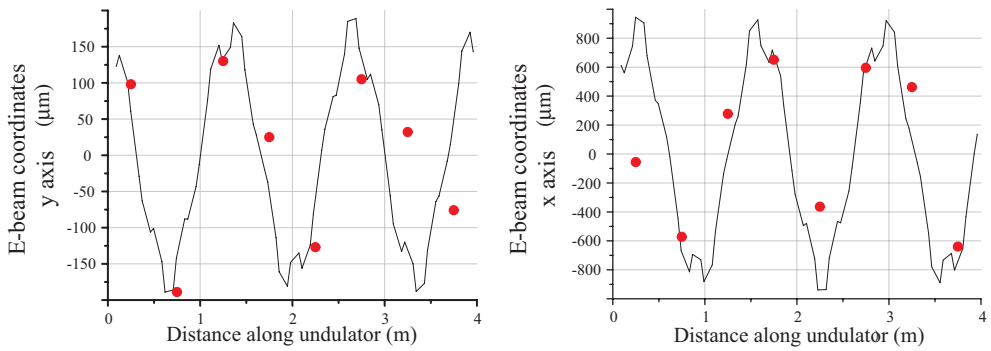

Figure 3.8: The electron beam trajectories through the undulator for the y-axis (left) and the x-axis (right) relative to the reference laser. Points represent measured data and the solid curve represents the theoretical trajectory.

The alignment laser is a fiber coupled, red diode laser manufactured by the Melles Griot corporation (Model No. 06DLL633) and is mounted in a secure enclosure at the head of Beamline 3. The laser has an output power of 3 mW, a wavelength of 655 nm, and a near 100 % circular spot size of 7 mm (as specified by the manufacturer). Thermal equilibrium of the laser is achieved about 20 minutes after turn on. A spot size of less than 2.2 mm must be maintained through Beamline 3 and the 4 m undulator since the scintillators on the beam profile diagnostics have a height of 2.2 mm (Figure 3.9).

As seen in Figure 3.10, an array of lenses and adjustable mirrors serve to telescope and align the alignment laser beam through the undulator, maintaining a reasonable spot size throughout. The laser optics are located in an enclosure to minimize air currents which may affect the stability of the beam. A cold mirror, or combining mirror (which reflects short wavelengths and transmits long wavelengths), is used to co-align the red diode laser with Nd:YAG laser (1064 nm) that is used for the seeded FEL experiments (Chapter 6.1) through the VISA undulator. The laser is aligned using two reference targets (Figure 3.10). The first target is located inside the enclosure on a retractable mount; the second

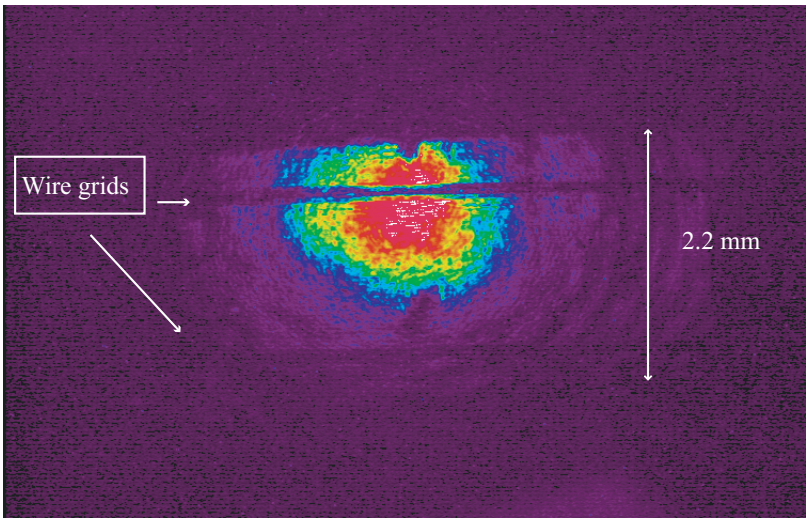

Figure 3.9: A false-color image of an undulator profile monitor with the alignment laser. The wire grids are placed on the 2.2 mm wide mirror.

target is fixed and located after the undualtor exit. The targets are imaged via CCD cameras. The alignment process entails the fine tuning of the two adjustable mirrors to control position and angle of the beam as observed on each of the two targets. The alignment procedure is repeated prior to each experimental run to ensure consistency of the measured parameters.

3.3.2 Diagnostics

Diagnostics for the VISA undulator were designed to be multifunctional and compact as there are restrictive spatial constraints due to the lack of convenient access to the undulator interior. There are 8 diagnostic ports along the undulator spaced 50 cm apart starting at 25 cm after the undulator entrance. Each diagnostic port is fitted with a profile monitor.

The profile monitors incorporate double sided silicon mirrors which give the availability to measure both electron beam properties as well as FEL radiation characteristics. The double sided mirrors are mounted in vacuum on two-stage

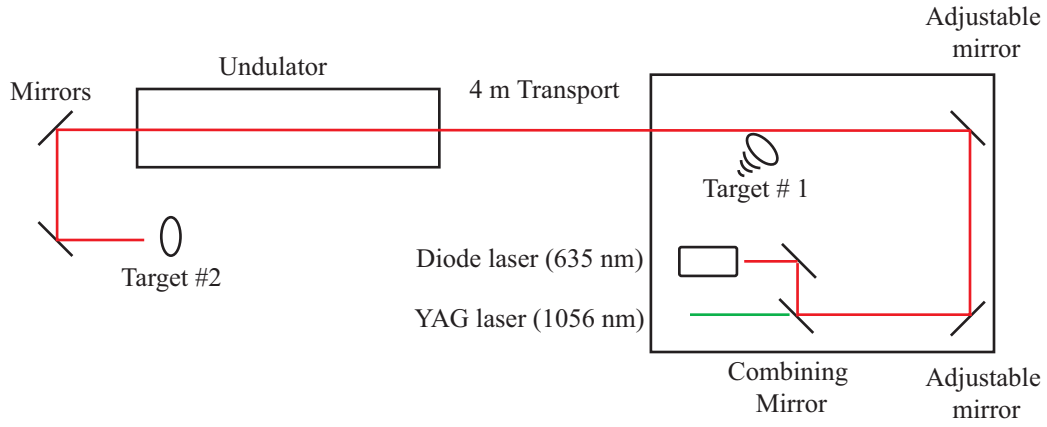

Figure 3.10: A schematic of the VISA alignment laser (diode laser at 655 nm).

actuators (Figure 3.11). As the mirrors are actuated into the first position, the electron beam striking the surface produces optical transition radiation (OTR) [67]. The resultant light is directed outside the undulator vessel through a window, into an optics relay system comprised of two mirrors, a magnifier, a lens, a CCD camera, and an optional polarizer (Figure 3.12) [68]. The polarizer is used at high gain to separate the radially polarized OTR emitted by the electron beam striking the mirror from the linearly polarized emission. The information retrieved includes transverse electron beam sizes and centroid positions and intensity. The mirror is calibrated with wires spaced 2 mm apart. In the actuators' second position, the silicon mirror reflects FEL light out of the undulator box through a window (on the opposite side). On this side of the undulator table, the radiation is characterized with numerous instruments, including CCD cameras for beam sizes, energy-meters, spectrometers, a novel diagnostic device termed the *double-differential spectrometer*, and a fiducialized screen to resolve the angular distribution of the radiation.

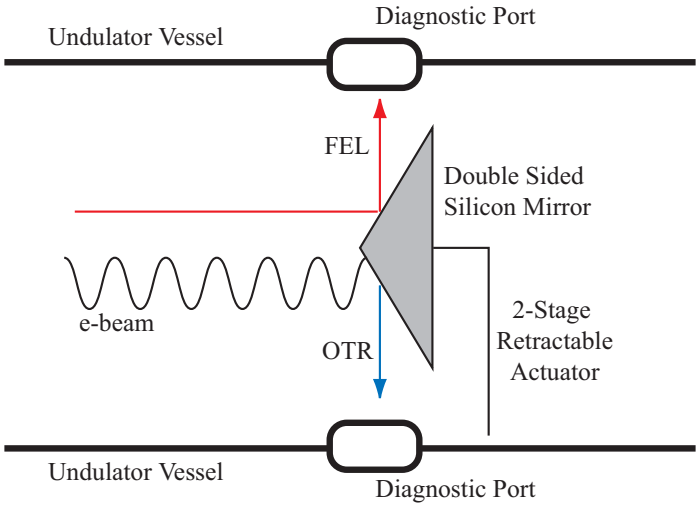

Figure 3.11: A sketch of the VISA undulator profile monitor (not to scale).

3.3.3 Optical Transport Line

The optical transport line for the VISA undulator is located on the near side, opposite to the side with the OTR diagnostics. It is used to relay the extracted FEL radiation from each undulator port, as well as the undulator exit, to individual measurement diagnostic devices.

The optical transport line consists of a series of lenses and mirrors placed on remote control flip mounts in order to be retracted from the radiation transport (Figure 3.13). The flip mounts are manufactured by New Focus and are activated by TTL inputs integrated into the ATF control system. Lenses (f = 25 cm) are placed 50 cm apart to image the radiation to the diagnostics, with a spatial inversion every period.

An interesting problem arises when looking at the odd numbered ports. Due to the spatial inversions incurred through the optical transport line, a delay line was added so that the imaged light encounters an even number of optical focusing elements, regardless of which port it is emitted from. The delay line is activated

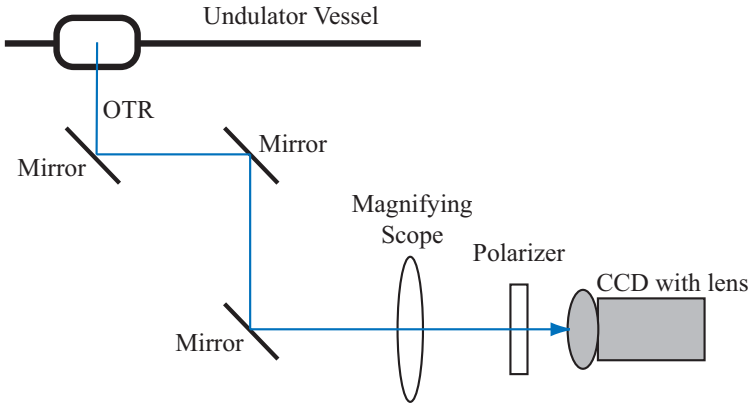

Figure 3.12: The telescopic setup used to observe optical transition radiation (OTR) from the electron beam at the VISA Undulator.

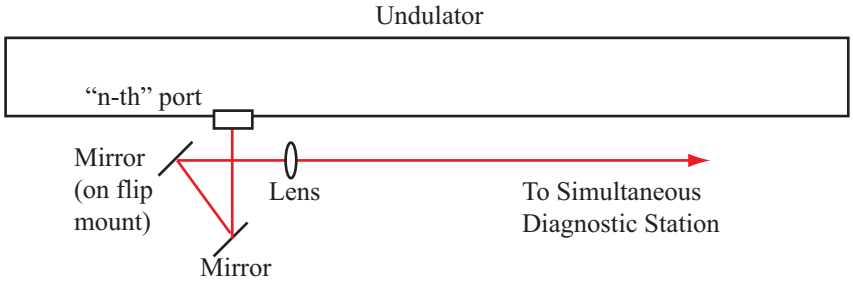

Figure 3.13: A sketch of a typical transport station of the optical transport line. A retractable mirror relays the radiation (through focusing lenses) to the diagnostics station.

when studying light from an odd numbered port (i.e. ports 3, 5, 7). The optical transport line terminates into the simultaneous diagnostics station, discussed in Section 3.3.4.

There are two remote controlled filter wheels along the transport line (Figure 3.15). One filter wheel is loaded with neutral density filters which attenuate the radiation when the diagnostics begin to saturate at high gain. The second filter wheel is loaded with irises of increasing apertures to collimate the beam. Unfortunately, due to spatial constraints in the Experimental Hall near the VISA undulator, any useful information from port 1 of the undulator had to be sacri-

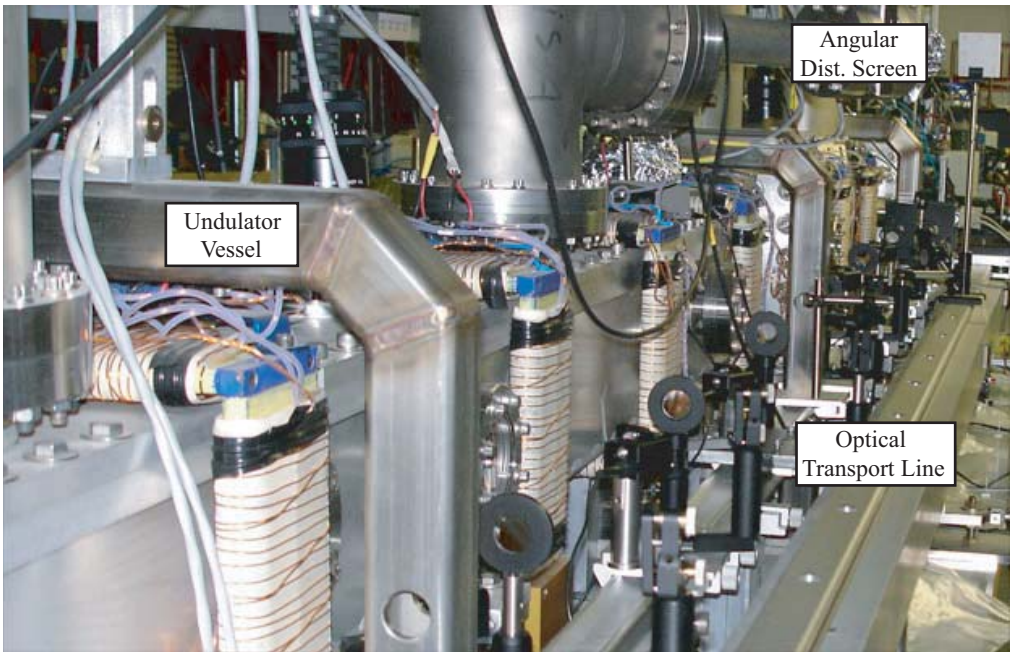

Figure 3.14: A photograph of the optical transport line viewed upstream from the undulator exit, with the angular distribution screen visible in the far corner.

ficed in order to create the needed space for the numerous FEL diagnostic devices. As very few photons were detected from this port during the VISA I runs, mostly due to spontaneous undulator radiation, the loss is not significant for gain length measurements.

3.3.4 Simultaneous Diagnostic Station

The optical transport line relays the emitted FEL radiation from any one of the eight undulator extraction ports, or the undulator exit, to the simultaneous diagnostic station. Figure 3.16 displays a schematic of the setup for the diagnostic station. This station rests atop an optical breadboard and consists of a CCD camera for imaging the light, an energy-meter, a spectrometer, and an extra slot available for other diagnostics such as a frequency resolved optical gating (FROG) device. The intent of the stand is to be efficient and modular, where diagnostics

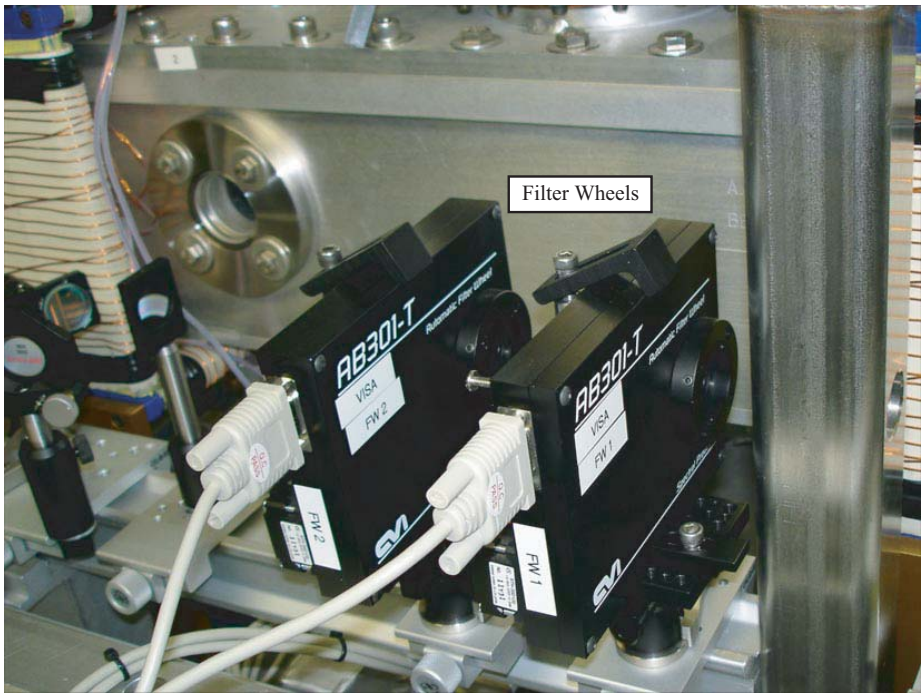

Figure 3.15: A photograph of the two remote controlled filter wheels used for attenuation and collimation of the FEL radiation.

can be easily transposed or replaced without the need for tedious re-alignment. There are three 50% beam-splitters, with the CCD the farthest away as it requires the fewest number of photons of the three mentioned detectors. A photograph of the simultaneous diagnostic station is shown in Figure 3.17. The diagnostics are calibrated prior to each run with the alignment fiber coupled reference laser.

For redundancy, there is an additional CCD camera and energy-meter placed at the end of the table to analyze the radiation properties at the undulator exit. In fact, these two diagnostics are mainstays retained from the VISA I runs and are useful for cross calibrating the measurements taken at the simultaneous diagnostic station. The measurements are made by allowing the FEL light to transport to a 45° copper mirror placed 1 m from the undulator. A remote control flip mounted mirror allows the user to toggle the radiation between the CCD camera or the

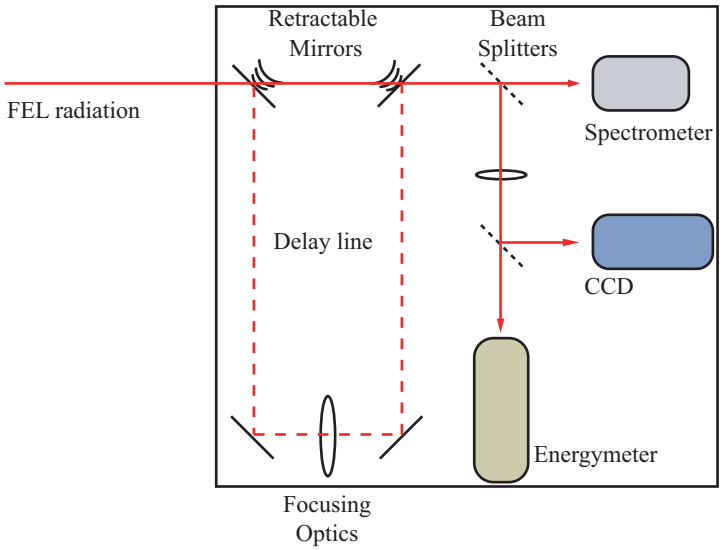

Figure 3.16: A schematic of the simultaneous diagnostic station.

energy-meter. Unfortunately, this does not allow a simultaneous shot-to-shot acquisition so averaging measurements are relied upon.

The energy-meters used at VISA are manufactured by Molectron (Model No. J3S-10). They can be operated in two modes (long and short wavelength); each mode has its own calibration. The CCD cameras used at VISA are manufactured by Cohu Electronics (Model No. 2622-1000). The spectrometer is manufactured by Ocean Optics (Model No. USB2000).

Far-field angular distribution patterns are measured by allowing the FEL radiation to propagate to a screen located approximately 3 meters downstream. The screen is calibrated with fiducials and is imaged with a CCD camera focused on its center. Again, this diagnostic is calibrated with the alignment fiber coupled laser. The FEL radiation is propagated to this screen without the aid of focusing lenses.

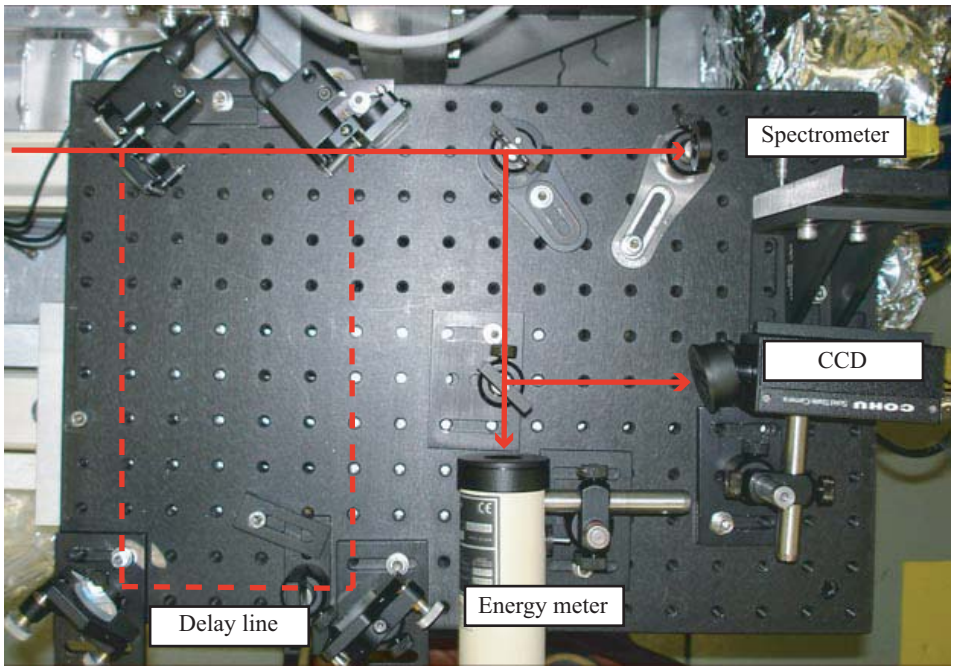

Figure 3.17: A photograph of the simultaneous diagnostic station installed along the optical transport line.

3.3.5 Advanced Diagnostics

There are a number of advanced diagnostics in use at the VISA experiment. These diagnostics are not commercially available, require custom levels of specifications, and have been developed uniquely for the VISA and VISA II experiments.

The double differential spectrometer incorporates focusing cylindrical lenses, an adjustable slit, and a set of gratings. A dedicated radiation extraction port at the end of the undulator is used to transport light into the double differential spectrometer. It is used to directly unfold the correlation between the angles and frequencies of the emitted FEL radiation. The experimental scheme and the underlying physics behind the double differential spectrum are discussed in detail in Section 4.3. Experimental data, calibration procedures and suggested improvements are also presented in this section.

A second advanced diagnostic in the VISA program incorporates the modified frequency resolved optical gating (FROG) technique. This diagnostic must be modified specifically to measure the expected chirp on the FEL radiation produced from the VISA II experiment as well as investigate the large spectral bandwidth observed in the transitional VISA IB experiment. This is discussed in detail in Section 5.4.

CHAPTER 4

Results and Analysis of the VISA IB Experiment

This chapter recounts the details of the experimental results, and ensuing analysis, of a transitional SASE FEL experiment conducted in 2003. In order to understand the context and relevance of the present measurements (called VISA IB), a review of the prior results from the VISA experiment is mandatory. In the first section (Section 4.1), a recap of the VISA I experiment and its major results is presented. The summary is followed by an explanation of the observed phenomenon, focusing on the anomalously wide bandwidth of the high gain FEL wavelength distribution. The computational model and analytical calculations are discussed in Section 4.2.4. The chapter concludes with Section 4.3, a brief look into a novel diagnostic whose purpose is to further enhance the understanding of the relationship between the spectral distribution and the associated observation angles. This diagnostic, termed the *double differential spectrometer*, was developed exclusively for the VISA program by the Particle Beam Physics Laboratory at UCLA.

4.1 Summary of VISA I

In order to understand the context and relevance of the present measurements, a review of the prior results of the VISA experiment is needed. In 1998, the VISA (Visible to Infrared SASE Amplifier) experiment was proposed to study the effects of a high gain SASE FEL with a strong focusing undulator. This study was fabricated as a precursor to the more elaborate LCLS (Linac Coherent Light Source) SASE FEL planned for development at the Stanford Linear Accelerator Center (SLAC). Indeed, in 2001 the VISA experiment successfully demonstrated a high gain SASE FEL, with energy saturation observed within the 4-m undulator and a radiation wavelength of 840 nm [18]; these results aided in proceeding the LCLS project to construction. The measured gain length was 18.5 cm, the shortest gain length recorded in the NIR wavelength regime. High gain lasing was achieved in large part due to an atypical electron bunch compression mechanism that was discovered, and subsequently exploited, during the experimental runs. Large second-order longitudinal time dispersion, quantified by the transport coefficient T_{566} [69], in addition to off-energy operation, yielded pulse compression in the dispersive section of the beamline transport. The pulse compression effectively increased the peak current of the electron bunch from 55 A to 240 A, ensuring high gain SASE FEL operation.

The evolution of the electron beam properties, and the subsequent FEL radiation, was studied with a start-to-end simulation code suite that models the beam interactions from its inception at the photocathode to the end of the undulator. The simulation suite is comprised of three individual codes, each one dedicated to a specific section of the complicated model. The electron beam dynamics in the gun and linacs are modeled with `PARMELA` [70]. `PARMELA` is an accelerator code that was developed at Los Alamos National Laboratory, and has since been

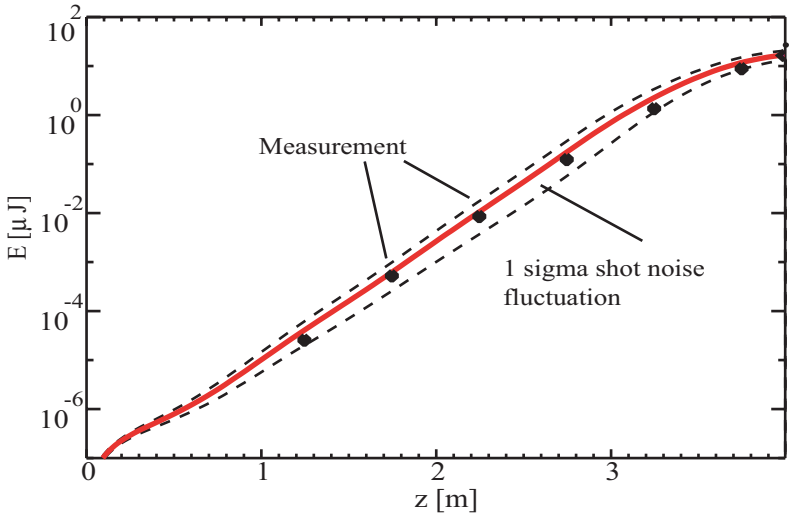

Figure 4.1: The VISA I energy gain curve shows excellent agreement between the computational model and experimental data.

upgraded at UCLA [71]. `PARMELA` is used to compute the effects on the beam phase space due to both applied fields and collective effects due to the electron beam itself, from beam generation at the photocathode to the end of the accelerating sections. The electron beam transport, from the exit of the linac to the entrance of the undulator, is modeled with `ELEGANT` [72]. The code `ELEGANT` was developed and rigorously maintained by M. Borland and others at Argonne National Laboratory. `ELEGANT` is a very expansive tool with numerous features, but for the purposes at VISA, it is strictly used for transport calculations, particularly for studying the effects of compression, including coherent synchrotron radiation, along the dogleg. The electron beam and FEL radiation inside the undulator and beyond is modeled with `GENESIS 1.3` (commonly referred to as `GENESIS` in this document and the FEL literature) [73]. The current version of `GENESIS` is maintained and supported by S. Reiche at the UCLA Particle Beam Physics Laboratory. The benchmarking of simulations against the experimental knowledge of the beam production and evolution was a major achievement for

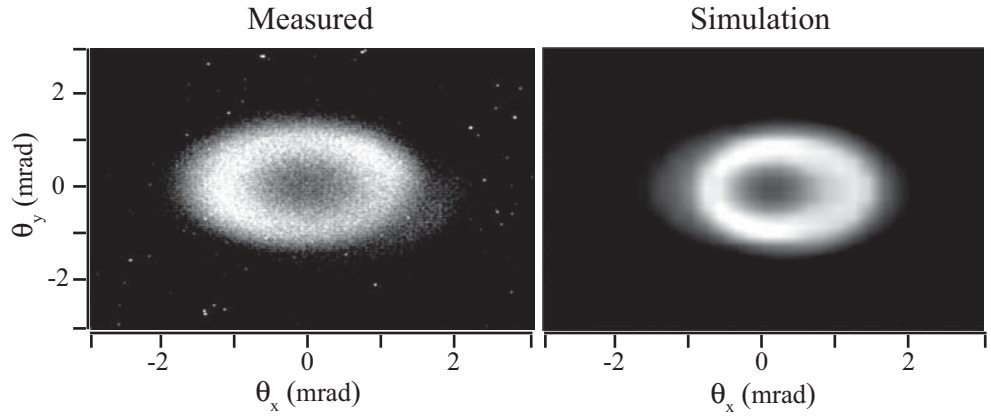

Figure 4.2: The far-field angular distribution of the radiation measured at the VISA I experiment (left) and generated from the computational model (right).

the VISA experiment. The confidence gained from the simulations allows reliance on the same modeling applications to analyze nearly all aspects of the present and future measurements in the VISA program.

Figure 4.1 shows the output of the aforementioned simulation suite. It represents the gain curve of the exponentially growing energy of the SASE FEL for the VISA I experiment. The solid line is the gain curve produced by `GENESIS` (with the dashed lines representing noise fluctuations); the dots represent the measured results of the energy at each profile monitor along the undulator, spaced 50 cm apart. Overall, there is very good agreement with theory, computations, and measurements. Figure 4.1 is also illustrative to demonstrate the three stages of SASE FEL radiation (spontaneous emission or lethargy, exponential gain, and energy saturation) that were discussed in Chapter 2.

The VISA I experiment also displayed hollow mode far-field angular distribution patterns, as seen in Figure 4.2. The hollow mode patterns were surprisingly well-reproduced by `GENESIS` simulations, indicating that they are a fundamental feature of the SASE FEL radiation.

An additional measurement during the VISA I runs was the experimental characterization of nonlinear harmonic generation [74]. The basic properties of harmonic radiation were confirmed, including the linear decrease of gain length and wavelength with respect to the harmonic number, n, as well as the narrowing of the spectral bandwidth.

The VISA experiment produced many results that confirmed many of the fundamentals of SASE FEL theory, and it has been well-acknowledged by the FEL community in publications and conference proceedings.

4.2 VISA IB: A Stepping Stone

The bunch compression scheme used in the VISA I experiment, obtained by exploiting second-order effects along the dispersive segment of the transport, facilitated high gain lasing. However, the strong compression restricted the management and manipulation of the electron beam properties prior to injection into the undulator. One of the main objectives for a successful VISA II experiment is to inject a chirped electron beam into the undulator. This is accomplished by preserving a linear electron beam chirp throughout the transport via the use of sextupole magnet correctors placed at high horizontal dispersion points. This method has been shown to mitigate the second-order effects, in particular by minimizing the T_{566} component of the second-order transport matrix [75]. The details regarding this experiment are discussed exhaustively in Chapter 5.

As a prelude to the implementation of transport linearization, a series of experiments performed prior to sextupole magnet installation have been conducted at the existing facilities of the ATF. These measurements employ a highly chirped, post-linac pulse, which through nonlinear longitudinal compression, achieves the

appropriate conditions that generate robust and sustained FEL amplification. This experiment was crowned with the lackluster moniker of "VISA IB", and will be referred to as such throughout this document (as well as other publications and conference proceedings).

Indeed, the transitional VISA IB experiment demonstrated unanticipated and previously unobserved phenomena. An extremely large relative bandwidth of the FEL radiation, up to 15% full width (FW, width as defined above the noise floor), at high gain is observed. The large spectral width is accompanied by an anomalously wide far-field angular radiation pattern, similar to the original VISA experiment, but more pronounced in angle. In this section, these experimental results are presented, as well as the simulations and in-depth analyses that reproduce the most striking aspects of the radiation measurements.

4.2.1 VISA IB: Experimental Layout and Operating Parameters

The experimental setup used in the VISA IB experiment is similar to that used in VISA I and detailed in Chapter 3. The photoinjector electron source, capable of producing a 70 MeV electron beam, is followed by a 20 degree dogleg transport line that delivers beam to the undulator. The dogleg contains an adjustable collimator, the high energy slits (HES), located at a high energy dispersion point. The electron beam size and transmitted fraction are measured at the HES and are used to determine the beam's energy and energy spread.

Alignment is a major concern at the ATF, as in any linear accelerator. To establish central alignment of the electron beam, rather than rely on retractable diagnostic scintillators which may not reproduce the same measurements after constant actuating, a different approach is employed at the ATF. The electron beam is aligned through the center of the quadrupole magnets of the transport

rather than the physical center of the vacuum pipe (although the beam pipe is aligned by rigorous surveying). This is accomplished by observing the electron beam on a screen downstream of a specific quadrupole. The quadrupole magnet strength, or equivalently the current through the coils, is varied by $\pm$ 10% and the respective electron beam centroid position is recorded. The steering magnet settings are slightly altered to center the beam, and the process is repeated. The goal of this approach is to minimize the deviation in electron beam centroid position by finding the optimal value of the steering magnet settings; the electron beam traversing through the center of the quadrupole ideally would receive zero transverse kick in trajectory (in practice, a minimal kick is observed). The procedure is repeated for each quadrupole triplet along the transport. This process establishes the center line of the transport, and the ideal trajectory of the electron beam centroid. The alignment technique is quite viable in the H-line, yet, it is more difficult to apply it in the dispersive line where other factors, such as beam jitter and dispersion, do not allow such stable and consistent measurements of the beam centroid. This procedure serves to de-couple the trajectory steering and focusing controls of the quadrupoles and steering magnets, which can be coupled by less rigorously controlled off-the-cuff operation, in which the central trajectory may be allowed to inadvertently drift from the design axis.

In VISA IB, the 500 pC electron beam generated at the cathode possesses a 2.8% energy spread at the end of the H-line, due to the time-energy chirp imparted at the linac. The linac modules accelerate the beam to an energy of 70 MeV. Approximately 330 pC, with 1.7% energy spread, propagates through the high energy slits along the dispersive line.

Once the bunch compression mechanism was discovered and confirmed, an online diagnostic was setup to fully understand and record the running conditions

during FEL operation. The compression process in the dogleg is monitored by measuring the *coherent transition radiation* (CTR) emitted from a retractable foil in Beamline 3 (Figure 3.5). The CTR energy is peaked when the beam's energy-time chirp is chosen to optimize the bunch compression. The CTR energy is measured with a Golay cell. The Golay cell is a thermo-pneumatic IR detector, operated at room temperature. IR pulses pass through an infrared-transparent window and heat the gas inside a chamber. The increase in temperature results in an increase of gas pressure which deflects a thin membrane which forms one side of the chamber walls. The deflection of the membrane is correlated to the amount of IR energy dissipated [76]. Measurements made at the CTR monitor, along with the energy and energy spread observed at the HES, allow the benchmarking of the results from the simulation suite to the experimental data.

4.2.2 VISA IB: Experimental Results and Observations

The electron beam is generated by shining the YAG laser, which has an energy of 15-18 mJ and a wavelength of 266 μm, on the copper cathode. The electron beam has a charge of 500 pC measured by a retractable Faraday cup located at the photoinjector exit. The subsequent chirping in the linac sections, by accelerating off rf-crest, is accomplished by shifting the phase between the two accelerating modules. The optical lattice employed along the H-line is designed to keep the electron beam size manageable throughout the transport. The beam energy is 70 MeV, approximately determined by the electrical current settings on the first dipole magnet, given by the practical formula, $E[\text{MeV}] \approx 1.8 \times I[\text{amps}]$, where the quantities are quoted in laboratory units. Another reliable benchmark of the central beam energy is derived from Eq. 1.5, as the spectrum of the FEL radiation, and thus the central radiated wavelength, is measured.

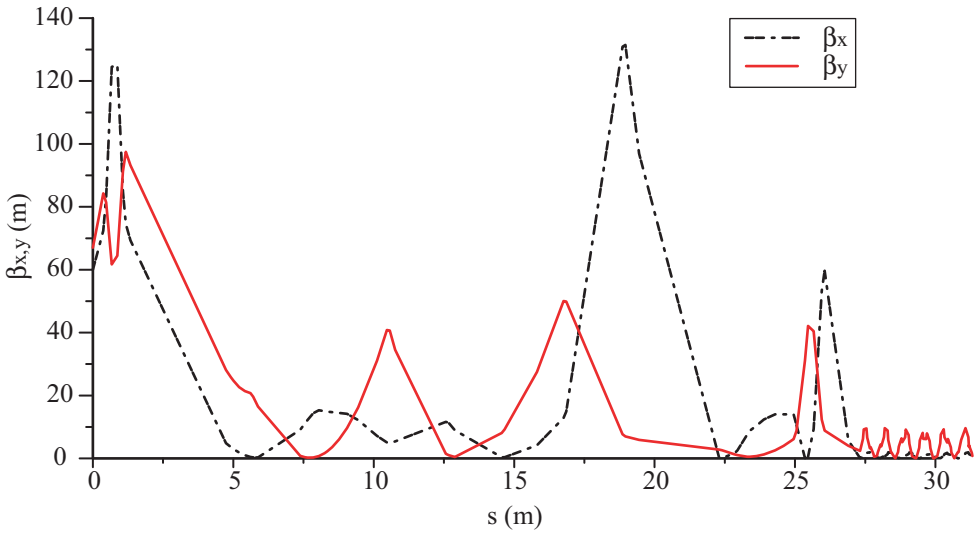

Figure 4.3: The Twiss parameters experimental fit for the VISA IB experiment.

The Twiss parameters are calculated with a MatchCad worksheet, authored by V. Yakimenko and maintained by the ATF staff, which numerically fits the parameters of beam size observed on several beam profile monitors. The emittance is obtained by using the multiple screen method [77]. The beam size in at least three different longitudinal positions along the transport can be used to measure the sigma matrix. At the ATF, measurements of beam size at six screens along the H-line (Figure 3.5) are used to calculate the sigma matrix and subsequently the normalized emittance. It is not unusual to observe recorded normalized emittance values as low as 1 mm-mrad at the ATF.

For a complete characterization of the electron beam properties, a Microsoft Excel worksheet was written by H.-D. Nuhn to calculate the Twiss parameters of the beam based on the observable beam sizes on the profile monitors. This online tool is crucial as it allows the operator to maintain a steady course during the experiment. Figure 4.3 shows the measured values of the Twiss parameters using the most acceptable fit parameters. These results are compared to simulations

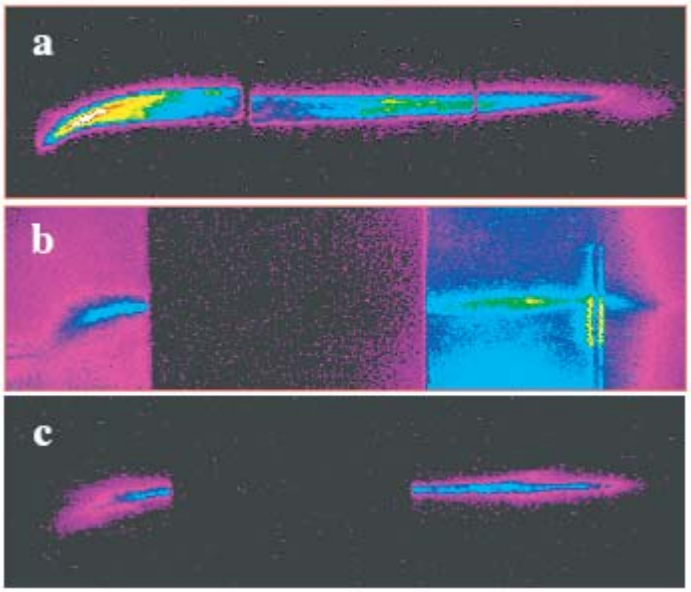

Figure 4.4: Images of the electron beam on the high energy slit (false color), with the high energy slits (a) fully closed, (b) fully open and (c) transmitting the compressed fraction of the beam.

(`ELEGANT`) in the following section (Figure 4.10).

The electron beam measurements along the F-line are anchored by the observation of the energy spread at the high energy slits (HES). Located 1.3 m from the first dipole, the HES, when fully closed, is used as a beam profile monitor to record beam size and centroid position. The momentum resolution at the HES is calculated from the pixel resolution of the CCD and frame grabber (46 μm per pixel in the horizontal, or bend, plane, and 50 μm in the vertical); the momentum resolution for the system at the VISA IB energy is approximately 0.4 MeV.

The electron beam at the HES has an observed energy spread of 2.8%. The fully opened HES allows approximately 30% transmission of the electron beam. The transmission of the beam charge is measured by a Faraday cup located at the end of the undulator. In prior VISA runs, full transmission was achievable, however due to the high energy spread of the VISA IB runs, only 330 pC is

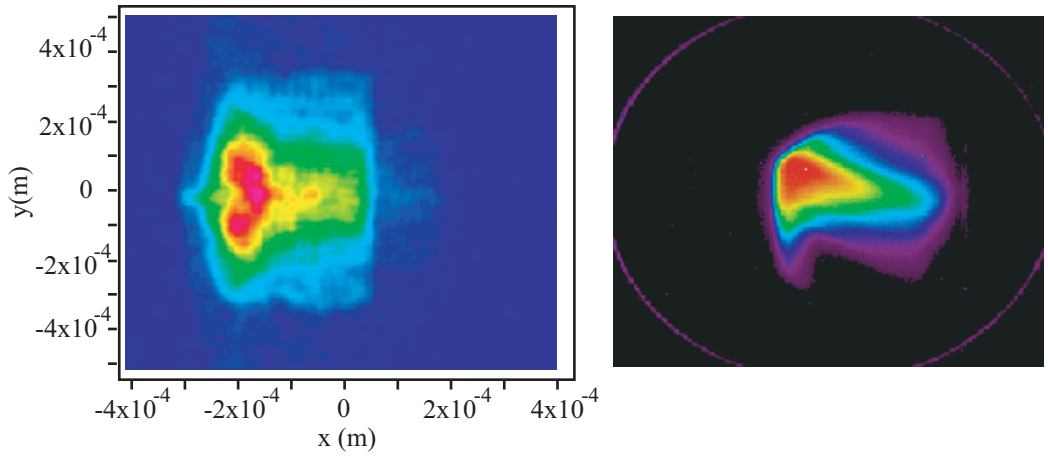

Figure 4.5: The transverse distribution of the beam at the location of the diagnostic produced in simulation (left) - `ELEGANT`, and raw image (false color) of the electron beam on the final pop-in before injection into the undulator (right), measuring 375 μm in x and 225 μm in y.

transported. The resultant energy spread of the beam after collimation at the HES is 1.7%. The remainder of the beam is clipped at the HES, and is observable on the phosphor coatings on either side of the slits during run time, as seen in Figure 4.4. This figure also demonstrates that the HES is an invaluable online diagnostic to monitor energy spread and compression.

Compression of the electron beam through the dogleg transport is directly observable by the Golay cell placed along Beamline 3 (BL3). The final matching triplet on BL3 is driven at high electric current as large magnetic gradients are required to focus the beam to a tight spot to match the beta functions at the undulator entrance. The measured beam radius on the final beam profile monitor of the transport (40 cm before the undulator) is 435 μm. Figure 4.5 shows an image of the transverse profile of the electron beam and a simulation of the beam for the given running conditions.

Steering is important throughout transport, as the central trajectory of the beam should be well known. In Beamline 3 and the VISA undulator, alignment

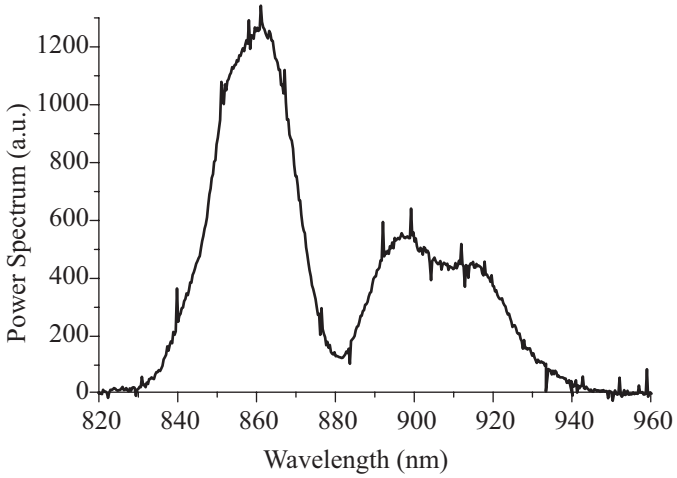

Figure 4.6: The anomalously wide wavelength spectrum of the FEL radiation for the VISA IB experiment.

of the beam is accomplished by centering the image of the transverse beam spot on the profile monitors to the center of the reference diode laser.

4.2.3 VISA IB: Observation of Large Spectral Bandwidth

With bunch compression, betatron matching, and trajectory centroid correction, the conditions for SASE FEL gain are excellent. The observed FEL radiation at high gain displays an extraordinary wavelength distribution, as shown in Figure 4.6. The spectrum is notable for its double peak structure, having a mean value of the relative full width (FW) bandwidth of 12%. The average measured SASE radiated energy is approximately 2 μJ. The saturation energy of the initial VISA runs was near 20 μJ, nearly an order of magnitude greater than the VISA IB runs. Simulations displayed below show that this difference may be attributed to the shorter beam component, with smaller charge, used in VISA IB. The dual spiked spectral structure indicates the presence of two distinct lasing modes.

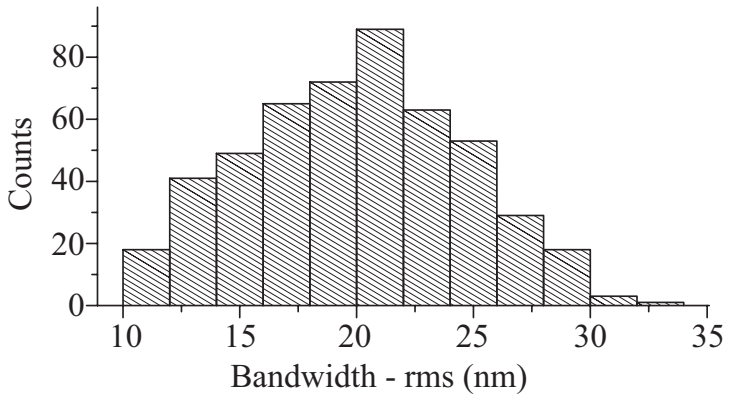

Figure 4.7: The statistical distribution of the rms bandwidth of the radiation collected during the VISA IB experimental runs.

The FEL output is much more stable than in earlier VISA runs, mainly due to the enhanced reproducibility of the electron beam pulse compression process. In fact, the lasing output was stable over a time scale of several hours, with only minimal user tuning required, an unusual feat for the VISA experiment. This allowed a wealth of spectral and energy data to be collected under nearly identical operating conditions.

The anomalous bandwidth of the wavelength spectrum is observed whenever high gain conditions are present. In Figure 4.7, the distribution of the spectral rms bandwidth is displayed for the radiation shots yielding only the top 10% of SASE energy (501 shots). The peak of the distribution is at 21 nm rms width, corresponding to 12% full width (2.3% rms). Shots as high as 33 nm rms width (15% FW, 3.6% rms) are observed in the data. For comparison, the earlier VISA runs in 2001 yielded a relative width of 2.4% (0.5% rms) with high gain lasing. The bandwidth data is summarized in Table 4.1.

	Bandwidth RMS (nm)	Bandwidth Relative	Bandwidth Relative RMS
VISA IB (mean)	21 nm	12 %	2.3 %
VISA IB (maximum)	33 nm	15 %	3.6 %
VISA I	4 nm	2.4 %	0.5 %

Table 4.1: The significant values of the bandwidth for the VISA IB runs, compared to earlier runs.

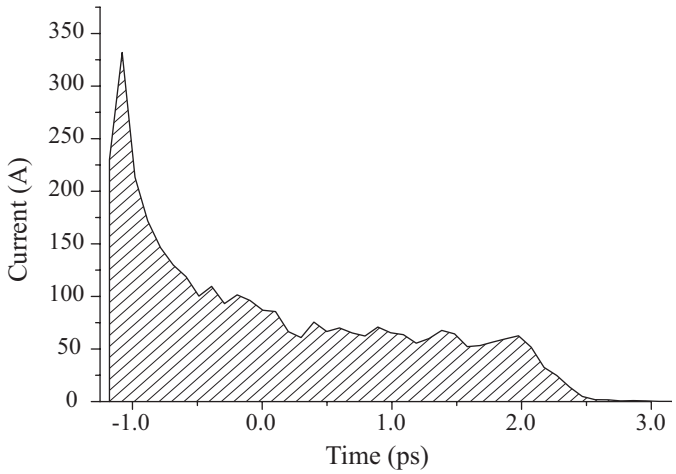

Figure 4.8: A simulation (`ELEGANT-GENESIS`) of the electron beam current profile for the VISA IB scenario. The lasing peak of the current exceeds 300 A.

4.2.4 VISA IB: Simulations and Analysis

Electron beam transport modeling using matrix calculations are accomplished with the code `ELEGANT`, as mentioned above. Although it is more commonly used for modeling scenarios dealing with circular accelerators, `ELEGANT`'s strength in calculating the second-order effects (parameterized in the elements T_{ijk} of the second-order transport matrix) leading to compression is the reason it has been used throughout the extent of the VISA program.

The modeling of the beam transport in VISA IB indicates that the peak cur-

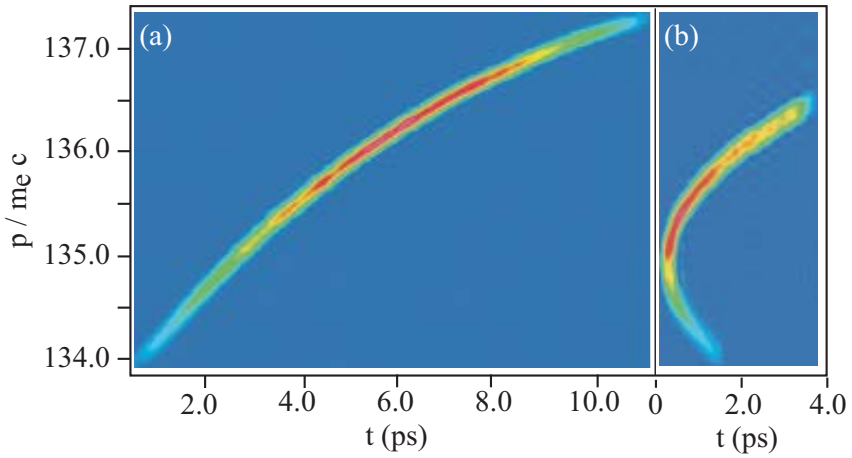

Figure 4.9: Longitudinal phase space of the electron beam for the VISA IB experiment, (a) just after the linac exit (`PARMELA` output - `ELEGANT` input), (b) prior to undulator injection (`ELEGANT` output - `GENESIS` input). Pulse compression from 10 ps to 4 ps is evident.

rent in the electron pulse, after nonlinear compression, exceeds 300 A (Figure 4.8). `GENESIS` simulations show that the lasing peak contains 25-30 pC of charge and is very short in duration with respect to the full electron bunch length. Unlike the original VISA running conditions, the compression process is insensitive to injection and phase fluctuations arising from either RF or photocathode laser timing jitter. This is mainly due to the energy spread in the initially chirped beam. Figure 4.9 shows the compression mechanism in effect. The 10 ps beam is compressed to approximately 4 ps, and collimated by the high energy slits. The large energy spread guarantees that a component of the beam is compressed regardless of phase jitter, as rf-laser injection timing errors are much smaller than the initial bunch length of 10 ps. After transport, the electron beam at undulator injection displays a highly nonlinear longitudinal phase space as a result of the second-order effects in the dispersive dogleg segment.

Other electron beam properties are also studied with `ELEGANT`. The beta functions of the beam are plotted in Figure 4.10 for the given running parameters of

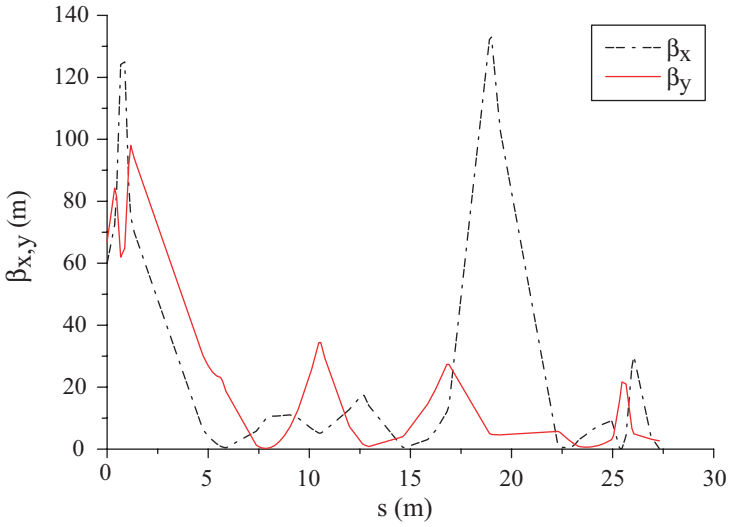

Figure 4.10: A simulation of VISA IB Twiss parameter evolution (ELEGANT)

VISA IB. There is good agreement with observed results for the beta functions (see Figure 4.3). Also of note is that the horizontal dispersion, or R_{16} of the transport matrix, is minimized to near zero in practical applications with the given operating tune. ELEGANT simulations show that the beta functions at the HES (a useful benchmark) are: $\beta_x = 5.2$ m, $\beta_y = 34.4$ m, while the dispersion, R_{16}, is -0.41 m^{-1}. The result is also confirmed by simulations in Figure 4.11. The beam profiles (x-t, y-t) after transport, prior to undulator injection are plotted in Figure 4.12. These graphics confirm that the electron beam is slightly mismatched in the horizontal direction and give useful illustrations to the type of beam that is being input into the undulator.

The GENESIS module of the simulation suite is used exclusively for FEL calculations and provides insight into the underpinnings of the unusual radiation amplification observed in the VISA runs. First and foremost, the FEL reaches the onset of saturation, consistent with the experimental comparison to previous VISA data (Figure 4.13). This lasing condition shows that the high current obtained via compression ensures high gain SASE FEL operation and outweighs

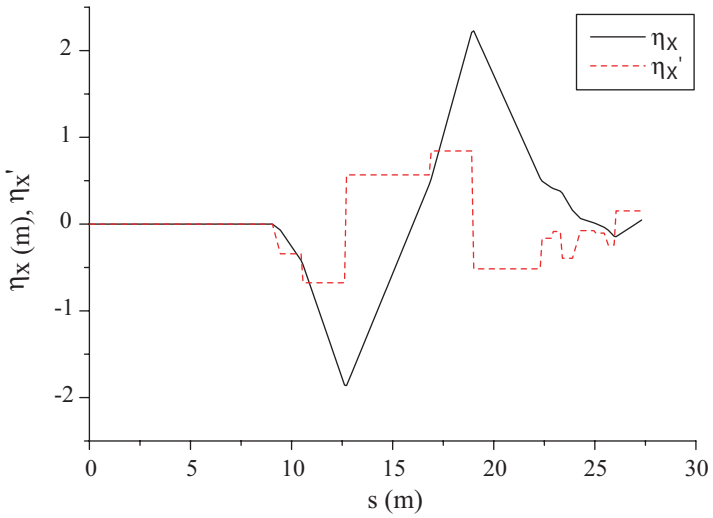

Figure 4.11: A simulation of the dispersion function (solid line), and its first derivative (dashed line), at VISA IB (`ELEGANT`).

any possible degradation of the slice emittance due to the large energy spread and residual dispersion.

Other key facets of the observed wavelength spectrum are reproduced by the simulations, such as the large bandwidth and double spiked structure, apparent in Figure 4.14. The `GENESIS` results show that the secondary spike observed in the spectra is due to the amplification of an off-axis, large angular spread mode. Further, simulations indicate that this mode is excited by the non-ideal beam centroid and envelope motion as the electrons perform betatron oscillations in the undulator's quadrupole focusing lattice.

While the electron beam as a whole is aligned to the undulator axis (to the limits of the profile monitor resolution), the lasing core centroid is misaligned, undergoing $\sim$300 μm oscillations. The lasing core rms envelope is also strongly mismatched to the focusing lattice, resulting in variations between 30 and 90 μm in x and 40 and 70 μm in y. As seen in Figure 4.15, there is a notable correlation between the oscillations in beam radius and the periodic growth of the spectral

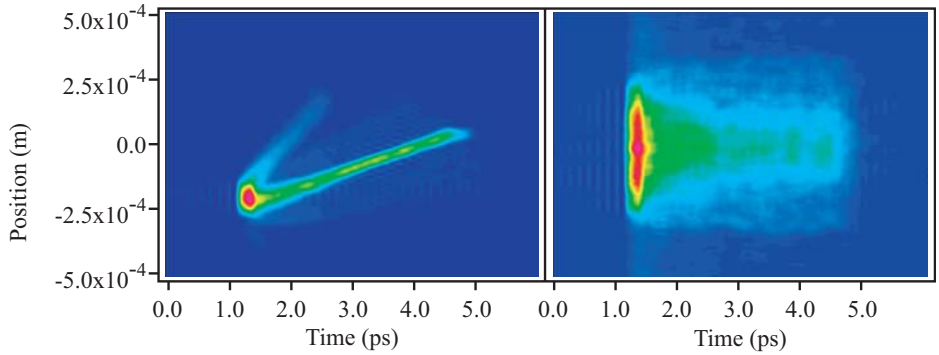

Figure 4.12: The simulated profile space for the electron beam at the end of the transport: (a) (x, t)-space, (b) (y, t)-space.

bandwidth.

To aid in the understanding of the effects that produce the observed spectra, we refer to the FEL resonance relation (Eq. 1.5) with the addition of the quadrupole focusing term, K_q,

$$\lambda_r = \frac{\lambda_u}{2\gamma^2}\left(1 + \frac{K^2 + K_q^2}{2} + \gamma^2\theta^2\right). \tag{4.1}$$

Here, the term K_q accounts for the effects on the resonance arising from the off-axis motion of the beam core, due to the quadrupole focusing of the undulator; all other terms have been defined before in Chapter 2. Energy spread has a negligible impact on the simulated spectral bandwidth for VISA IB operating parameters. Particularly in simulations, when `GENESIS` is run with all particles set to near equal energy ($\delta\gamma/\gamma \approx 0$), there is no notable change in the simulated FEL spectral bandwidth.

The red-shifting of the radiation arises mainly from the last two terms in Eq. 4.1. As discussed in Chapter 2, the first of these terms indicates the degradation of the longitudinal velocity due to the transverse motion of the electrons. In this experiment, there are two sources of transverse motion. The first component, $K = 2\pi e B_u/m_e\lambda_u c$, is called the undulator parameter (Chapter 2). For the

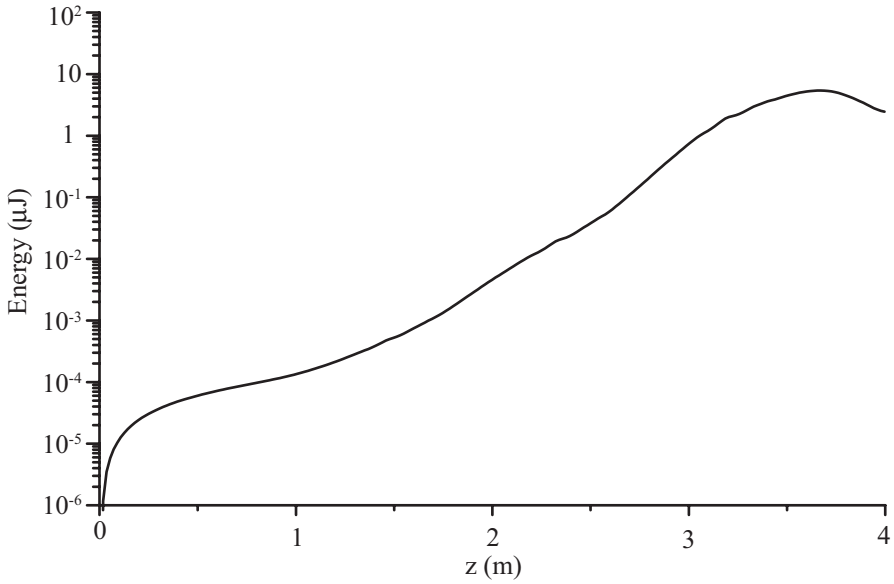

Figure 4.13: The simulated energy gain curve for the VISA IB experiment (`GENESIS` simulation).

VISA undulator, the peak magnetic field is $B_u = 0.72$ T yielding an undulator parameter of $K = 1.26$.

Due to the large excursions in the undulator focusing lattice, additional transverse motion causes a red-shift in the radiated wavelength. The bend in the electron trajectory due to the quadrupole fields, which have a square wave form, yields an effective undulator parameter of $K_q \simeq eB'\Delta x L_q/\sqrt{2}\pi m_e c$. Here, B' is the quadrupole gradient, Δx is the amplitude of oscillation, and L_q is the focusing period. For the VISA undulator parameters (Table 3.2), $K_q \approx 0.16$, which corresponds to a maximum trajectory angle of 1.2 mrad. The maximum predicted fractional red-shifting of the resonant wavelength due to this effect is 1.5% (corresponding to an rms spectral spread of 0.38% when averaged over a betatron period). Such broadening effects, due to changes in the electron longitudinal velocity, have been observed in a similar experimental context, that of Thomson-scattering sources [78, 79].

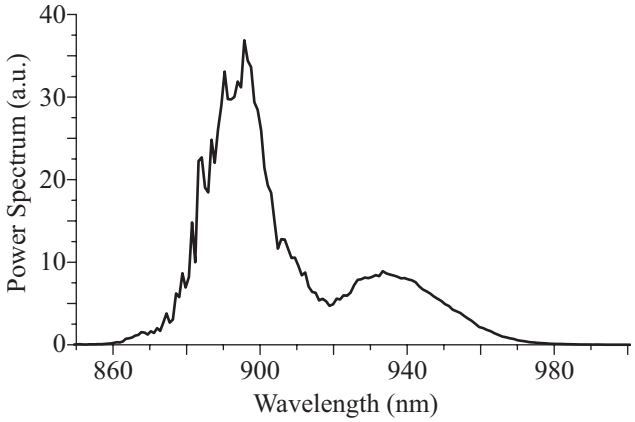

Figure 4.14: The simulated spectrum reproduced the features of the observed radiation (GENESIS).

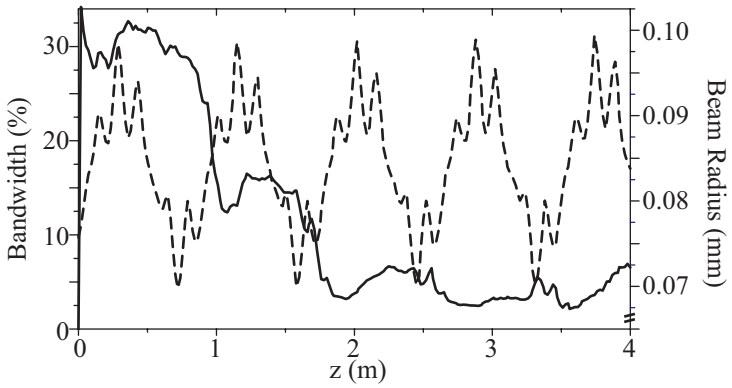

Figure 4.15: The correlation between bandwidth and beam size plays an important role in understanding the reasons for bandwidth broadening.

Large amplitude betatron motion and its associated horizontal angles contribute not only to this direct source of radiation red-shift, but also allow greater coupling to off-axis (higher spatial-order) horizontal emission modes. In turn, this off-axis emission provides the dominant source of radiation red-shifting, even greater than the effect due to angles in the electron trajectory. As in previous VISA results [18], the far-field angular spectrum is typically hollow, but has maximum intensity at much larger angles, in excess of 2 mrad. The red-shifting associated with horizontal angles is 4.2%, corresponding to the relative shift of

the long wavelength peak compared to the short wavelength (on-axis) peak (Figure 4.6). The relative shift in wavelength at an off-axis observation angle deduced from Eq. 4.1 is given by

$$\frac{\Delta\lambda}{\lambda_r} = \frac{\gamma^2\theta^2}{1+\frac{K^2}{2}}. \tag{4.2}$$

In `GENESIS` simulations, the quantity $(\theta^2)_{rms}$ has a value of 1.8×10^{-6} mrad^2, which corresponds to an rms wavelength spread of 2.0%. Accounting for all the other sources of spectral broadening discussed, the total rms wavelength spread expected under our experimental conditions is 2.2%, which is in excellent agreement with observations.

The production of the measured bandwidth's anomalous aspects through off-axis emission is correlated to oscillations in rms beam size. For example, a bi-Gaussian transverse distribution of radiating electrons with rms widths $\sigma_{x,c}$ and $\sigma_{y,c}$ may emit into coherent angles as large as

$$\theta_c = \frac{\lambda_r}{4\pi}\sqrt{\sigma_{x,c}^{-2} + \sigma_{y,c}^{-2}}. \tag{4.3}$$

For the beam sizes indicated in Figure 4.10, this prediction yields θ_c in the range of 1.7-2.5 mrad, consistent with the observed emission angles. However, Figure 4.15 also shows that when the transverse beam size is smallest, or the maximum coherent angle is largest, the bandwidth begins to rapidly decrease. This behavior is accompanied in simulations by a notable increase in the total FEL gain. The connection between the FEL gain and bandwidth variations is that the on-axis, short wavelength mode gain is enhanced by the increase in beam density when the transverse beam size is small, resulting in *gain guiding* [80]. The gain for the red-shifted mode, however, is not as strongly enhanced due to its wider angular emission, and the radiation bandwidth diminishes. As the FEL begins to saturate, gain guiding is no longer effective and the ratio of on-axis radiation to that of

higher-order modes is reduced. As the FEL enters a final, pronounced period of bandwidth growth, the final observed state of large spectral spread is observed.

4.3 Double Differential Spectrometer

Novel diagnostics were developed and implemented during the experimental run with the intent of further analyzing the anomalous results of the VISA IB experiment. One such diagnostic, the *double differential spectrometer* (DDS), was developed with the specific goal of unfolding the correlation between angles and frequency of the FEL spectrum. Some experimental run time was dedicated to the commissioning and implementation of this diagnostic. This section details the development and fabrication of the DDS diagnostic, including the hardware upgrade and calibration procedure. This is followed by a summary of the data retrieved from experimental runs dedicated to the commissioning of this tool. Indeed, initial data show the existence of several modes, and verify the overall parabolic shape of the radiation intensity in the angle-frequency (θ, ω) space. A brief analysis of this data, including `GENESIS` simulation work, is also presented.

4.3.1 Description of the Diagnostic

The anomalous spectral results from the VISA IB experiment did indeed display extraordinary results [81]. Further work is ongoing to obtain a more complete understanding of the physics of large angle coherent emission in a SASE FEL. In order to explore the angular emission effects in a high gain FEL, a radiation diagnostic (the double differential spectrometer) was developed to image the far-field intensity along a slit. The wavelength spectrum is dispersed in the direction normal to the slit by a set of gratings to produce a two dimensional intensity

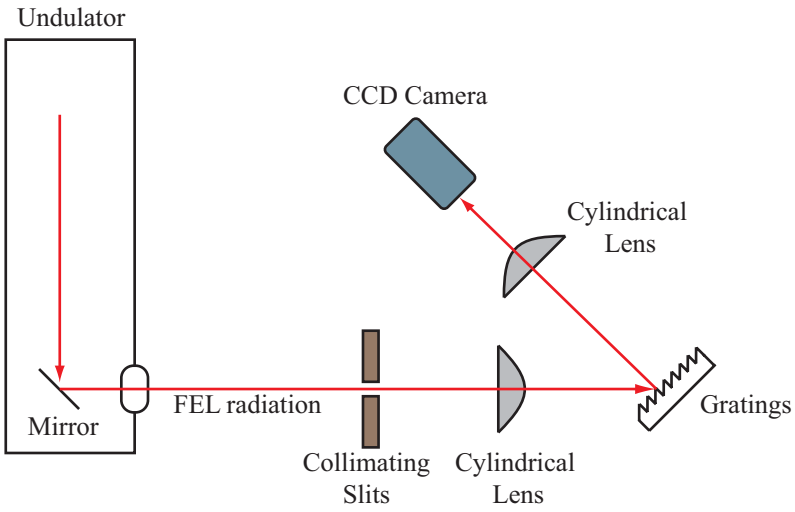

Figure 4.16: A schematic of the double differential spectrometer (not to scale).

distribution as a function of angle and frequency. It is important to note that the angle is actually only the transverse angle (vertical in this setup), so the actual expression that is measured is the frequency derivative of $dI/d\theta_y$, rather than the intensity as a function of the complete solid angle, $d\Omega$. A detailed analytical calculation of the intensity distribution is given in Appendix C.

The double differential spectrometer is calibrated with a pencil-style spectral Argon lamp (Oriel Instruments, Part No. 6030). The lamp emits a unique spectrum with lines and linewidths that are clearly defined, provided by the manufacturer. Figure 4.17 displays the output of the lamp collected with the DDS; for the purposes of such narrow linewidths, the DDS serves as a spectrometer. The Argon lamp was chosen because it emits lines in its spectrum which are similar to the wavelengths observed in VISA IB and expected in VISA II. Although the original lamp had shattered (due to a collaborator's misguided efforts), a second, identical calibration lamp was procured and is used to calibrate the detector prior to each experimental run. All subsequent calibrations incorporate a slotted metal sheath around the lamp to prevent accidental mishaps.

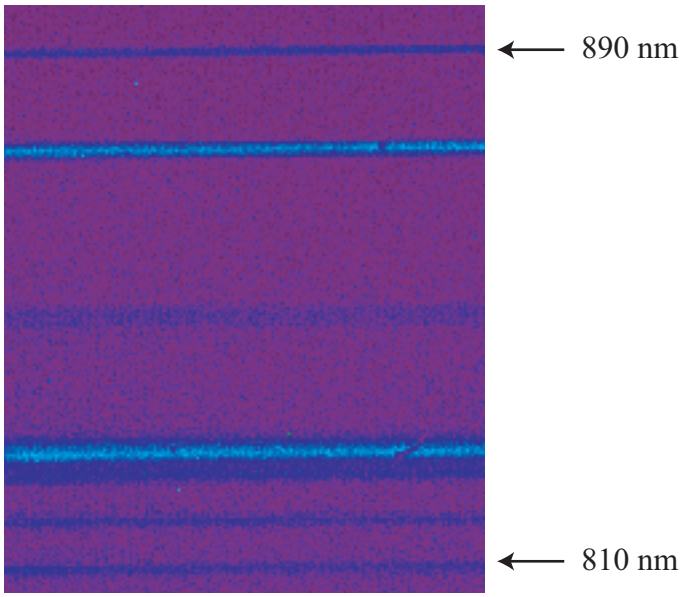

Figure 4.17: The calibration lines of the Argon lamp imaged through the double differential spectrometer.

4.3.2 Experimental Observations

The commissioning of the diagnostic took place after the initial VISA IB results. Although nearly identical running conditions were used, the observed FEL radiation had some minor differences when compared to VISA IB results. First, the gain was near saturation, just as in prior results, however, the anomalous wide spectral width was no longer observed. In fact, the goal of the secondary DDS runs was merely to test the diagnostic for operation purposes, an undertaking far less ambitious than achieving saturation. However, as a testament to the stability of the ATF photoinjector, and the understanding of the transport via start-to-end simulations, a high gain FEL was generated yielding noteworthy results.

A number of images were retrieved from the spectrometer, some shown in Figure 4.18. The approximate quadratic dependence of the frequency on angle

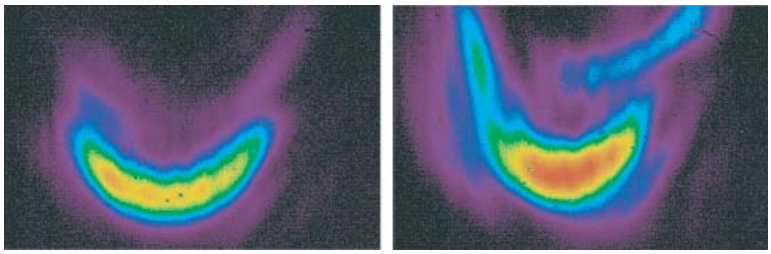

Figure 4.18: The false color images of the high gain FEL obtained from the double differential spectrometer display a quadratic dependence on angle (horizontal axis) as well as higher-order modes. Frequencies are shown along the vertical axis.

of the spectrum is prevalent in all the images. Some images display hollow structures as secondary shapes. Higher-order modes are also visible as wings in the distribution. This is consistent with results obtained during the VISA IB runs, where some wavelength spectra were observed to be narrow while others were wide and double peaked. Far-field angular distributions were recorded to further characterize the radiation. An observation screen with fiducials was placed approximately 3 m away from the end of the undulator. The FEL radiation was transported through air, without any optical elements, and observed on the screen with a CCD camera. Hollow shapes with definite spirality were observed (Figure 4.19). The spirality of the radiation patterns is currently under study because it is well known from general FEL theory that planar undulators produce horizontally polarized light.

A second diagnostic was designed to investigate the phenomenon of hollow far-field angular distributions. This diagnostic, termed the *mode converter*, was developed to further understand the far-field radiation, by manipulating and measuring the orbital angular momentum of light. The orbital angular momentum is an intrinsic property of light and has been observed and measured [82]. Further details regarding the mode converter are disseminated in Section 6.2

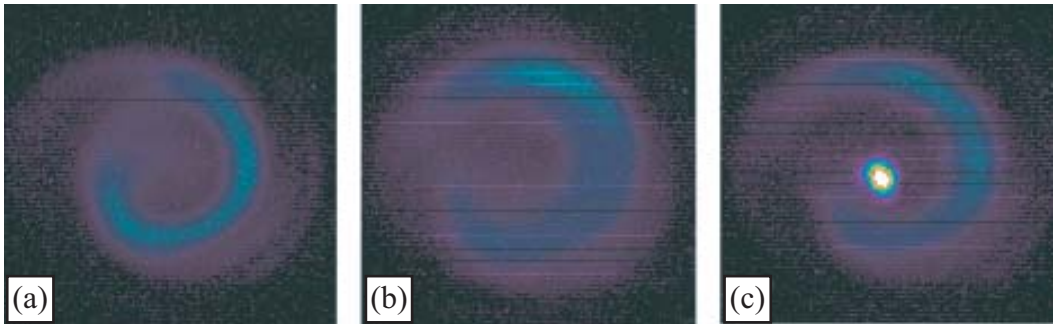

Figure 4.19: Angular distributions recorded during the DDS runs display hollow modes accompanied by spirality (a,b). The observed angular distribution is pictured with the reference diode laser (c).

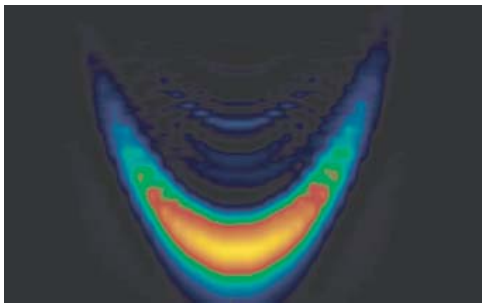

Figure 4.20: The intensity distribution under VISA IB operating parameters produced with the `GENESIS` post-processor toolkit.

4.3.3 Simulations

As is customary for anomalistic results obtained at the VISA program, start-to-end simulations were consulted. `GENESIS` analysis of the VISA IB data was able to reproduce the DDS images for idealized cases. The image in Figure 4.20 was produced by superimposing slices of the FEL radiation distribution selected through a vertical aperture (reasonably mimicking the experimental setup). The spectral angular intensity distribution displays the parabolic shape (quadratic dependence on angle) that is expected from any undulator radiation scenario, however careful inspection reveals the presence of higher-order modes, due to the SASE FEL process, as well. Although, the simulated distribution was generated

with idealized parameters of the VISA IB experiment, it illustrates that indeed, the start-to-end suite is a robust mechanism that is able to calculate nearly all aspects of the radiation using different experimental diagnostics for benchmarking. Analytic calculations for the intensity distribution are presented in Appendix C.

CHAPTER 5

Design of the VISA II Experiment

The VISA II project was proposed in 2001 as an extension to the successful VISA experiments at the Accelerator Test Facility in Brookhaven National Laboratory. This chapter divulges the specifics of the design and commissioning of the VISA II experiment. The conception of, and motivation for, the experiment is introduced in Section 5.1. The commissioning of the experiment, with a focus on the necessary engineering and hardware upgrade is described in Section 5.2. This is followed by detailed studies and simulations of the FEL radiation under VISA II operating conditions, with an emphasis on expected experimental results from the measurements. An explanation of the advanced diagnostics used for the experiment concludes this chapter.

5.1 VISA II: Introduction

The VISA II experiment was proposed in 2001 to continue the efforts of the VISA program at the ATF in BNL. The original goals of the project were split into two distinct parts. The first effort was the fabrication and employment of a dedicated chicane compressor upstream of the undulator, to create a high current electron beam via magnetic electron bunch compression [83]. Simulations have shown that the bunch compression achieved with this chicane would yield an increase of the electron beam current to 1.5 kA, reducing the FEL gain length so that

saturation is reached within the third meter of the four meter long undulator. Among other electron beam dedicated measurements, the chicane compressor would allow for deep saturation studies in a single pass high gain FEL [84], a topic of growing interest to the x-ray FEL community. The second part of the project, was the injection of a linearly chirped electron beam into the undulator to produce frequency chirped FEL radiation [85]. This would be accomplished by the deliberate control of second-order longitudinal compression in the dogleg of the ATF transport by the addition of sextupole magnet correctors at high horizontal dispersion points (η_x). Sextupole magnets have been widely used in ciruclar machines for the correction of chromatic aberrations in such systems [86]. In the dogleg transport, the main goal of the sextupole correctors would be to mitigate the T_{566} element of the second-order transport matrix [75]. Figure 5.1 shows a sextupole magnet that was designed and fabricated by PBPL and installed along the ATF transport specifically for the VISA II experiment.

Under ideal laboratory conditions, with the implementation of the chicane compressor and the sextupole magnets, an operator at the ATF would have independent control over bunch length compression, or beam current, and electron beam chirp respectively. The chicane compressor, which was initially slated as a distinct physics project, would evolve into a utility that enhances the capabilities of the ATF. With the chicane compressor, studies dealing with *coherent edge radiation* (CER) [87], *coherent synchroton radiation* (CSR) [88], transverse phase space tomography [89] and interferometric studies of bunch length measurements [90] have either been proposed or have been undertaken. The VISA II experiment nominally moved on to encompass only the addition and use of sextupole magnets to deliver a linearly chirped beam to the undulator and the ensuing diagnostics required to measure frequency chirped output radiation. Simulations show, that although saturation can not be achieved without a compressed beam, high gain is

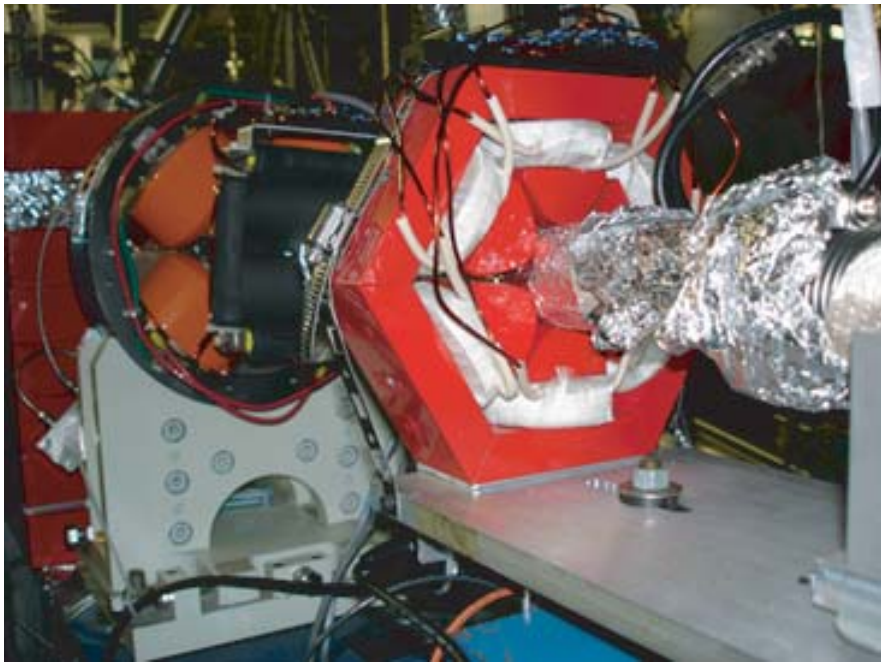

Figure 5.1: A photograph of a sextupole magnet (center) installed along the dispersive segment of the ATF transport

still achievable with the linearly chirped beam. The advanced diagnostics, for the VISA II experiment include the double differential spectrometer (Section 4.3) to deconvolve the correlations between angles and frequencies in the radiation, and a modified version of *frequency resolved optical gating* (FROG), which is crucial to measure the properties of the frequency chirped pulses created by the operation of the VISA II FEL.

5.2 Motivation for Chirped Beam Operation

As mentioned in Chapter 1, there are current proposals to construct single-pass high gain SASE FELs to generate Ångstrom wavelength radiation in the x-ray regime. These sources are designed to operate at hundred femtosecond pulse lengths [91], with a clear demand to achieve shorter time scales. A number of

Sextupole Parameter	Symbol	Value
Gradient	k_2	22.0 T/m^2
Length	l_s	5 cm
Max current	I_{max}	8 A

Table 5.1: The specifications of the sextupoles fabricated for the VISA II experiment.

experiments have been proposed to shorten the duration of the high power x-ray pulses. For example, it is possible to correlate the frequency with the longitudinal position of a spike by injecting a chirped electron beam through the undulator [92]. This chirped radiation could then be compressed by gratings to shorten the pulse length, and thus increase the peak power.

Another such scheme to obtain ultra-short pulse lengths, serves as the afflatus for the VISA II experiment. The experiment was derived from a proposal for an experiment at the LCLS [43]. The proposal describes a two-stage SASE FEL process (Figure 5.2). In the first stage of the scenario, an energy-chirped electron beam is injected into an undulator. The energy chirp is parametrized by the dimensionless factor α,

$$\frac{\delta\gamma}{\gamma} = \alpha\frac{l}{l_b}, \tag{5.1}$$

where $\delta\gamma/\gamma$ is the energy spread of the electron beam, l is the longitudinal coordinate, and l_b is the bunch length of the pulse. Using the FEL resonance condition (Eq. 1.5), we see that the output radiation will have a frequency chirp equal to twice that of the electron beam chirp,

$$\frac{\delta\omega}{\omega} = 2\alpha\frac{l}{l_b}, \tag{5.2}$$

where $\delta\omega/\omega$ is the frequency bandwidth of the radiation. The growth of the radiation due to the collective instability would require revisiting Maxwell's equations

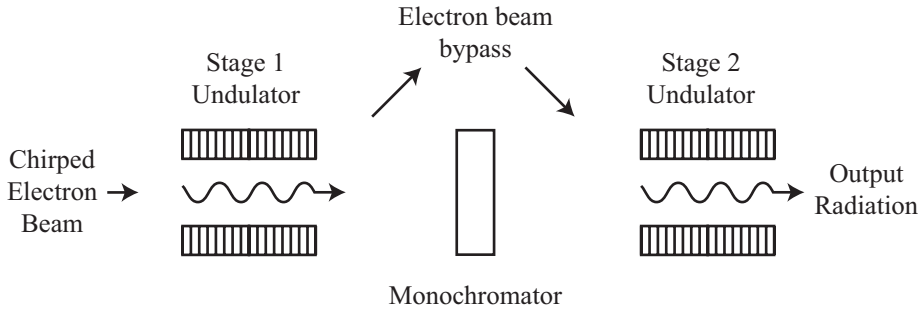

Figure 5.2: A schematic of the chirped beam two-stage SASE FEL proposed for the LCLS to obtain ultra-short x-ray pulses.

with the addition of a first-order correction term describing the chirp. The increase in the gain length will be small if the chirp over one cooperation length (the slippage occurring over a gain length) is small. Intuitively, the correlation is preserved; if the chirp would be large enough, degradation of the gain due to energy smearing would occur.

The first stage undulator produces a frequency chirped output radiation through the SASE FEL process. This radiation is then monochromatized, and thus shortened to a desired pulse length, while the electron beam is sent through a bypass (e.g. chicane). The shortened radiation pulse is then injected into the second stage undulator, where it serves as a seeding pulse. Only a short section of the electron beam is resonant with the frequency chirped seed pulse. The second undulator is utilized as a FEL amplifier and the short pulse is subsequently amplified to saturation. The transverse and longitudinal coherence of the output pulse from the first undulator are preserved through the second amplifier. Figure 5.2 illustrates this concept to create short duration x-ray pulses, which is feasible with the beam parameters available at the LCLS. In order to test particular aspects of this scheme, the VISA II experiment has been designed to operate with the highest energy chirp allowable at the ATF.

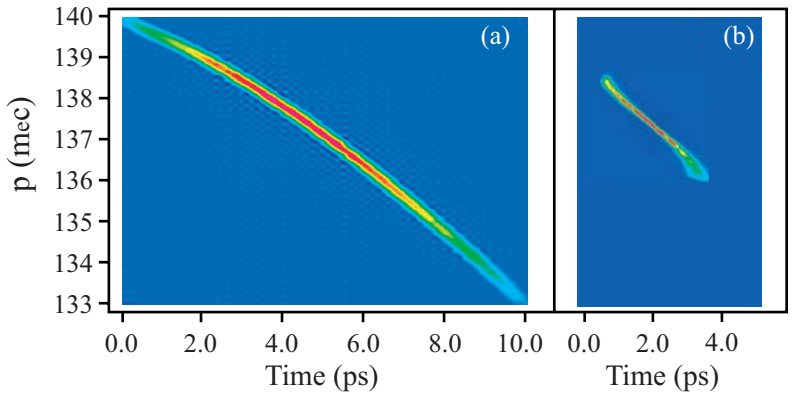

Figure 5.3: The longitudinal phase space of the electron beam under VISA II runing conditions, after the linac (a) and prior to undulator injection (b).

The main goal of the VISA II experiment is to produce and measure the strongly chirped SASE FEL radiation produced from the energy chirped electron beam. The existing technologies for sextupole magnet fabrication are sufficient for the needs of the chirp preservation through electron beam transport. After extensive simulation work, sextupoles were designed and fabricated at UCLA to meet the requested specifications, summarized in Table 5.1. However, the diagnostics required to measure the ultra short frequency chirped pulses are not in the realm of present-day commercially available detectors. A modified FROG device was designed specifically for the large bandwidths observed at the VISA IB program and implemented for the VISA II program as well.

5.3 VISA II: Start-to-End Simulations and Analysis

The process for designing a chirped beam FEL system began with analytic calculations accompanied by extensive work in simulations. Since the simulation suite was powerful in predicting observed phenomena for both the VISA and VISA IB experiments, there is confidence in the reliance on the same suite to design the

VISA II experiment. In fact, all issues regarding electron beam transport, compression, and FEL studies were carried out in detail prior to operations, whereas in previous projects, the start-to-end simulation suite was used as an analysis tool after the experimental data was collected.

The first step in the simulation process was to run the electron beam on the back of the accelerating field crest (so-called "back of crest" operation), as opposed to forward of crest as in the VISA IB scenario. Using `PARMELA`, the appropriate gun and linac conditions were chosen to optimize the linear chirp exiting the linac modules. The longitudinal phase space of the beam is nearly linear and has a normalized mean energy of γ_0=136 (Figure 5.3 (a)). The preservation of this chirp throughout the transport is vital for the operation of VISA II. This poses a challenge because of the second-order longitudinal compression that exists in the dogleg of the transport. Although, the compression mechanism yields a high current required for FEL saturation, it alters the linearity of the longitudinal phase space. The two sextupole magnets are placed as close as possible, given pre-existing obstructions along the beamline, to the peak horizontal dispersion points. The sextupole magnets had worked so effectively (Figure 5.4) that the ATF requested the PBPL to fabricate and install additional sextupole magnets along the beamline for other experiments requiring corrections to chromatic aberrations.

The addition of sextupole magnet correctors, nearest the high horizontal dispersion points, indeed mitigates this effect, and preserves the chirp through the transport. Figure 5.3(b) shows that the linear chirp is preserved prior to undulator injection. Clipping at the high energy slits (HES) is also observed in the simulations, which is advantageous for this scenario, as it provides a purer linearly chirped beam (less second- or third-order distortion due to rf curvature)

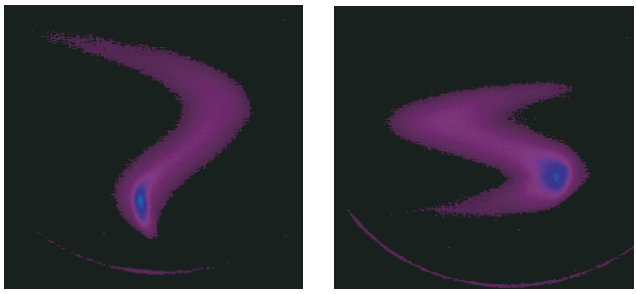

Figure 5.4: Transverse profile images (false color) of the electron beam near the end of the dispersive line. The sextupole magnets are energized to exaggerated settings from the design tune to demonstrate functionality and second-order effects.

to study the SASE FEL effects with. The transmission across the HES is about 54% according to `ELEGANT` simulations. The propagated current is more than sufficient for FEL operations.

To control the compression along the transport, the T_{566} element of the second-order transport matrix is tracked through the simulations. Once the second-order longitudinal compression factor is minimized, by running the sextupole magnet correctors at the appropriate currents, the compression is mitigated and the linear chirp is preserved.

In practical terms, however, it is not possible to measure the T_{566} term with the currently available diagnostics at the ATF. Rather, in practice, the T_{166} transverse term can be measured directly. To explain this measurement properly, we first revisit some fundamentals from accelerator physics. From beam physics [39], we can express the the state vector of the electron beam by $\vec{X} = (x, x', y, y', z, \delta)$ and its evolution from initial to final state ($\vec{X_1} \rightarrow \vec{X_2}$) is given by transport matrices such as,

$$(\vec{X_2})_i = R_{ij}(\vec{X_1})_j + T_{ijk}(\vec{X_1})_j(\vec{X_1})_k. \tag{5.3}$$

The R_{ij} and T_{ijk} terms in Eq. 5.3 are the first- and second-order transport matri-

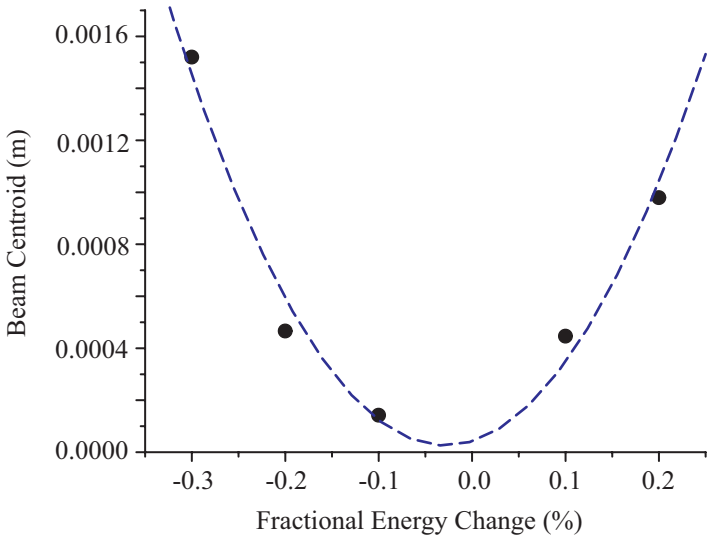

Figure 5.5: Preliminary experimental data of the second-order horizontal dispersion. The solid points are measured data and the dashed curve is the quadratic fit.

ces, respectively. Since, the T_{566} element, is a longitudinal term and can not be directly observed, the transverse terms will be measured. Writing an expression from Eq. 5.3 for the horizontal position of the electron beam yields

$$\Delta x_{cen} = R_{16}\delta + T_{166}\delta^2. \tag{5.4}$$

The R_{16} term is proportional to the fractional change in energy, or equivalently the negative fractional change in total magnetic field. Diagnostics available at the ATF allow the measurement of centroid position versus fractional change in magnetic fields. This data can be plotted and fit to a quadratic (Eq. 5.4), and the T_{166} term can be deduced. In practice, if this term evolves the same way as it does in simulation, then we can confidently proclaim knowledge of the evolution of the T_{566} term. Figure 5.5 displays data from this experimental method measured at the fourth beam profile monitor on the dispersive line; the fit values for the horizontal dispersion displayed in this figure are $R_{16} = 0.01$ m and $T_{166} = 1.94$ m.

The second important step of the design process was to ensure that the chirped

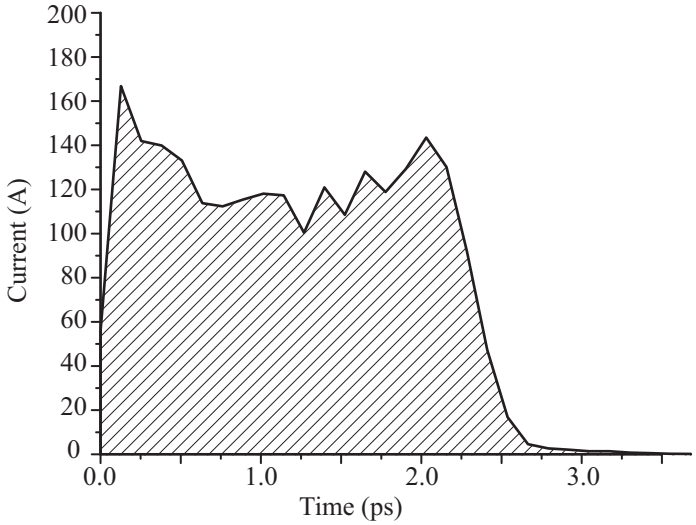

Figure 5.6: The current profile for VISA II running conditions displays a moderate gain in current.

beam was capable of lasing in the undulator. As it turned out, the operations with sextupole magnets energized at the appropriate settings, did not compress the beam or yield a great enough current for saturation. This is a problem for the diagnostics, some of which require more photons to be operational than the gain in the SASE FEL would produce. After numerous iterations, the tune (or magnet settings) of the beamline was optimized so that the chirp was preserved with a small amount of compression, yielding a mild increase of the average beam current up to 120 A. The electron beam is run back of crest, yielding negative R_{56} partial compression in the dogleg [75]; on the other hand, the chicane produces positive R_{56} longitudinal compression. Figure 5.6 illustrates the slight compression and the resultant increase in the current.

The modest increase in beam current (factor of 2) is enough to achieve SASE FEL lasing with a gain on the order of 10^6 (Figure 5.7), according to the `GENESIS` output. This level of gain is adequate for detection with the existing diagnostics and requires few additional changes for a complete characterization of the

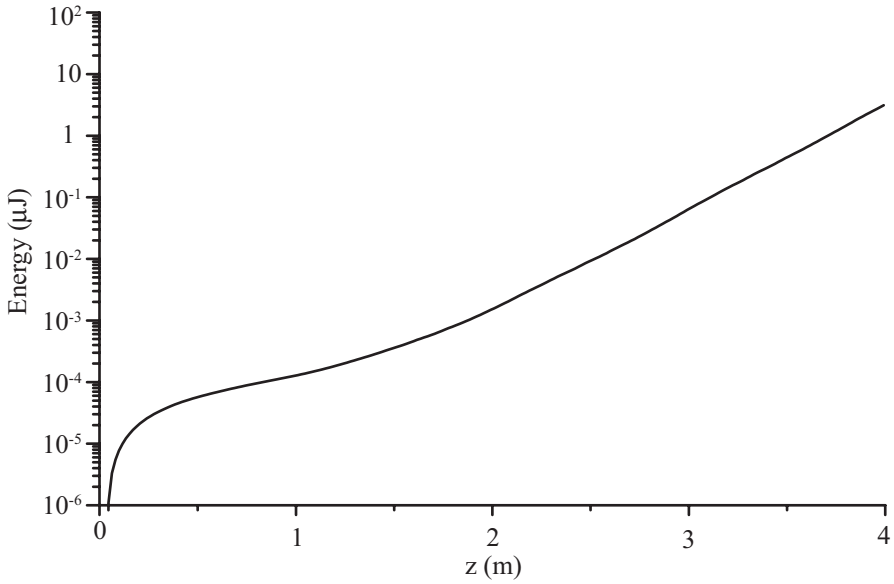

Figure 5.7: The predicted gain curve for VISA II operating parameters. Although saturation is not reached, a gain on the order of 10^6 is expected.

radiation.

The GENESIS code was used for all the FEL simulation work. One interesting result from GENESIS was that the expected wavelength spectrum was very wide. This is due to two main effects. First, the chirped beam produces a bandwidth in the FEL radiation that is proportional to the energy spread of the input electron beam, as noted above. Second, and perhaps more dominant, the FEL has not achieved saturation under these conditions. The expected bandwidth, however, is still not as wide as the VISA IB case, as off-axis lasing should be avoided with the correct VISA II tunes.. The center wavelength of the spectrum is located at 868 nm and the relative bandwidth is just under 4% (Figure 5.8). The spectrum as predicted by the GENESIS module of the simulation suite, is at the edge of the resolution provided by a commercially available FROG unit [93]; the measured spectrum for the VISA IB experiment is well beyond the available resolution. Therefore, a modified version of FROG will be used to characterize the frequency

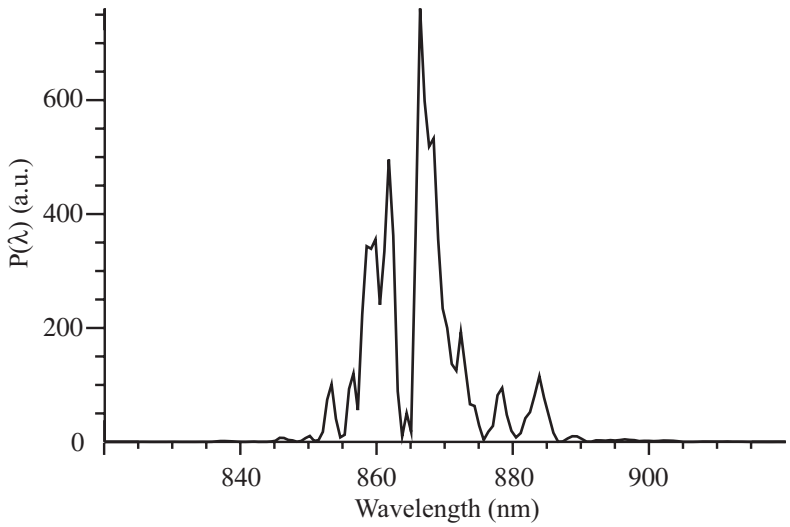

Figure 5.8: The simulated wavelength spectrum for the VISA II experiment displays a wide bandwidth because saturation has not been achieved.

chirped FEL pulse; this is discussed in Section 5.4.

5.4 Advanced Diagnostics: FROG

The creation of the chirped pulses at the VISA II experiment is not complete until the pulses are actually measured. In order to completely characterize the pulse, a measurement of the radiation's amplitude and phase is required. The ideal candidate for such a measurement is the frequency resolved optical gating (FROG) technique [94]. FROG measurements have already been successfully conducted for SASE FELs at Argonne National Laboratory [95], and have been proposed for measurements elsewhere [96].

In the most basic terms, the FROG technique is an autocorrelation type of measurement which measures the spectrum as a function of the delay. The output of the FROG device is the *spectrogram* (intensity in the time-frequency hybrid domain) [94]. Using an iterative algorithm and two-dimensional phase

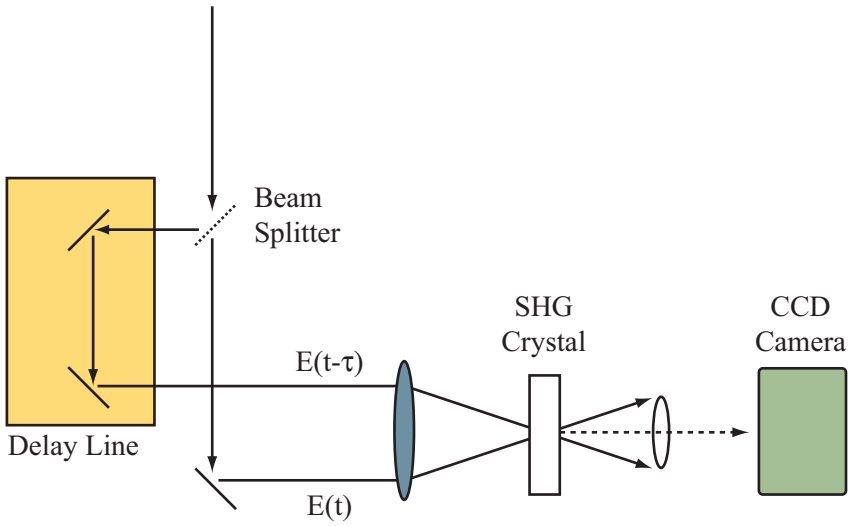

Figure 5.9: A schematic of a typical SHG FROG setup.

retrieval image recovery techniques, the FROG yields full amplitude and phase information for a given pulse. The most common type of FROG is the second harmonic generation (SHG), illustrated in Figure 5.9; Grenouille is a type of SHG FROG [97]. The SHG FROG is the most sensitive FROG and its output trace is given by

$$I_{SHG}(\omega,\tau) = \left| \int E(t)E(t-\tau)e^{-i\omega t}dt \right|^2 . \tag{5.5}$$

The Grenouille is a self-aligning FROG system which has no dynamic parts and possesses the ability to resolve pulses as short as 10 fs [98]. However, after careful studies [99], it was deemed that although a commercially available Grenouille unit had a resolution which was bordering the expected measurable parameters for the VISA II experiment, it would definitely not meet the measured parameters of the VISA IB experiment, and is thus not the ideal candidate for the VISA FEL which has the ability to operate in both regimes. The measured bandwidth of the VISA IB experiment was simply too large to allow for any reasonable resolution. It was decided to continue the course with a modified version of the hardware that would satisfy most of the needs of the VISA experiments.

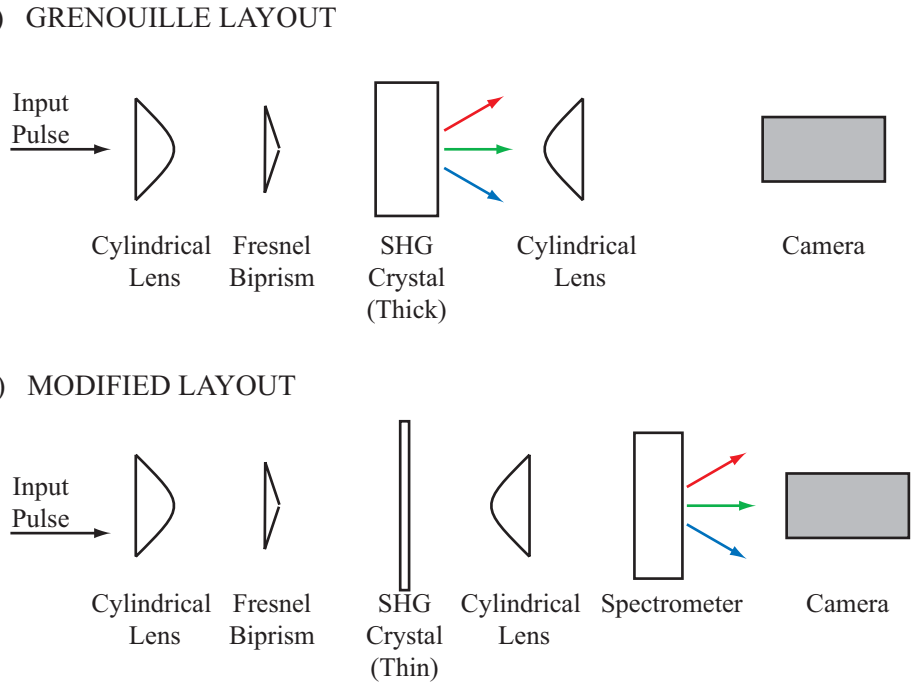

Figure 5.10: The original Grenouille layout (a) and the proposed modified version (b) for the VISA II experiment.

5.4.1 FROG Modifications at VISA II

The SHG FROG setup (Figure 5.9) consists of a beam-splitter to divide the pulse, a lens for focusing, a second harmonic generation crystal, and a camera to serve as a spectrometer. The camera displays a spectrogram, which is an intensity distribution plotted against frequency on one axis and time-delay on the other. The beam splitter sends half of the pulse to the delay line, which introduces the necessary time-delay for an autocorrelation at the crystal. The SHG crystal is very thin; the bandwidth for a SHG crystal is inversely proportional to its thickness. The Grenouille system, which is a commercial SHG FROG system, consists of a similar setup in a footprint less than 12 inches in the longest dimension. It differs from the traditional FROG in the layout; instead of a beam splitter and a thin SHG crystal, the Grenouille uses a Fresnel bi-prism and a thick crystal, with

additional cylindrical lenses for focusing. The physics underlying the Grenouille is nearly identical to the SHG FROG, only the components are different. This allows simple user operation of the device as all the pieces are already self-aligned.

The VISA II collaboration was extremely interested in employing such a device due to the spatial restrictions in the Experimental Hall at the ATF. However, the commercially viable solution would not meet the needs required for the experiment. The resolution of a commercial Grenouille unit degrades quickly as the bandwidth of the measured pulse increases. In fact, for the VISA IB case, the bandwidth of the FEL pulse to be measured was greater than 100 nm, which corresponds to a spectral resolution of 60 nm. This was obviously not acceptable from the experimental point of view. However, a modification of the system [93, 99] would improve the resolution, while maintaining the ability to measure both intensity and phase.

Figure 5.10 shows the proposed modification in schematic form. In the original layout of the Grenouille, the Fresnel biprism had the role of splitting the beam, adding a delay, and recombining, while the thick SHG crystal served for autocorrelation and as a spectrometer. The thick SHG crystal limits the resolution for the wide bandwidth pulse; it would be replaced with a thin crystal and a separate dedicated grating-based spectrometer. This slight alteration (although it loses the moniker of Grenouille) has been referred to as *modified FROG* for the VISA II experiment.

As usual, simulations were carried out to test the feasibility of the modified FROG at the VISA II experiment. Figure 5.11 shows the output of a `GENESIS` post-processing tool that allows for the calculation of the SHG spectrogram. This spectrogram was input into the Femtosoft Technologies FROG software and the actual temporal profile of the FEL pulse was reconstructed. The spectrogram

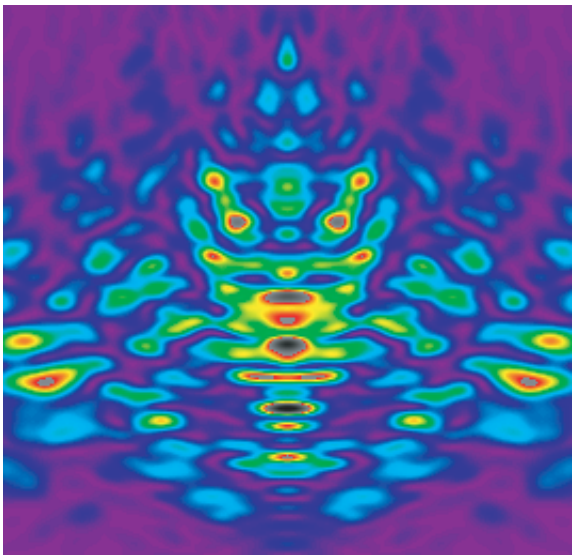

Figure 5.11: The spectrogram for the frequency chirped pulse at VISA II expected from the modified SHG FROG diagnostic. In the spectrogram, frequencies lie along the vertical axis and the time-delay along the horizontal.

is symmetric, as is the case for all SHG reconstructions, so it has an ambiguity about the direction of time. This is a trivial ambiguity, since there is evidence of a chirped pulse a priori, as well as confirmations from simulations, we can assume that the pulse is positively chirped for all reconstructions.

CHAPTER 6

Conclusions

This chapter will examine the near future of the VISA program and its collaboration with the ATF. In Section 6.1, the Seeded Amplifier experiment is presented, along with experimental concerns and simulation studies that were carried out to explore the physics of the seeded FEL system. The following section posits on three possible experiments that have not yet been formally addressed but are very viable with minimal change to the existing system. Each of these proposals has merit either as a proof-of-principle experiment or as a precursor to a full-fledged experimental undertaking. Finally, the dissertation will conclude with a brief summary and an outlook to future applications that the VISA program may influence.

6.1 Design of the Seeded Amplifier Experiment

The current project at the ATF under the auspices of the VISA program is the design of a seeded amplifier. The motivation for this measurement is to demonstrate control of the divergence of the FEL radiation. The seeded amplifier is proposed to measure the far-field angular distribution of the radiation and study the effects of seeding an undulator with a coherent laser source. The seeding source will establish transverse coherence in the amplified radiation, including a lower bandwidth, thus a higher brightness. In the far-field, this radiation may

be manipulated, similar to that in the VISA IB experiment. The increase in divergence angle will directly decrease the intensity thereby allowing delivery of high power radiation within the damage threshold of sensitive optics.

This experiment requires some nontrivial modifications to the existing line. The seed laser pulse for this experiment is picked off from the YAG laser that the ATF employs for photoelectron generation. The wavelength of the laser is 1064 μm. The energy of the electron beam must be lowered accordingly ($\approx$61 MeV) to reproduce a resonant wavelength of 1064 μm and ensure field amplification. The electron beam transport remains the same as described in Chapter 3, except obviously the magnet settings for the dipoles and quadrupoles must be shifted to account for the new operating energy. The diagnostics, which were used for 800 nm wavelength radiation, must also be upgraded for the new operating wavelength. Specifically, a new spectrometer was purchased (Ocean Optics USB2000-IR) to cover the longer wavelength regime. A more sensitive camera (UNIQ - Part No. USS-300) is used to detect the radiation, as the original CCD cameras used for the VISA IB experiment have a reduced resolution near the operating wavelength.

Another experimental challenge is the longitudinal alignment of the electron beam with the seed laser. This is accomplished with the use of a delay stage. The YAG delay stage allows for deliberate control of the timing of the seed laser at the entrance of the undulator. The timing overlap is achieved by synchronizing a signal from a stripline electron beam position monitor (BPM) and a photodiode detector signal on an oscilloscope with 150 ps resolution. The scan of the seed laser is accomplished with the delay stage. Second, appropriate optics were placed to keep the waist of the seed laser approximately 30 cm after the entrance of the undulator [100], to have maximum overlap between the electron

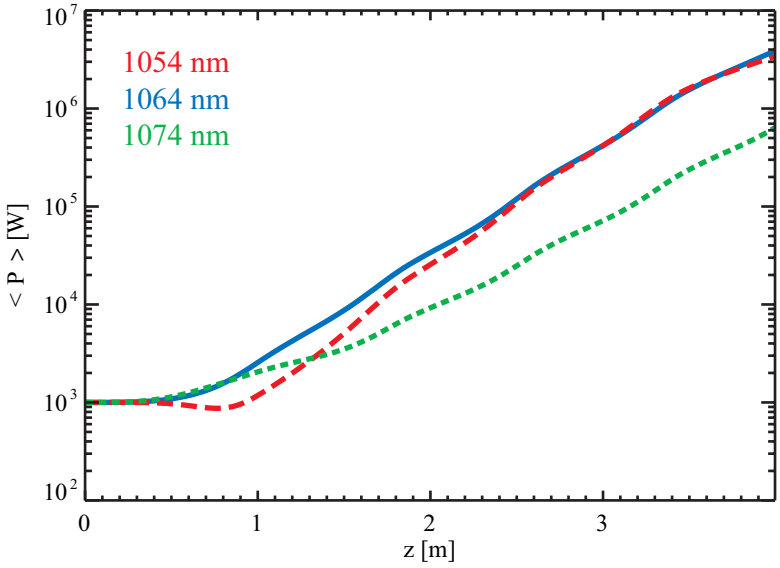

Figure 6.1: The simulated gain curves for the resonant wavelength (solid line), and slightly off-resonant wavelengths (dashed lines) for the Seeded Amplifier experiment.

beam and the seeding pulse in the start-up regime. The waist was chosen to be approximately two power gain lengths into the undulator so that the seed would have an increased intensity at the interaction, as opposed to having the waist at the entrance, where it would immediately begin to diffract.

One of the main focuses of this experiment is the study of the effects of detuning on the far-field distribution of the radiation. In Figure 6.1, a `GENESIS` study of the effect that detuning has on the emitted power. The far-field angular distribution for the detuning study is presented in Figure 6.2. The hollow mode in the far-field distribution is prevalent when the electron beam is run slightly off the design energy.

The electron beam preparation for the Seeded Amplifier experiment is very similar to that of VISA II. The magnet settings for the dipoles and quadrupoles were scaled to accommodate the lower energy of the electron beam. The T_{566} term

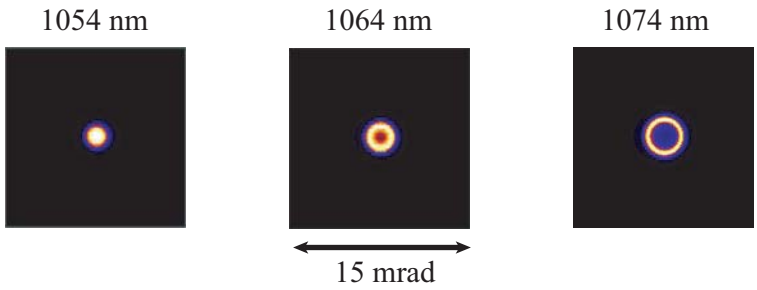

Figure 6.2: The far-field angular distributions for the resonant wavelength (1064 nm) and off-resonant cases (`GENESIS` simulation).

of the second-order transport matrix was reduced down to control the nonlinear compression. In fact, negative R_{56} partial compression is employed to generate the necessary peak current for SASE mode operations.

6.2 Outlook for the VISA Program

The future of the collaboration between the PBPL and the ATF with the VISA program is optimistic. In this section, a number of proposals for unique measurements and experiments underway at the VISA program are investigated. These measurements are viable under the current configuration at the ATF requiring minimal alterations and few additional diagnostics, yet will produce novel results that are of interest to the SASE FEL community.

6.2.1 Orbital Angular Momentum

The observation of hollow mode structures in the VISA I experiment and the subsequent observation of hollow mode structures with spirality in the VISA IB experimented prompted an interest in the nature of the radiation pulse. Similar helical patterns have been observed in the cases of laser light created as a

superposition of Laguerre-Gaussian modes [101]. Theory and experiment have established that these light beams have a property referred to as *orbital angular momentum* [82]. The orbital angular momentum can be manipulated in the laboratory for exotic reasons, such as optical trapping of atoms [102] and interferometric methods to characterize single photons [103].

As an example of such manipulation, a *mode converter* transforms a Hermite-Gaussian mode of a given order to a Laguerre-Gaussian mode and vice versa [104]. The $\pi/2$-mode converter is of special interest to the VISA program, as it has been used in other experiments to diagnose beams of similar ellipticity and structure. This is accomplished by the use of two cylindrical lenses placed $d = \sqrt{2}f$ apart, producing a relative phase shift of $\pi/2$ between the horizontal and vertical polarizations of the light. The resultant light will have distinct observable properties. Applying this simple device to the hollow mode profiles at the VISA undulator requires a simple modification to the far-field angular distribution screen. The necessary optics and hardware have been assembled and merely require setup and alignment. The results from this experiment would be of great interest to other SASE FEL experiments where hollow modes may also be observed. Although, the theory behind orbital angular momentum for FELs is still under investigation, a real measurement would jump start more in-depth studies as well as simulations into a previously overlooked phenomena of the nature of FEL light.

6.2.2 High Current FEL

The issues of high current FELs, where the high current is produced from a dedicated chicane compressor, has been studied previously [16]. The chicane compressor at the ATF, the result of a PBPL-ATF collaboration, has the ability

to produce an electron beam with currents as high as 1.5 kA [83]. With the data provided by the chicane for other measurements, it is only a small extension to apply the high current generated into the VISA undulator. In fact, `GENESIS` simulations have shown that saturation would be reached in the third meter of the four meter long undulator. Foreseen obstacles to this experiment involve the transport of such a beam through the ATF dogleg. Transverse and longitudinal nonlinear mechanisms along the dogleg have historically provided concern for the VISA program, however with the addition of the sextupole magnet correctors, second-order nonlinearites can be suppressed. Also, a proposed post-acceleration X-band cavity which would be installed downstream of the chicane, would remove most of the energy spread from the compression allowing a better manipulation of the compressed beam through the transport to the undulator [105]. The results of this experiment would interest members of the x-ray FEL community as most of the proposed facilities rely on compression for high gain.

6.2.3 Transition Undulator Radiation

The topic of *transition undulator radiation* (TUR) has been studied theoretically [106] and in simulations [107]. However, the observation of this phenomena has not been made to date. Such a measurement is possible with the current setup at the VISA program. Since TUR is radially polarized while the FEL radiation from the VISA undulator is horizontally polarized in the direction of the electron wiggle, it is possible to separate the two components with the use of a polarizing grid. The transversely polarized light is separated allowing only one direction of polarization through the wire grid, which is mounted on a rotatable stage. The resultant radiation can be measured and compared to theory and numerical models. At VISA, since the radiation and the electron beam strikes a reflecting metal

mirror to transport light outside the vacuum chamber, it would be necessary to bend the electron beam after it passed through the undulator to avoid the coherent transition radiation emitted if the beam were to hit the mirror. This would be accomplished with the placement of a steering magnet on the beam pipe after the undulator, sending the electron beam into a beam dump and the resultant light to the necessary optics. This bend would also be another source of radiation, namely coherent synchrotron and edge radiation, which may be parasitic to the measurement. The coherent edge radiation from this bend is also radially polarized, so care must be taken to filter out the background radiation from the radiation of interest.

6.3 Peroration: Summation and Prospectus

The VISA program at the ATF has produced many fruitful results over its tenure. In 2001, VISA demonstrated saturation in a SASE FEL at 840 nm, and output energy near 20 μJ. Also, the observation of hollow mode far-field angular distribution patterns was studied with start-to-end simulations. A novel electron bunch mechanism was discovered, during the experimental runs, which exploited the second-order longitudinal compression to yield high peak current beams. These high current beams were ultimately responsible for sustained high gain SASE FEL operations.

The VISA II mission sought to control this compression process by the deliberate placement of second-order corrector magnets (sextupoles). With a handle of second-order effects, certain beam properties can be manipulated, or in this case preserved through the transport. A linear correlation between the energy of the electrons and the longitudinal position in the beam, commonly referred to as a chirp, will be preserved through the dispersive line and ultimately in-

jected into the undulator. The amplification of this beam will produce frequency chirped radiation. Beamline parameters were carefully chosen through start-to-end simulations to optimize the beam current while maintaining a linear chirp at injection, as well as to maximize the output radiation signal. Novel diagnostics were developed to study the frequency chirped pulses, as well as to investigate the spectral angular intensity distribution.

The VISA IB program set forth to operate in a similar regime, prior to sextupole magnet installation could take place. A chirped beam was transported to the undulator, and high gain lasing was achieved. The FEL lasing differed from previous results mainly due to the anomalously large bandwidth that was emitted. Also, far-field angular distribution patterns were observed with distinct spiral features. Start-to-end simulations aided in our comprehension of this system and guided us to the conclusion that off-axis emission and subsequent mode enhancement delivered the observed bandwidth. Preliminary results obtained with the double differential spectrometer confirmed the quadratic dependence of the frequency on emission angles.

Although most of these experiments were put forth to study proof-of-principle effects in larger x-ray FEL systems, many surprises were met along the way. The VISA program shows the usefulness of start-to-end simulations in predicting such phenomena as well as analyzing the unanticipated observations that accompany the expected results. Since the VISA project at the ATF is currently the only short gain length SASE system in operation, it would prove useful to continue FEL experimental work there. Many unforeseen hindrances may arise in the building of the large scale x-ray FEL projects planned all over the world; testing individual aspects and schemes of such grand projects at the VISA SASE FEL would prove wise and economical as through simulations and trial and error, we

expand our knowledge base and understanding of these complex systems.

APPENDIX A

Abbreviations and Acronyms

In this dissertation, several uncommon acronyms and abbreviations are heavily used. Although each acronym is defined when it is first used and possibly defined numerous times throughout the text, this appendix will provide a brief reference listing the most commonly used acronyms.

ATF Accelerator Test Facility

BL3 Beamline 3

BNL Brookhaven National Laboratory

BW Bandwidth

FW Full Width

CTR Coherent Transition Radiation

DDS Double Differential Spectrometer

FEL Free Electron Laser

FROG Frequency Resolved Optical Gating

HES High Energy Slits

LCLS Linac Coherent Light Source

PBPL Particle Beam Physics Laboratory

SASE Self-Amplified Spontaneous Emission

SHG Second Harmonic Generation

SSG Small Signal Gain

TUR Transition Undulator Radiation

VISA Visible-to-Infrared SASE Amplifier

APPENDIX B

Review of Hamiltonian Dynamics

This Appendix serves as a brief review of the derivation of Hamilton's equations of motion. The Hamiltonian for a charged particle in an electromagnetic field is expeditiously derived [28, 39].

B.1 Equations of Motion

The equations of motion can be derived from a Hamiltonian defined by

$$H = \vec{p} \cdot \dot{\vec{x}} - L. \tag{B.1}$$

The canonical momenta and position of the particle are represented by $\vec{p}$ and $\vec{x}$, respectivley; L is the Lagrangian, which is a generalized description of the momenta and the coordinates of the particles in a system. The canonical momenta and position constitute a *conjugate pair* of variables. The Lagrangian is related to the canonical momenta and position by the following relation:

$$\dot{\vec{p}} = \frac{\partial L}{\partial \vec{x}}. \tag{B.2}$$

Once a Hamiltonian for a system is established, the equations of motion are derived using the following relations for the conjugate variables:

$$\dot{\vec{x}} = \frac{\partial H}{\partial \vec{p}}, \tag{B.3}$$

$$\dot{\vec{p}} = -\frac{\partial H}{\partial \vec{x}}. \tag{B.4}$$

If the Hamiltonian is not an explicit function of time, $\partial H/\partial t = 0$, then the Hamiltonian is a constant of the motion, which is usually related to the total energy (rest plus potential plus kinetic) of the system.

B.1.1 Charged Particle in Electromagnetic Field

The Lorentz force for a charged particle in a field is

$$\frac{d\vec{p}_m}{dt} = q\left(\vec{E} + \vec{v}\cdot\vec{B}\right). \tag{B.5}$$

Using the vector and scalar potentials defined by

$$\vec{B} = \vec{\nabla}\times\vec{A}, \tag{B.6}$$

$$\vec{E} = -\vec{\nabla}\varphi - \frac{\partial\vec{A}}{\partial t}, \tag{B.7}$$

Eq. B.5 can be rewritten as

$$\frac{d\vec{p}_m}{dt} = q\left(-\vec{\nabla}\varphi - \frac{d\vec{A}}{dt}\right). \tag{B.8}$$

In this expression, $\vec{p}_m$ is the mechanical momentum. It is important to note that the last term in this expression corresponds to the full derivative (not the partial derivative) of the vector potential. The relation between the mechanical momentum and the canonical momentum for this system is,

$$\vec{p} = \vec{p}_m + q\vec{A}. \tag{B.9}$$

The Lagrangian, from Eq. B.2 is

$$L = -\frac{mc^2}{\gamma} + q\vec{A}\cdot\dot{\vec{x}} - q\varphi. \tag{B.10}$$

Using this Lagrangian and the canonical momentum (Eq. B.9), the Hamiltonian of Eq. B.1 can be expressed as

$$H = \frac{(\vec{p} - q\vec{A})^2}{\gamma m} + \frac{mc^2}{\gamma} + q\varphi. \tag{B.11}$$

After some manipulation we can express the Hamiltonian as a function of the canonical momenta and the vector potential,

$$H = \sqrt{\left(\vec{p} - q\vec{A}\right)^2 c^2 + m^2c^4} + q\varphi. \tag{B.12}$$

In Chapter 2, this Hamiltonian is used to derive the equations of motion for electrons ($q = e$) in an undulator. The scalar potential is set to zero for the undulator magnet described. The Hamiltonian for an electron in a magnetic field is

$$H = \sqrt{\left(\vec{p} - e\vec{A}\right)^2 c^2 + (mc^2)^2}. \tag{B.13}$$

Since the free electron laser operates in a quasi-classical limit, a quantum treatment is not necessary [29, 30] and the classical approach is adequate. The classical Hamiltonian formalism is applied for the undulator radiation discussed in Chapter 2.

APPENDIX C

Spectral Angular Intensity Distribution of a Planar Undulator

A formal calculation of the spectral angular intensity distribution, informally referred to as the *double differential spectrum*, for the undulator radiation emitted by a planar undulator is presented. First, the calculation for the intensity distribution is performed for the case of on-axis observation. Second, the calculation is repeated for an arbitrary observation angle along the vertical dimension; this scenario resembles the experimental setup described in Section 4.3.

C.1 The On-axis Intensity Distribution for a Planar Undulator

The total intensity radiated by a single electron per unit solid angle, Ω, per unit frequency, ω, is given by [31]

$$\frac{d^2I}{d\omega d\Omega} = \frac{e^2\omega^2}{4\pi^2 c}\left|\int_{-\infty}^{\infty} \vec{n}\times\left(\vec{n}\times\vec{\beta}\right) e^{i\omega(t-\vec{n}\cdot\vec{r}(t)/c)}dt\right|^2. \tag{C.1}$$

Here, e is the unit electron charge, c is the speed of light, $\vec{n}$ is the unit normal vector which points from the electron to the observation point, $\vec{\beta}$ is the particle velocity normalized to c, and $\vec{r}(t)$ is the particle trajectory (from here on abbreviated to $\vec{r}$ as the explicit time dependence is understood). For the case of the planar undulator, observing the radiation in the far-field regime, and on-axis, or

zero observation angle ($\vec{n} = \hat{z}$, $\theta = 0$), we have the following expressions:

$$\vec{\beta} = \left(-\frac{K}{\gamma} \sin\left(k_u z\right), 0, \beta_0 + \frac{K^2}{4\gamma^2} \cos\left(2k_u z\right) \right), \tag{C.2}$$

$$\vec{r} = \left(\frac{K}{k_u \beta_0 \gamma} \cos\left(c k_u \beta_0 t\right), 0, c\beta_0 t + \frac{K^2}{8 k_u \beta_0 \gamma^2} \sin\left(2 c k_u \beta_0 t\right) \right), \tag{C.3}$$

$$\vec{n} = (0, 0, 1). \tag{C.4}$$

It is important to note that the expression for β in Eq. C.2 contains the dependence on $z = z(t)$ written to first-order. The higher order terms would include the longitudinal modulation given in Eq. C.3, but are not necessary for this calculation. In Eqs. C.2 and C.3, β_0 is the average longitudinal velocity, given by

$$\beta_0^2 = 1 - \frac{1}{\gamma^2} - < \beta_x^2 >,$$

$$\beta_0 = \sqrt{1 - \frac{1 + \frac{K^2}{2}}{\gamma^2}}. \tag{C.5}$$

The vector and cross products of Eq. C.1 become, respectively,

$$\vec{n} \times \left(\vec{n} \times \vec{\beta} \right) = \left(-\frac{K}{\gamma} \sin\left(k_u z\right), 0, 0 \right), \tag{C.6}$$

$$\frac{\vec{n} \cdot \vec{r}}{c} = \beta_0 t + \frac{K^2}{4\left(1 + \frac{K^2}{2}\right)} \frac{1}{\omega_r \beta_0} \sin\left(2 c k_u \beta_0 t\right), \tag{C.7}$$

where ω_r is simply the resonance condition for a planar undulator, on-axis,

$$\omega_r = \frac{2 k_u c \gamma^2}{\left(1 + \frac{K^2}{2}\right)}. \tag{C.8}$$

Choosing the appropriate limits of integration, $t = \pm N_u \lambda_u / 2c$, the interval of passage through undulator, Eq. C.1 becomes

$$\frac{d^2 I}{d\omega d\Omega} = \frac{e^2 \omega^2}{4\pi^2 c} \left| \int_{-\frac{N_u \lambda_u}{2c}}^{\frac{N_u \lambda_u}{2c}} \frac{K}{\gamma} \sin\left(k_u z\right) e^{i\omega \left(t - \beta_0 t - \frac{K^2}{4\left(1 + \frac{K^2}{2}\right)} \frac{1}{\omega_r \beta_0} \sin\left(2 c k_u \beta_0 t\right) \right)} dt \right|^2. \tag{C.9}$$

To continue the calculation, the following relation is used [32],

$$e^{-ia \sin b} = \sum_{m=-\infty}^{\infty} e^{-imb} J_m(a), \tag{C.10}$$

where $J_m(a)$ are the Bessel functions. It is judicious to use the following substitutions:

$$a = \frac{K^2}{4\left(1+\frac{K^2}{2}\right)}\frac{\omega}{\omega_r \beta_0}, \tag{C.11}$$

$$b = ck_u\beta_0 t. \tag{C.12}$$

With these substitutions, and the exponential expansion of $\sin k_u z$, the integrand in Eq. C.9 is simplified to

$$\begin{aligned}
\text{Integrand} &= \frac{-K}{2i\gamma}\left(e^{ib}-e^{-ib}\right)e^{i\omega(t-\beta_0 t)}e^{-ia\sin 2b} \\
&= \frac{-K}{2i\gamma}\left(e^{ib}-e^{-ib}\right)e^{i\omega(t-\beta_0 t)}\sum_{m=-\infty}^{\infty} e^{-i2mb}J_m(a) \\
&= \frac{-K}{2i\gamma}e^{i\omega(t-\beta_0 t)}\left[\sum_{m=-\infty}^{\infty} e^{-i(2m+1)b}J_m(a) - \sum_{l=-\infty}^{\infty} e^{-i(2l+1)b}J_l(a)\right] \\
&= \frac{-K}{2i\gamma}e^{i\omega(t-\beta_0 t)}\sum_{m=-\infty}^{\infty} e^{-i(2m+1)b}\left(J_m(a)-J_{m+1}(a)\right), \quad (l=m+1) \\
&= \frac{-K}{2i\gamma}e^{i\omega(t-\beta_0 t)}\sum_{n,odd}^{\infty} e^{-inb}\left(J_{(n-1)/2}(a)-J_{(n+1)/2}(a)\right).
\end{aligned} \tag{C.13}$$

Inserting this integrand into Eq. C.9, integrating the expression with the appropriate limits, then squaring the result yields

$$\begin{aligned}
\frac{d^2I}{d\omega d\Omega} &= \frac{e^2\omega^2}{4\pi^2 c}\sum_{n,odd}^{\infty}\left[J_{(n-1)/2}(a)-J_{(n+1)/2}(a)\right]^2\frac{K^2}{\gamma^2}\frac{N_u^2\lambda_u^2}{c^2}\left(\frac{\sin x_n}{x_n}\right)^2 \\
&= \frac{r_e mc^2 N_u^2\gamma^2}{c}\frac{K^2}{1+\frac{K^2}{2}}\sum_{n,odd}^{\infty}\left[J_{(n-1)/2}(a)-J_{(n+1)/2}(a)\right]^2\left(\frac{\omega}{\omega_r}\right)^2\left(\frac{\sin x_n}{x_n}\right)^2,
\end{aligned} \tag{C.14}$$

where $r_e = e^2/mc^2$ is the electron rest mass, and x_n is given by

$$x_n = \frac{N_u\lambda_u}{2c}\left(\omega(1-\beta_0)-nck_u\beta_0\right). \tag{C.15}$$

The function $(\sin x_n/x_n)^2$ is maximally peaked for $x_n = 0$ (Figure C.1). From Eq. C.15, it is apparent that only the odd harmonics of the radiated frequency, $n\omega_r$, are observable for the on-axis scenario. Armed with the knowledge that only odd harmonics are present for the case of the on-axis planar undulator ($\omega = n\omega_r$), and using the first order Taylor expansion for β_0 from Eq. C.5,

$$\beta_0 \approx 1 - \frac{(1 + \frac{K^2}{2})}{2\gamma^2}, \tag{C.16}$$

the final expression for the intensity distribution becomes,

$$\frac{d^2I}{d\omega d\Omega} = \frac{r_e mc^2}{c} N_u^2 \gamma^2 \frac{K^2}{1 + \frac{K^2}{2}} \sum_{n,odd}^{\infty} F_n(K) \left(\frac{\sin x_n}{x_n}\right)^2, \tag{C.17}$$

where

$$F_n(K) = n^2 \left[J_{(n-1)/2}(\xi_n) - J_{(n+1)/2}(\xi_n)\right]^2 \tag{C.18}$$

and

$$x_n = N_u \pi \left(\frac{\omega - n\omega_r}{\omega_r}\right) \tag{C.19}$$

with ξ_n given by

$$\xi_n = \frac{nK^2}{4(1 + \frac{K^2}{2})}. \tag{C.20}$$

C.2 Intensity Distribution for a Planar Undulator with a Vertical Observation Angle

The spectral angular intensity distribution of undulator radiation for arbitrary angle is slightly more complicated than that for the on-axis case. We begin with Eq. C.1, and use the same position vector ($\vec{r}$) and velocity vector ($\vec{\beta}$) as in the on-axis case, except the unit normal vector now points in an arbitrary angle in the vertical dimension,

$$\vec{n} = (0, \sin\theta, \cos\theta). \tag{C.21}$$

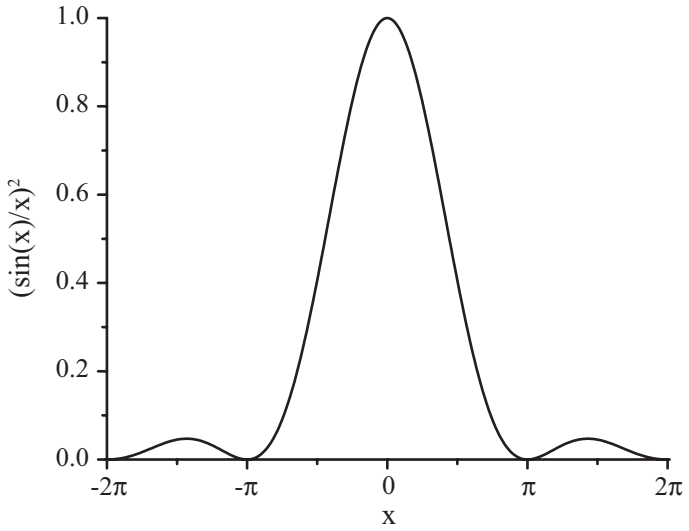

Figure C.1: The lineshape function of the intensity distribution is maximally peaked at zero.

The vector and cross products of interest are, respectively,

$$\vec{n} \times \left(\vec{n} \times \vec{\beta}\right) = \begin{pmatrix} -\frac{K}{\gamma} \sin\left(k_u c \beta_0 t\right) \\ -\sin\theta\cos\theta\left(\beta_0 + \frac{K^2}{4\gamma^2}\cos\left(2k_u c\beta_0 t\right)\right) \\ \sin^2\theta\left(\beta_0 + \frac{K^2}{4\gamma^2}\cos\left(2k_u c\beta_0 t\right)\right) \end{pmatrix}, \tag{C.22}$$

$$\frac{\vec{n}\cdot\vec{r}}{c} = \cos\theta\left(\beta_0 t + \frac{K^2}{8ck_u\beta_0\gamma^2}\sin\left(2ck_u\beta_0 t\right)\right). \tag{C.23}$$

It is apparent that the $\hat{x}$-component of the integral dominates over the other two terms, which, when squared are proportional to $1/\gamma^4$. The terms proportional to $\sin\theta$ grow like $\theta \approx 1/\gamma$; they are also neglected when multiplied to the higher order terms when the product is on the scale of $1/\gamma^3$ or smaller. Therefore, the integrand of interest to be evaluated is

$$\text{Integrand} = -\frac{K}{\gamma}\sin\left(k_u c\beta_0 t\right) e^{i\omega\left(t - \beta_0 t\cos\theta - \frac{K^2\cos\theta}{8k_u c\beta_0\gamma^2}\sin(2ck_u\beta_0 t)\right)}, \tag{C.24}$$

with the limits $t = \pm N_u\lambda_u/2c$, as for the on axis case. The resonance condition

for an arbitrary observation angle, θ, is given by

$$\omega_r(\theta) = \frac{ck_u}{1 - \beta_0 \cos\theta}. \tag{C.25}$$

This form can be reduced using the cosine expansion for small angles and the expression from Eq. C.5, to yield

$$\omega_r(\theta) = \frac{2\gamma^2 ck_u}{\left(1 + \frac{K^2}{2} + \gamma^2\theta^2\right)}. \tag{C.26}$$

Applying the same techniques as in the previous section using the integrand of Eq. C.24, the spectral-angular distribution reduces down to

$$\frac{d^2I}{d\omega d\Omega} = \frac{r_e mc^2}{c}\frac{K^2}{4}N_u^2\gamma^2 \sum_{n,odd}\left(\frac{\omega\lambda_u}{2\pi c\gamma^2}\right)^2 \left[J_{(n-1)/2}(\xi_n) - J_{(n+1)2}(\xi_n)\right]^2 \left(\frac{\sin x_n}{x_n}\right)^2. \tag{C.27}$$

Using Eq. C.26, the argument of the sine function,

$$x_n = \frac{N_u\lambda_u}{2c}\omega(1 - \beta_0\cos\theta) - nck_u\beta_0, \tag{C.28}$$

can be rewritten in a form similar to that in the previous section,

$$x_n = N_u\pi\left(\frac{\omega - n\omega_r(\theta)}{\omega_r(\theta)}\right). \tag{C.29}$$

The argument of the Bessel functions, now dependent on the angle, is

$$\begin{aligned}\xi_n(\theta) &= \frac{\omega K^2\cos\theta}{8k_u c\beta_0\gamma^2}, \\ \xi_n(\theta) &= \frac{nK^2}{4\left(1 + \frac{K^2}{2} + \gamma^2\theta^2\right)}.\end{aligned} \tag{C.30}$$

Then, we redefine the F_n's in a similar fashion,

$$F_n(K,\theta) = n^2\left[J_{(n-1)/2}(\xi_n(\theta)) - J_{(n+1)/2}(\xi_n(\theta))\right]^2. \tag{C.31}$$

The final expression for the spectral-angular distribution is

$$\frac{d^2I}{d\omega d\Omega} = \frac{r_e mc^2}{c}N_u^2\gamma^2\frac{K^2}{1 + \frac{K^2}{2} + \gamma^2\theta^2}\sum_{n,odd}^{\infty}F_n(K,\theta)\left(\frac{\sin x_n}{x_n}\right)^2. \tag{C.32}$$

References

[1] R. Neutze, *et al.* Potential for biomolecular imaging with femtosecond x-ray pulses. *Nature*, 406:752, 2000.

[2] M. Altarelli, A. Salam. The quest for brilliance: Light sources from the third to the fourth generation. *Europhyiscs News*, 35(2), 2004.

[3] G.R. Neil, *et al.* Sustained kilowatt lasing in a free-electron laser with same-cell energy recovery. *Physical Review Letters*, 84(4):662, 2000.

[4] M. Cornacchia *et al.* Linac coherent light source design study report. Technical Report SLAC-R-521, Stanford Linear Accelerator Center, Stanford, 1998.

[5] TESLA-FEL. Deutsches Elektronen Synchrotron 2001-05. Technical Report DESY-01-011, Germany, 2001.

[6] J.S. Oh, Y. Kim. PAL linac upgrade for a 1-3 Å XFEL. In *Proceedings of LINAC 2004*, page 544, Lubeck, Germany, 2004.

[7] T. Shintake. Soft-x-ray SASE-FEL project at SPRING-8 Japan. In *Proceedings of the Second Asian Particle Accelerator Conference*, Beijing, China, 2002.

[8] J.M.J. Madey. Stimulated emission of bremsstrahlung in a periodic magnetic field. *Journal of Applied Physics*, 42(5):1906, 1971.

[9] J.B. Murphy and C. Pellegrini. Introduction to the physics of the free electron laser. In *Laser Handbook*, volume 6, chapter 2. North Holland, 1990.

[10] G. O'Shea, H. Freund. Free-electron lasers: Status and applications. *Science*, 292:1853, 2001.

[11] L. R. Elias, *et al.* Observation of stimulated emission of radiation by relativistic electrons in a spatially periodic transverse magnetic field. *Physical Review Letters*, 36:717, 1976.

[12] D.A.G. Deacon, *et al.* First operation of a free-electron laser. *Physical Review Letters*, 38:892, 1977.

[13] W.B. Colson, B.W. Williams. Free electron lasers in 2004. In *Proceedings of the 2004 FEL Conference*, page 706, Trieste, Italy, 2004.

[14] M. Hogan, *et al.* Measurements of high gain and intensity fluctuations in a self-amplified, spontaneous-emission free-electron laser. *Physical Review Letters*, 80(2):289, 1998.

[15] M. Hogan, *et al.* Measurements of gain larger than 10^5 at 12μm in a self-amplified spontaneous-emission free-electron laser. *Physical Review Letters*, 81(22):4867, 1998.

[16] S.V. Milton, *et al.* Exponential gain and saturation of a self-amplified spontaneous emission free-electron laser. *Science*, 292:2037, 2001.

[17] C. Pellegrini, J. Rosenzweig, I. Ben-Zvi. A SASE-free electron laser experiment, VISA, at the ATF linac. ATF Experiments, 1998.

[18] A. Murokh, *et al.* Properties of the ultrashort gain length, self-amplified spontaneous emission free-electron laser in the linear regime and saturation. *Physical Review E*, 67:066501, 2003.

[19] V. Ayvazyan, *et al.* Generation of GW radiation pulses from a VUV free-electron laser operating in the femtosecond regime. *Physical Review Letters*, 88:104802, 2002.

[20] S.J. Allen, *et al.* Materials science in the far-IR with electrostatic based FELs. *Nuclear Instruments and Methods in Physics Research A*, 358:536, 1995.

[21] A. Peremans, *et al.* Vibrational spectroscopy at interfaces by ir-vis sum-frequency generation using CLIO FEL. *Nuclear Instruments and Methods in Physics Research A*, 375:657, 1996.

[22] M. Budde, *et al.* Vibrational lifetime of bond-center hydrogen in crystalline silicon. *Physical Review Letters*, 85(7):1452, 2000.

[23] C. Pellegrini and S. Reiche. The development of x-ray free-electron lasers. *IEEE Journal of Selected Topics in Quantum Electronics*, 10(6):1393, 2004.

[24] E.D. Courant, C. Pellegrini, W. Zakowicz. High-energy inverse free-electron-laser accelerator. *Physical Review A*, 32:2813, 1985.

[25] E.L. Saldin, E.A. Schneidmiller, M.V. Yurkov. *The Physics of Free Electron Lasers*. Springer-Verlag, Germany, 1st edition, 2000.

[26] S. Reiche. Fourth generation light sources - I: X-ray laser. United States Particle Accelerator School, 2003. Lecture Notes.

[27] C. Pellegrini. Electromagnetic radiation from relativistic electrons and free-electron lasers. UCLA Department of Physics and Astronomy, 2004.

[28] H. Goldstein. *Classical Mechanics*. Addison-Wesley, Massachusetts, 1st edition, 1950.

[29] E.L. Saldin, E.A. Schneidmiller, M.V. Yurkov. Calculation of energy diffusion in an electron beam due to quantum fluctuations of undulator radiation. *Nuclear Instruments and Methods in Physics Research A*, 381:545, 1996.

[30] C.B. Schroeder, C. Pellegrini, P. Chen. Quantum effects in high gain free-electron lasers. *Physical Review E*, 64:056502, 2001.

[31] J.D. Jackson. *Classical Electrodynamics*. Wiley, New York, 3rd edition, 1999.

[32] M. Abramowitz and I. Stegun. *Handbook of Mathematical Functions*. Dover, New York, 10th edition, 1972.

[33] A.E. Siegman. *Lasers*. University Science Books, California, 1st edition, 1986.

[34] S. Reiche. *Numerical Studies for a Single Pass High Gain Free-Electron Laser*. PhD thesis, University of Hamburg, 1999.

[35] R. Bonifacio, C. Pellegrini, L. Narducci. Collective instabilities and high-gain regime in a free electron laser. *Optical Communications*, 50:373, 1984.

[36] R. Bonifacio, F. Casagrande, C. Pellegrini. Hamiltonian model of a free electron laser. *Optical Communications*, 61:55, 1987.

[37] A.A. Zholents, *et al.* Acurren-enhanced SASE using an optical laser and its applications to the LCLS. In *Proceedings of the 2004 FEL Conference*, page 582, Trieste, Italy, 2004.

[38] K.-J. Kim. Three-dimensional analysis of coherent amplification and self-amplified spontaneous emission in free-electron lasers. *Physical Review Letters*, 57(15):1871, 1986.

[39] J.B. Rosenzweig. *Fundamentals of beam physics*. Oxford University Press, New York, 1st edition, 2003.

[40] J.-M. Wang and L.-H. Yu. A transient analysis of a bunched beam free electron laser. *Nuclear Instruments and Methods in Physics Research A*, 250:484, 1986.

[41] K.-J. Kim. An analysis of self-amplified spontaneous emission. *Nuclear Instruments and Methods in Physics Research A*, 250:396, 1986.

[42] M.V. Yurkov E.L. Saldin, E.A. Schneidmiller. Statistical properties of the radiation from SASE FEL operating in the linear regime. *Nuclear Instruments and Methods in Physics Research A*, 407:291, 1998.

[43] C. Schroeder, C. Pellegrini, S. Reiche, J. Arthur, P. Emma. Chirped-beam two-stage free-electron laser for high-power femtosecond x-ray pulse generation. *Journal of the Optical Society of America B*, 19:1782, 2002.

[44] G. Dattoli, G. De Ninno, M. Migliorati. Landau damping and free-electron laser interaction in storage rings. *The European Physical Journal D*, 33:273, 2005.

[45] S. Krinsky and Z. Huang. Frequency chirped self-amplified spontaneous-emission free-electron laser. *Physical Review Special Topics - Accelerators and Beams*, 6:050702, 2003.

[46] I. Ben-Zvi. A machine for learning. *Cern Courier*, October 2004.

[47] World Wide Web. ATF laser system. `http://www.bnl.gov/atf/systems/lasers/lasersys.html`, 2005.

[48] M. Babzien. Brookhaven ATF drive laser performance. presented at Stanford Linear Accelerator Center, October 2002.

[49] World Wide Web. ATF core capabilities. `http://www.bnl.gov/atf/systems/rfgun/pi_describe.html`, 2005.

[50] D.T. Palmer, *et al.* Emittance studies of the BNL/UCLA 1.6 cell photocathode rf gun. In *Proceedings of the 1997 Particle Accelerator Conference*, page 2687, Vancouver, BC, Canada, 1997.

[51] B.E. Carlsten. New photoelectric injector design for the Los Alamos National Laboratory XUV FEL accelerator. *Nuclear Instruments and Methods in Physics Research A*, 285:313, 1989.

[52] X. Qiu, K. Batchelor, I. Ben-Zvi, X-J. Wang. Demonstration of emittance compensation through the measurement of the slice emittance of a 10-ps electron bunch. *Physical Review Letters*, 76(20):3723, 1996.

[53] R. Boni, *et al.* Reduction of multipacting in an accelerator cavity. *IEEE Transactions on Nuclear Science*, NS-32(5):2815, 1985.

[54] V. Yakimenko. Photoinjector. ATF Newsletter, February 2005.

[55] X.J. Wang, M. Babzien, I. Ben-Zvi, R. Malone, V. Yakimenko. FEL technologies R & D and SASE gain enhancement observation at the BNL ATF. In *Proceedings of EPAC 2000*, page 779, Vienna, Austria, 2000.

[56] World Wide Web. ATF computer control system. `http://www.bnl.gov/atf/ControlSys/ControlSys.html`, 2005.

[57] R. Malone and X.J. Wang. Using a commercial mathematics software package for on-line analysis at the BNL Accelerator Test Facility. *IEEE Transactions on Nuclear Science*, 47(2):288, 2000.

[58] R. Malone, X. Wang, V. Yakimenko. Data transfer in Mathcad. *Scientific Computing and Instrumentation*, April 2001.

[59] R. Malone. Computer control system. ATF Newsletter, February 2005.

[60] K. Halbach. Design of permanent multipole magnets with oriented rare earth cobalt material. *Nuclear Instruments and Methods*, 169(1):1–10, 1980.

[61] P. Emma, H.-D. Nuhn. FEL trajectory analysis for the VISA experiment. In *Proceedings of the 20th International FEL 98 Conference*, pages II–35, Williamsburg, VA, USA, 1998.

[62] A. Tremaine, H.-D. Nuhn. Private Communication.

[63] R. Carr, *et al.* Visible-infrared self-amplified spontaneous emission amplifier free electron laser undulator. *Physical Review Special Topics - Accelerators and Beams*, 4:122402, 2001.

[64] G. Rakowsky, *et al.* Measurement and optimization of the VISA undulator. In *Proceedings of the 1999 Particle Accelerator Conference*, page 2698, New York, NY, USA, 1999.

[65] P. Frigola, *et al.* Initial gain measurements of an 800nm SASE FEL, VISA. *Nuclear Instruments and Methods in Physics Research A*, 475:339, 2001.

[66] R. Ruland, *et al.* Alignment of the VISA undulator. In *Proceedings of the 1999 Particle Accelerator Conference*, page 1390, New York, NY, USA, 1999.

[67] A. Murokh, *et al.* Results of the VISA SASE FEL experiment at 840nm. *Nuclear Instruments and Methods in Physics Research A*, 507:417, 2003.

[68] A. Murokh, J. Rosenzweig, I. Ben-Zvi, X. Wang, V. Yakimenko. Limitations on measuring a transverse profile of ultra-dense electron beams with scintillators. In *Proceedings of the 2001 Particle Accelerator Conference*, page 1333, Chicago, IL, USA, 2001.

[69] K. Brown. A first- and second-order matrix theory for the design of beam transport systems and charged particle spectrometers. Technical Report SLAC-R-075, Stanford Linear Accelerator Center, Stanford, 1982.

[70] L.M. Young, J.H. Billen. PARMELA. Technical Report LA-UR-96-1835, Accelerator Code Group, Los Alamos National Laboratory, USA, rev. 2000.

[71] S.G. Anderson. *Creation, Manipulation, and Diagnosis of Intense, Relativistic Picosecond Photo-electron Beams*. PhD thesis, University of California Los Angeles, 2002.

[72] M. Borland. elegant: A flexible sdds-compliant code for accelerator simulation. Technical Report LS-287, Advanced Photon Source, Argonne National Laboratory, USA, 2000.

[73] S. Reiche. GENESIS 1.3: a fully 3D time-dependent FEL simulation code. *Nuclear Instruments and Methods in Physics Research A*, 429:243, 1999.

[74] A. Tremaine, *et al.* Experimental characterization of nonlinear harmonic radiation from a visible self-amplified spontaneous emission free-electron laser at saturation. *Physical Review Letters*, 88:204801, 2002.

[75] R.J. England, J.B. Rosenzweig, G. Andonian, P. Musumeci, G. Travish, R. Yoder. Sextupole correction of the longitudinal transport of relativistic beams in dispersionless translating sections. *Physical Review Special Topics - Accelerators and Beams*, 8:012801, 2005.

[76] M.J.E. Golay. Theoretical consideration in heat and infra-red detection, with particular reference to the pneumatic detector. *The Review of Scientific Instruments*, 18(5):347, 1947.

[77] S.Y. Lee. *Accelerator Phyics*. World Scientific, New Jersey, 2nd edition, 1999.

[78] P. Piot, D.R. Douglas, G.A. Krafft. Longitudinal phase space manipulation in energy recovering linac-driven free-electron lasers. *Physical Review Special Topics - Accelerators and Beams*, 6:030702, 2003.

[79] G.A. Krafft. Spectral distributions of thomson-scattered photons from high-intensity pulsed lasers. *Physical Review Letters*, 92:204802, 2004.

[80] S. Krinsky and L.H. Yu. Output power in guided modes for amplified spontaneous emission in a single-pass free-electron laser. *Physical Review A*, 35:3406, 1987.

[81] G. Andonian, *et al.* Observation of anomalously large spectral bandwidth in a high-gain self-amplified spontaneous emission free-electron laser. *Physical Review Letters*, 95:054801, 2005.

[82] A.T. O'Neil, I. MacVicar, L. Allen, ¡.J. Padjett. Intrinsic and extrinsic nature of the orbital angular momentum of a light beam. *Physical Review Letters*, 88(5):053601, 2002.

[83] R.B. Agustsson. Design, construction, simulation and implementation of a magnetic electron bunch compressor. Master's thesis, University of California Los Angeles, 2004.

[84] R. Agustsson, J. Rosenzweig. Chicane compressor development for BNL ATF applications to SASE FEL. In *22nd International Free Electron Laser Conference and 7th FEL Users Workshop*, Durham, North Carolina, USA, 2000.

[85] G. Andonian, *et al.* Design and status of the VISA II experiment. In *Proceedings of the 2003 Particle Accelerator Conference*, page 944, Portland, Oregon, USA, 2003.

[86] X. Wu, *et al.* The design of the isochronous and achromatic charge-stripping sections for the rare isotope accelerator. In *Proceedings of the European Particle Accelerator Conference 2002*, page 1211, Paris, France, 2002.

[87] R.A. Bosch. Extracting edge radiation within a straight section of an electron storage ring. *Physical Review Special Topics - Accelerators and Beams*, 5:020701, 2002.

[88] V.L. Ginzburg and V.N. Tsytovich. Several problems of the theory of transition radiation and transition scattering. *Physics Reports*, 49(1):1–89, 1978.

[89] F. Zhou, *et al.* Experimental characterizations of 4-D transverse phase space of a compressed beam. In *Proceedings of the 2005 Particle Accelerator Conference*, page 2263, Knoxville, Tennessee, USA, 2005.

[90] U. Happek, A.J. Sievers, E.B. Blum. Observation of coherent transition radiation. *Physical Review Letters*, 67(21):2962, 1991.

[91] C. Pellegrini, J. Stohr. X-ray free-electron lasers - principles, properties and applications. *Nuclear Instruments and Methods in Physics Research A*, 500:33, 2003.

[92] C. Pellegrini. High power femtosecond pulses from an x-ray SASE-FEL. *Nuclear Instruments and Methods in Physics Research A*, 445:124, 2000.

[93] R. Trebino. Private Communication.

[94] R.. Trebino. *Frequency-Resolved Optical Gating: The Measurement of Ultrashort Laser Pulses*. Kluwer Academic, Massachusetts, 1st edition, 2000.

[95] Y. Li, J. Lewellen, Z. Huang, V. Sajaev, S.V. Milton. Time-resolved phase measurement of a self-amplified free-electron laser. *Physical Review Letters*, 89(23):234801, 2002.

[96] E.L. Saldin, E.A. Schneidmiller, M.V. Yurkov. A novel diagnostics of ultrashort electron bunches based on detection of coherent radiation from bunched electron beam in an undulator. In *Proceedings of the 2004 FEL Conference*, page 375, Trieste, Italy, 2004.

[97] P. O'Shea, M. Kimmel, X. Gu, and R. Trebino. Highly simplified device for ultrashort-pulse measurement. *Optics Letters*, 26:932, 2001.

[98] World Wide Web. Swamp optics - ultrashort laser pulse measurement. `http://www.swampoptics.com`, 2006.

[99] S. Cialdi. Temporal characterization of an FEL pulse by Grenouille. PBPL Seminar Series - Lecture 11, Fall 2003.

[100] M. Babzien. Private Communication.

[101] L. Allen, *et al.* Orbital angular momentum of light and the transformation of laguerre-gaussian laser modes. *Physical Review A*, 45(11):8185, 1992.

[102] T. Kuga, *et al.* Novel optical trap of atoms with a doughnut beam. *Physical Review Letters*, 78(25):4713, 1997.

[103] J. Leach, *et al.* Measuring the orbital angular momentum of a single photon. *Physical Review Letters*, 88(24):257901, 2002.

[104] M.W. Beijersbergen, *et al.* Astigmatic laser mode converters and transfer of orbital angular momentum. *Optics Communications*, 96:123, 1993.

[105] V. Yakimenko. Private Communication.

[106] K.-J. Kim. Transition undulator radiation as bright infrared source. *Physical Review Letters*, 76:1244, 1996.

[107] S. Reiche, Z. Huang. Coherent radiation effects in the LCLS undulator. In *Proceedings of the 2004 FEL Conference*, page 193, Trieste, Italy, 2004.